Analysis of Phase Stability and Defect Mobility in Functional Oxides Exposed to Extreme Conditions

by

Matthew J. Webb

A dissertation submitted in partial fulfillment
of the requirements for the degree of
Doctor of Philosophy
(Materials Science and Engineering)
in the University of Michigan
2025

Doctoral Committee:

Professor John Heron, Chair
Professor Emmanouil Kioupakis
Professor Andrej Lenert
Professor Yiyang Li

Matthew J. Webb
webbmj@umich.edu
ORCID iD: 0000-0002-8022-7031

© Matthew J. Webb 2025

ACKNOWLEDGEMENTS

The work presented in this thesis is the result of many years of collaboration between myself and many great co-authors. For this, I thank S. McSherry, J. Kaufman, Z. Deng, A. Davoodabadi, T. Ma, A. H. Hunter, M. Gerhart, S. Baksa, S. Gelin, A.-R. Ansbro, P. B. Meisenheimer, T. Chiang, M. Lenox, and J. Gray.

I would also like to thank the rest of the members of the ferroelectronics lab throughout my time here, S. Novakov, N. Vu, S. Chae, P. Kezer, B. Justus, R. Oliver, Y. Liang, and of course, our Professor J. Heron, for their help and support.

Finally, I would like to thank my family, my parents, Gillian and Andrew, and my wife, Veronica, for their unwavering support.

I acknowledge financial support from the Semiconductor Research Corporation Nanomanufacturing Materials and Processes Program, from the Department of Defense, Defense Advanced Research Projects Agency, and from the National Science Foundation.

TABLE OF CONTENTS

ACKNOWLEDGEMENTS ii

LIST OF FIGURES vi

LIST OF APPENDICES xv

LIST OF ACRONYMS xvi

ABSTRACT xvii

CHAPTER

1 Understanding Extreme Conditions 1

1.1 A case study on stability in extreme conditions 1

1.2 Functional oxide materials 3

1.3 Failure mechanisms 5

1.3.1 Phase transformations 6

1.3.2 Grain growth 7

1.3.3 Corrosion (Oxidation) 7

1.3.4 Fatigue 8

1.3.5 Defect migration, interdiffusion and electromigration 8

1.3.6 Strain relaxation failure 9

1.3.7 Dielectric breakdown 9

2 Experimental Methods 11

2.1 X-ray Diffraction 11

2.1.1 Symmetric scan . . . 11
2.1.2 X-ray Reflectivity . . . 12
2.1.3 Reciprocal Space Mapping . . . 13
2.1.4 Grazing Incidence X-ray Diffraction . . . 14
2.2 Electron Microscopy . . . 15
2.2.1 Scanning Electron Microscopy . . . 16
2.2.2 Transmission Electron Microscopy . . . 16
2.2.3 Energy Dispersive Spectroscopy . . . 16
2.3 Thin Film Deposition Techniques . . . 17
2.3.1 Pulsed Laser Deposition . . . 17
2.3.2 Atomic Layer Deposition . . . 18

3 Investigating Materials Predicted to Withstand Extreme Temperature . . . 20

3.1 Background: high entropy materials . . . 20
3.2 Solubility of copper and zinc in (MgCoNiCuZn)O . . . 24
3.3 Fabrication of (MgCoNiCuZn)O . . . 28
3.4 Phase stability of high entropy oxide (MgCoNiCuZn)O under extreme conditions 29
3.5 Conclusion: the stability of bulk (MgCoNiCuZn)O . . . 39

4 Evaluating the Stability of Poly-Cationic Oxide Thin Films with Optical Properties . 40

4.1 Background: thermal stability and optical properties . . . 40
4.2 Optical properties and thermal stability of high entropy oxide thin films . . . 42
4.3 A new approach to overcoming failure modes . . . 46
4.4 Fabrication and stability of $BaZr_{0.5}Hf_{0.5}O_3$ and MgO heterostructures . . . 47
4.5 Optical performance under extreme conditions . . . 54
4.6 Investigating the failure mechanism . . . 56
4.7 Conclusion: the stability of optical heterostructures . . . 62

5 Examining Fatigue Behavior in Ferroelectric Thin Films . . . 64

5.1 Background: ferroelectric materials . . . 64
5.2 Fabrication and structural characterization of $Hf_{0.5}Zr_{0.5}O_2$ . . . 67

5.3 Cycling-limited stability of $Hf_{0.5}Zr_{0.5}O_2$ 70
5.4 Conclusion: the stability of ferroelectric devices 77

6 Conclusions and Suggested Future Works 78

6.1 Suggested future work 79
6.1.1 Methods to improve the stability of (MgCoNiCuZn)O 79
6.1.2 Monostructural high entropy oxides 81
6.1.3 Methods to improve the stability of the $BaZr_{0.5}Hf_{0.5}O_3$/MgO system . . . 82
6.1.4 Low lattice mismatch functional oxide pairs 84

APPENDICES 85

BIBLIOGRAPHY 96

LIST OF FIGURES

FIGURE

1.1 Illustration of the energy scales of different external stimuli. Adapted from [1]. 1

1.2 Evolution of turbine material capability and of turbine gas inlet temperature. Adapted from data in [6]. With inlet temperatures ever increasing to improve engine efficiency, we observe a divergence of metal turbine temperature capability, and the actual operating temperatures of the turbine. This is achieved through the use of internal cooling structures and thermal barrier coatings. 2

1.3 Estimate of TPV efficiency as a figure of merit versus emitter temperature, comparing different emitter plus filtering approaches in different atmospheres, including several data points for a single MgO:NiO based TPV system. Generally, a higher efficiency is observed for higher emitter temperatures, requiring more stable filtering solutions. Adapted from [28]. Data collected from [29–34]. 4

1.4 A schematic phase diagram of a simple eutectic system. Starting from ①, a single phase (A) composition a change of +ΔT or - ΔT will result in a phase transformation into a mixed (A + liquid, ②, or A + B, ③) phase. Although this is illustrated for temperature, it is also possible to cause this transformation with other stimuli, such as strain or electric field. 6

2.1 A XRD schematic, demonstrating the conditions for reflection, or Bragg's law conditions. Spacing between the planes is d and the angle of incidence is θ with a wavelength λ. 12

2.2 A XRR schematic, demonstrating the relations between film properties and observed patterns, using computed data. The density is determined from the critical angle, θ_c, where the intensity initially drops, while the period of oscillations, $\Delta\theta$ fits the film thickness, and the amplitude of oscillation is related to the difference in layer density, $\Delta\rho$. Not shown on the figure, the rate of intensity decay is related to the film roughness. Adapted from [124]. 14

2.3 An RSM schematic in reciprocal space coordinates, demonstrating a film that is in a partially relaxed strain state compared to the substrate. The fully strained and fully relaxed lines are also shown. 15

2.4 A schematic showing the difference between the SEM column, where the beam is focused on to a sample, with additional detectors to collect backscattered and secondary electrons and a TEM column, where the beam is directed through a sample and collected by a detector afterwards. 17

2.5 (a) A schematic detailing the components of a PLD chamber. (b) Schematic structure of films grown under each growth mode described in the text. 19

3.1 Calculated (**eq. 3.2**) using configurational entropy for an equimolar compound with N elements on the disordered site, the value for an equimolar compound with 5 disordered elements is highlighted, being the most common type of high entropy compound. 21

3.2 Schematics showing the unit cell for: an FCC metal, a rocksalt oxide, and a perovskite oxide. Included are the calculated entropy values using **eq. 3.2**. This is then converted to an entropy per unit value to illustrate the lower magnitude of configurational entropy for HEOs compared to HEAs due primarily to the presence of the oxygen sub-lattice. 23

3.3 Solubility of Cu and Zn in the rocksalt oxides, extracted from the binary phase diagram solidus. The data used to produce this figure is from [183–188]. Solid lines and points indicate experimental data, while dotted lines indicate a linear extrapolation from the measured data. The shaded area is the maximum range of miscibility predicted for the binary rocksalt-CuO and rocksalt-ZnO systems. It is observed that the copper solubility in the rocksalt oxides generally peaks around 1100-1200 ºC, before dropping rapidly. Conversely, within the temperature range considered here, the Zn solubility in the rocksalt oxides monotonically increases. Note that there is a region of $\geq$ 20% solubility for CuO and ZnO in all the rocksalt oxides from about 1050-1200 ºC. The NiO-ZnO data is shown as individual points as it is obtained from the NiO-ZnO axis of a ternary Fe_2O_3-NiO-ZnO phase diagram as no NiO-ZnO data could be found. 26

3.4 This figure is constructed using data from **Figure 3.3** and **Figure A.1**. The additional computational data is highlighted in green and denoted by (cp). By averaging the solubility of the binary rocksalt oxides, we can produce a simplified hypothesis on the solubility of Cu and Zn in (MgCoNiCuZn)O. This gives the expected Cu and Zn values shown, assuming an initial composition of 20% of each. 27

3.5 (a) X-ray diffraction data for an as-sintered pellet (1100 ºC for 18 hours) of polycrystalline (MgCoNiCuZn)O. (b) X-ray diffraction analysis of (MgCoNiCuZn)O produced in the seminal work by Rost et al. This sample was sintered at 1000 ºC for 12 hours twice. Data adapted from [160], note that J14 is another name for (MgCoNiCuZn)O. The same peaks are observed in both sets of data with a similar ratio of intensity between the differently indexed peaks, indicating that a single-phase rocksalt structured polycrystalline sample has been obtained. 28

3.6 (a) X-ray diffraction analysis indicating the presence of wurtzite and tenorite secondary phases, consisting of CuO and ZnO that is metastable in the rocksalt structure. Without quenching from $\sim$ 900 ºC, these elements segregate from the rocksalt phase. An * marks a secondary phase identified as either wurtzite or tenorite. (b) SEM EDS analysis of a (MgCoNiCuZn)O sample following an anneal at 1700 ºC for 2 hours. An ETD image is shown, overlaid with an EDS image (colored green) indicating the regions of high zirconium concentration, it is clear that the zirconium has predominantly deposited around the grain boundaries. (c) Photograph of the alumina crucible and YSZ media, post-anneal. The green discoloration is due to a reaction with the media, resulting in an oxide that has deposited on the YSZ media. 30

3.7 Image showing the configuration used for annealing in the SentroTech ST-1700. A (MgCoNiCuZn)O sintered pellet is protected from reaction with the crucible by using excess (MgCoNiCuZn)O powder that was confirmed to be single-phase (ground from a single-phase (MgCoNiCuZn)O pellet). 30

3.8 SEM EDS maps of annealed (MgCoNiCuZn)O. Atomic percent maps of Mg, Co, Ni, Cu, Zn and O, shown for pellets annealed at 1300-1700 ºC alongside the un-annealed sample. Quantification was done using the $K\alpha_1$ transitions. The rocksalt particles are homogeneous in Mg, Co, Ni and Zn, with a decreasing Zn concentration with increasing temperature due to sublimation. 32

3.9 Composition and morphology of (MgCoNiCuZn)O sintered pellets following high temperature annealing. SEM EDS of pellet following annealing at up to 1700 ºC showing inhomogeneous distribution of Cu following annealing. Regions of high Cu concentration are observed between rocksalt particles after annealing. There is still a non-zero Cu concentration in the rocksalt particles, however it is not easy to see in the EDS maps due to the much larger segregated Cu concentration. Images were taken using an ETD and colored using the Cu concentration maps collected using EDS. . . . 33

3.10 XRD patterns following annealing and air-quenching of (MgCoNiCuZn)O. XRD data for an as-sintered pellet (1100 °C for 18 hours) of polycrystalline (MgCoNiCuZn)O (as shown in **Figure 3.5**) and the same (MgCoNiCuZn)O pellet after annealing for 2 hours at the given temperature and subsequent air quench. The peak intensity ratios for the as-sintered sample are typical of a rocksalt structure. Following annealing, the peak intensity ratio of the XRD of the samples is varied, often with an increase intensity for the 220 peak. It is possible that this is due to local structure or distortions. It has also been suggested that it could be due to a change in the Jahn-Teller effect, due to the loss of Cu during the anneal[191]. No secondary phases (tenorite-CuO or wurtzite-ZnO) are observed. Datasets are offset vertically for clarity. 35

3.11 Selective loss of Cu and Zn at high temperature in (MgCoNiCuZn)O. (a) SEM EDS data showing the cation atomic percent of a rocksalt particle surface following a 2-hour dwell at the given temperature. The 20 °C sample is as-sintered and has not undergone an annealing treatment. Errors are the error in the fit according to the SEM software. Lines have been added to help guide the eye along the changes in each elemental composition and sum to 100%. Additionally, the calculated configurational entropy (S) of each composition, is shown in the bottom panel, along with the entropy-temperature (TS) product. The dotted lines represent the expected S/k_B values for ideal 5-, 4- and 3- component systems respectively, calculated using **Eq. 3.1**. We observe that significant losses in Cu and Zn occur, and correspondingly this results in a drop in entropy. (b) The experimental lattice parameters and errors as determined using Rietveld refinement for the $K\alpha_1$ peaks in **Figure 3.10**, along with the Vegard's law estimate using the compositions from (a). The Vegard's law[199] calculation was done using experimental values for MgO, CoO, and NiO, and using the octahedrally coordinated ionic radii[200] for Cu^{2+} and Zn^{2+}, to estimate the lattice parameter of rocksalt CuO and ZnO. While individual points have poor correlation, the overall trend between the change in Vegard's law and the measured lattice parameter is similar. 36

3.12 Comparison of observed Cu and Zn composition to maximum solubility at the solidus. The copper concentration in (MgCoNiCuZn)O is observed to correspond roughly with the solubility of Cu in the rocksalt-Cu oxide binary systems in the 1300 – 1700 ºC range. We note the observed Zn composition in (MgCoNiCuZn)O is much lower than the maximum solubilities in the associated binary oxide constituents and that the Cu and Zn concentrations are correlated. Produced by combining **Figure 3.4** and **Figure 3.11**. 38

4.1 (a) Schematic photonic structure comprised of alternating layers of high and low refractive index (MgCoNiCuZn)O films, deposited at different substrate temperatures. (b) Refractive index variation with wavelength for (MgCoNiCuZn)O films grown at 200 ºC and 600 ºC. Adapted from [171]. 43

4.2 XRD data showing an as-deposited multilayer of (MgCoNiCuZn)O deposited at alternating temperatures of 200 and 400 ºC and XRD data following an anneal at 400 ºC for 2 hours, showing only one diffraction peak, indicative of intermixing of the two previously distinct structures. 43

4.3 XRD data showing an as-deposited film of (MgCoNiCuZn)O deposited at a substrate temperature of 200 ºC and XRD data following an anneal at 700 ºC for 2 hours and 1100 ºC for 2 hours. Following annealing at 700 ºC, a secondary phase peak is observed, while after annealing at 1100 ºC, no film is observed. 45

4.4 (a) AFM image collected using an NT-MDT NTEGRA and (b) SEM image both confirming the presence of particles following dewetting. SEM images were obtained using a Thermo Fisher Scientific Helios 650 Nanolab. 45

4.5 (a) Alternating films of $BaZr_{0.5}Hf_{0.5}O_3$ and MgO are chosen because of their low lattice mismatch and high melting temperatures. The high quality epitaxy will limit grain growth at extreme temperatures. (b) $BaZr_{0.5}Hf_{0.5}O_3$ and MgO are refractory oxides with dissimilar crystal structures. (c) Experimentally measured refractive indices of $BaZr_{0.5}Hf_{0.5}O_3$ and MgO[28]. The refractive indices of MgO and $BaZr_{0.5}Hf_{0.5}O_3$ were measured through spectroscopic ellipsometry and thermal emission infrared spectroscopy. Over the wavelength range of 0.4 – 1.6 μm the refractive indices were measured up to 1100 ºC using a custom-built, tip tilt hotstage on a Woollam M-2000 ellipsometer. 47

4.6 XRD analysis of the $BaZr_{0.5}Hf_{0.5}O_3$ target revealing that the target is predominantly composed of $BaZrO_3$ and $BaHfO_3$ perovskite phases, with some HfO_2 impurity phase. 48

4.7 Average background subtraction filtered, up-scaled atomic resolution STEM-EDS image of Ba and Hf cations in the $BaZr_{0.5}Hf_{0.5}O_3$ phase. The arrangement is consistent with a perovskite structure with Ba on the A-site and Hf on the B-site. 49

4.8 (a) XRD data showing in-situ annealing of a $BaZr_{0.5}Hf_{0.5}O_3$ single thin film at temperature intervals from 300-1100 ºC. No change was observed between the as-deposited film and the film at 300 ºC. At approximately 900 ºC, a secondary phase is observed at around 34º. (b)XRD data showing in-situ annealing of a $BaZr_{0.5}Hf_{0.5}O_3$ and MgO superlattice at temperature intervals from 300-1100 ºC. Similarly, at approximately 900 ºC, the same secondary phase is observed at around 34º. The peaks from the AlN X-ray diffraction (XRD) heater are also marked. 50

4.9 XRD data showing an as-deposited superlattice, as well as samples annealed in dry air at 1100 ºC for 24 hours, 1200 ºC for 2 hours, 1350 ºC for 2 hours and 1500 ºC for 2 hours. The same sample was used for the 1100 ºC and 1200 ºC anneals. Due to degradation other samples (deposited concurrently to the first) were used for the remaining anneals. 51

4.10 XRD data showing an as-deposited superlattice, as well as following a 168 hour anneal at 1100 ºC in dry air. 51

4.11 (a) STEM-HAADF imaging of the $BaZr_{0.5}Hf_{0.5}O_3$ superlattice prior to and (b) post-anneal, highlighting the preservation of the epitaxial flat interface at the substrate. (c) Superlattice layers 1-10 showing the layer roughness and intermixing prior to and (d) post-anneal. (e) EDS line scan along the above images, showing the conservation of distinct compositional regions before and (f) post-anneal. (g) analysis of the interface roughness showing no change prior to and (h) post-anneal. Roughness increases in the growth direction due to thermodynamic conditions during synthesis. 53

4.12 (a) Schematic illustrating the optical characterization setup utilizing emission from a SiC heater. (b) Optical measurements of a $BaZr_{0.5}Hf_{0.5}O_3$/MgO photonic crystal with two-and-a-half bilayers demonstrating suppression of thermal emission. (c) Transmission spectra of $BaZr_{0.5}Hf_{0.5}O_3$/MgO photonic crystals with varying bilayer thicknesses, before and after annealing at 1100 ºC for 12 hours in dry air. The change in optical transmittance is negligible following annealing. 55

4.13 (a) XRD data from a $BaZr_{0.5}Hf_{0.5}O_3$/MgO photonic crystal with two-and-a-half bilayers deposited on an MgO (001) substrate, exhibiting a textured polycrystalline structure. $BaZr_{0.5}Hf_{0.5}O_3$ polycrystalline film peaks are labeled. (b) Model (ideal reflector) calculated versus experimental transmittance data for a partially polycrystalline $BaZr_{0.5}Hf_{0.5}O_3$/MgO photonic crystal, with a significant discrepancy between the expected and measured results. 55

4.14 SEM images collected using an ETD, displaying the surface structure and a cross-sectional structure (following cleaving) of a photonic crystal with two-and-a-half bilayers. A schematic of different film growth modes is included, with Stranski-Krastanov, the most likely growth mode, highlighted. 57

4.15 Top-down SEM images illustrating strain evolution. (a) A single $BaZr_{0.5}Hf_{0.5}O_3$ thin film exhibits a growth mode that includes the formation of square islands. In a (b) superlattice with 8 bilayers, a mixture of square and triangular islands are observed. In (c) and (d) with increasing number of layers, a significant increase in triangular island density is observed. In the photonic crystal (~ 2 μm thick) sample, these islands appear to have fused to form an uneven surface. 58

4.16 Cross-sectional STEM-HAADF imaging along the <100> direction of the substrate. (a) A significant number of defects are observed that extend from the bulk of a superlattice with 14 bilayers through the surface. (b) Image of an isolated defect in a superlattice sample with 10 bilayers, appearing to originate from a defect in the fourth $BaZr_{0.5}Hf_{0.5}O_3$ layer (first layer shown in this image). (c) EDS of the same region showing no compositional variation across the defect. (d) and (e) EDS and HAADF intensity linescans from the regions marked in (b). The data in (d) is also shown in (e) for comparison. Linescan (e) shows clear anomalies in the composition and HAADF intensity at the origin of the defect and at the start of each subsequent layer, indicating that the protrusion is continued through the rest of the superlattice sample. 59

4.17 2D slice of Mg concentration from APT. (a) and (b) represent two 10 nm thick 2D slices through a 3D reconstruction of the defect, at perpendicular directions. 60

4.18 High temperature STEM. [(a)–(f)] STEM-HAADF images of a superlattice with 14 bilayers, held in-vacuo and at 1000 ºC in-situ over a period of 2 min at (a) 47, (b) 54, (c) 60, (d) 92, (e) 104, and (f) 164 s after reaching 1000 ºC. The star marks an approximately fixed position on the sample. (g) STEM-HAADF image of a partially degraded superlattice following cooling from 1000 ºC. (h) STEM-EDS mapping of Mg, Ba, Hf, and Zr composition of the region shown in (g) after heating for ~ 50 min at 1000 ºC. (i) STEM-HAADF image of completely degraded region of the superlattice following the same treatment as (g). (j) STEM-EDS composite image of Mg, Ba, Hf, and Zr concentration, illustrating the total loss of Ba. (k) Nanobeam diffraction of the region highlighted in (h) and (l) the calculated single crystal diffraction patterns for (k). 62

5.1 Occurrences of the term “ferroelectric” in publication titles on web of science[285]. Specific dates are identified from the relevant reports[268, 272–274, 279, 286–291]. Prior to 1945, the term ferroelectric was substituted for piezoelectric, as ferroelectric was not commonly used during this time period. 65

5.2 (a) GIXRD pattern of Si/W/$Hf_{0.5}Zr_{0.5}O_2$/W device stacks with a thickness of $\sim$ 10 nm. The dashed lines indicate the $\bar{1}11_m$ and 111_m reflections of the monoclinic $Hf_{0.5}Zr_{0.5}O_2$ phase and the non-equilibrium $Hf_{0.5}Zr_{0.5}O_2$ phases, namely the $111_{(o-p)}$ polar orthorhombic, 101_t tetragonal and $211_{(o-ap)}$ anti-polar orthorhombic phases. (b) 1×1 μm area AFM topography of $Hf_{0.5}Zr_{0.5}O_2$ after crystallization and removal of the top electrode, showing an average grain size of 26.4 $\pm$ 0.2 nm and a root mean square (RMS) roughness of 1.1 nm. (c) $Hf_{0.5}Zr_{0.5}O_2$ ferroelectric loop measured at 100 kHz. (d) Through-microscope photograph of the electrode configuration of $Hf_{0.5}Zr_{0.5}O_2$ nanodevice following ion milling to form a ferroelectric pillar under a larger top electrode for contacting with RF probes. 69

5.3 (a) Circuit design illustrating the use of a pulse generator and oscilloscope to achieve RF measurements, FE represents the ferroelectric devices, which can be considered a variable capacitor. Also shown are the “write” pulse, used to rapidly cycle the ferroelectric without recording polarization at a high duty cycle ($\sim$ 18%), and the slower “read” pulse, used to record the polarization of the ferroelectric device after a significant number of cycles. These positive-up-negative-down (PUND)-like pulses ensure that the device is reset prior to polarization measurement (2 P_r measurement). (b) Polarization ($2P_r$) evolution under an applied field of 3 MV cm^{-1} with cycling up to nearly 10^9 full cycles shown for device diameters of 0.4 to 10 μm. An increase in $2P_r$ is observed before a sudden failure occurs. (c) Cumulative cycle count at failure of $Hf_{0.5}Zr_{0.5}O_2$ device. Due to the distribution of “read” pulses, failure occurred at an unknown cycle between the filled and unfilled data points. Data is shown as ln(Cycles) vs inverse temperature to allow for a linear fit based on an Arrhenius equation (**Appendix D**). 71

5.4 (a) Under the application of a DC voltage, oxygen vacancies move in the direction of the applied bias, accumulating at the ferroelectric-electrode interface. (b) Under the application of a AC voltage, the oxygen vacancies do not move toward either electrode. Instead, the applied field lowers the diffusion barrier, resulting in increased lateral movement, following a random walk. This can eventually lead to oxygen vacancies accumulating and becoming pinned at the grain boundaries, forming a conductive filament. 72

5.5 Area dependence of the cumulative cycles to failure shown in **Figure 5.3.** Failure occurred at an unknown cycle number between the filled and unfilled data points. It is observed that the number of cumulative cycles to failure depends upon both device size and temperature. 75

5.6 (a) Field-modulated diffusion barrier (activation energy) extracted from the fit of **Figure 5.3(c)**, demonstrating a reduction from the reported thermal diffusion value of 1.02 $\pm$ 0.24 eV [337]. (b) Measurement of leakage current in devices measured in **Figure 5.3** following failure is area independent (at a field of 3 MV cm^{-1}), suggesting a localized failure mechanism such as the conductive filaments that are observed in HfO_2-based memristive devices[321, 344]. (c) Topography of a failed $Hf_{0.5}Zr_{0.5}O_2$ device following the removal of the top electrode. (d) It was demonstrated that it is possible to write a conductive filament using a voltage applied by a conductive-AFM tip. High conductivity regions are shown in green, overlaid with the topography from (c). This image was acquired by sourcing a voltage of 1 V through the tip, operated in contact mode. Conductive filaments were written using a voltage of up to 4 V. 76

5.7 (a) Field simulation showing entire device structure, with a field of 3 MV cm^{-1} applied to the top electrode and grounding the bottom electrode. TE is the W top electrode, FE represents a uniform $Hf_{0.5}Zr_{0.5}O_2$ ferroelectric layer, and BE is the W back electrode. (b) Field simulation showing an enlarged view of the edge of the ferroelectric capacitor, exhibiting field amplification at the TE-FE-SiO_2 junction. (c) Horizontal line scan showing electric field as a function of position, starting at the left edge of the FE device (0 nm), an increase of $> 20\%$ is observed at this edge. 76

6.1 Schematic relationship between composition of high entropy oxide (MgCoNiCuZn)O and expected stability and functionality. Linear plots are shown only as a guidance and any real dependence is likely to be far more complex. 80

6.2 Illustration of the differences between a multistructural high entropy oxide, such as $Mg_{0.2}Co_{0.2}Ni_{0.2}Cu_{0.2}Zn_{0.2}O$ ((MgCoNiCuZn)O) and a monostructural oxide such as $Ba(Ti_{0.2}Zr_{0.2}Nb_{0.2}Sn_{0.2}Hf_{0.2})O_3$, a potential perovskite high entropy oxide. Note that the structures with red arrows are contributing a negative enthalpy of formation (ΔH_f) that could contribute to disrupting the stability of the high entropy material 82

6.3 Illustration of the effect of doping $BaZrO_3$ with $BaUO_3$ on lattice parameter and melting temperature. Note that while a Vegard's law approach is used for composition, temperature is only illustrated schematically based on typical solidus lines observed for many fully miscible phase diagrams. 83

A.1 Computed binary phase diagrams for ZnO-rocksalt oxide. (a) ZnO-NiO, (b) ZnO-MgO, (c) ZnO-CoO. This is shown along with the relevant experimental data plotted in **Figure 3.3**. 85

B.1 Cu-rich region analysis. A peak in the volume fraction of Cu-rich regions occurs at around 1400 ºC, close to the melting temperature of tenorite CuO. The volume fraction has been calculated by analyzing the SEM EDS images of Cu concentration, as well as by a lever-rule[375] calculation, using the average Cu concentration of (MgCoNiCuZn)O particles and the overall Cu concentration of the region. Volume fraction analysis was performed using ImageJ Software[376]. 89

B.2 SEM EDS linescan of (MgCoNiCuZn)O annealed at 1600 ºC. Atomic percent linescan of Mg, Ni, and Co concentration in at% across the center of the annealed pellet. A Savitzky-Golay filter was used to smooth the data. Red-highlighted surfaces were the surfaces exposed during the annealing treatment. There is a clear increase in concentration of Mg at both surfaces of the pellet that were exposed during the heat treatment. Solid lines note the average cation composition over this region.. 90

C.1 The screening process consists of five main steps. (1) An oxide substrate with a high melting point (over 2,000 ºC) is selected. (2) The Materials Project database is queried to gather properties of candidate oxide pairs. (3) Lattice-compatible pairs are identified by considering stable configurations between the different oxides and a lattice misfit strain cutoff of 5% is applied. (4) Candidates are filtered by applying a bandgap cutoff of 2 eV and evaluated based on the criteria of minimal lattice strain and maximum refractive-index contrast. (5) Down-selected candidates are assessed using the available experimental data (for example, melting points). $MgO/BaZrO_3$ (top) and $LaAlO_3/CeO_2$ (bottom) are two example systems that have minimal lattice strain, different crystal types, high melting points and contrasting refractive indices. 93

LIST OF APPENDICES

A Calculations of Wurtzite ZnO Solubility in Rocksalt Oxides, MgO, NiO and CoO . . 85

B Additional Measurements of (MgCoNiCuZn)O 89

C Selecting Nanophotonic Materials 91

D Filament Formation Kinetics 94

LIST OF ACRONYMS

AC alternating current

AFM atomic force microscopy

ALD atomic layer deposition

APT atom probe tomography

BCC body-centered cubic

CMOS complementary metal oxide semiconductor

CTE co-efficient of thermal expansion

CVD chemical vapor deposition

DC direct current

DFT density functional theory

DRAM dynamic random access memory

EDS energy-dispersive spectroscopy

ESOs entropy-stabilized oxides

ETD Everhardt-Thornley detector

FCC face-centered cubic

GIXRD grazing incidence X-ray diffraction

HAADF high-angle annular dark field

HCP hexagonal close-packed

HEAs high entropy alloys

HEOs high entropy oxides

(MgCoNiCuZn)O $Mg_{0.2}Co_{0.2}Ni_{0.2}Cu_{0.2}Zn_{0.2}O$

PLD pulsed laser deposition

PUND positive-up-negative-down

PVD physical vapor deposition

RF radio frequency

RMS root mean square

RSM reciprocal space map

SEM scanning electron microscopy

STEM scanning transmission electron microscopy

TEM transmission electron microscopy

TPV thermophotovoltaic

XRD X-ray diffraction

XRR X-ray reflectivity

YSZ yttria-stabilized zirconia

ABSTRACT

With materials being pushed to further and further extremes in the name of improved performance, understanding failure mechanisms through phase stability and defect mobility in materials subjected to extreme conditions is more important than ever before. While high temperatures may be the most synonymous extreme condition, there are a number of other external stimuli that could be considered extreme, including strain, electric field, and chemical environment. For each condition, there are many unique failure mechanisms that can occur, such as phase segregation, corrosion, and degradation of functional properties. These failure mechanisms can be understood through the mobility of defects such as oxygen vacancies, or the relative stability of each phase.

Metal oxide materials often exhibit exciting and unique functional properties, such as magnetism and ferroelectricity. The primary aim of this work is to understand the stability of these materials under numerous extreme conditions and to relate this stability to the underlying failure mechanism.

The first material, a high entropy mixed oxide, $Mg_{0.2}Co_{0.2}Ni_{0.2}Cu_{0.2}Zn_{0.2}O$, is predicted to be highly stable, due to the configurational entropy in the system, that is believed to dominate the Gibbs' free energy at high temperatures. The stability is investigated in bulk and thin film composite systems, where tunable optical properties would allow for the production of reflecting filters. The stability is lower than expected, with bulk failure occurring due to phase segregation of the oxide components that possess an unfavorable enthalpy of formation, CuO and ZnO, following annealing above 1300 ºC. By 1700 ºC, this results in the formation of a nearly pure rocksalt oxide, retaining $< 5\%$ Cu cation concentration and negligible Zn concentration, this rocksalt phase is evidently highly stable, but lacks the functional properties of the high entropy oxide. Failure of the thin film optical system occurs through issues with miscibility and dewetting at even lower temperatures.

The failure of the $Mg_{0.2}Co_{0.2}Ni_{0.2}Cu_{0.2}Zn_{0.2}O$ thin film systems motivates the investigation of a different oxide system. This system, consisting of alternating thin films of $BaZr_{0.5}Hf_{0.5}O_3$ and MgO, is shown to possess suitable optical properties, and to retain these properties following annealing at 1100 ºC in air. The failure of this system occurs through the loss of Ba ions from the $BaZr_{0.5}Hf_{0.5}O_3$ layer, resulting in the formation of an (Hf, Zr)O_2 phase, occurring preferen-

tially around strain-induced defect structures formed during the deposition. Nonetheless, this system demonstrated a 10% improvement in thermophotovoltaic spectral control (relative to the prior state-of-the-art value) at an extreme temperature in an oxidizing environment.

The observed formation of an (Hf, Zr)O_2 phase under these extreme conditions illustrates the high stability of this system. As a ferroelectric material of interest to the semiconductor industry, the stability of $Hf_{0.5}Zr_{0.5}O_2$ under extreme electric fields was investigated, with failure occurring through the formation of a conductive filament. The filament is able to form due to the lowering of the activation barrier for charged particle motion under an electric field. For oxygen vacancies in $Hf_{0.5}Zr_{0.5}O_2$, this work reports a lowering of the barrier by ~ 0.8 eV, compared to the thermal diffusion barrier, under a field of 3 MV cm^{-1}.

The outcome of this work is an improved understanding of the failure of highly stable functional oxide materials subjected to extreme conditions. This understanding should be utilized to further the development of novel highly stable oxide materials.

CHAPTER 1

Understanding Extreme Conditions

When considering extreme conditions, it is easy to make the mistake of only thinking of extreme temperatures. However, besides high temperatures, there are many other external stimuli to which the term extreme conditions could apply. These can include certain environments, such as oxidizing or evacuated atmospheres. Or the application of external fields, such as electric or magnetic fields. Or even internal mechanisms, such as extreme strains between a substrate and a thin film. Some of the relative energy scales of these external stimuli are illustrated in **Figure 1.1**[1].

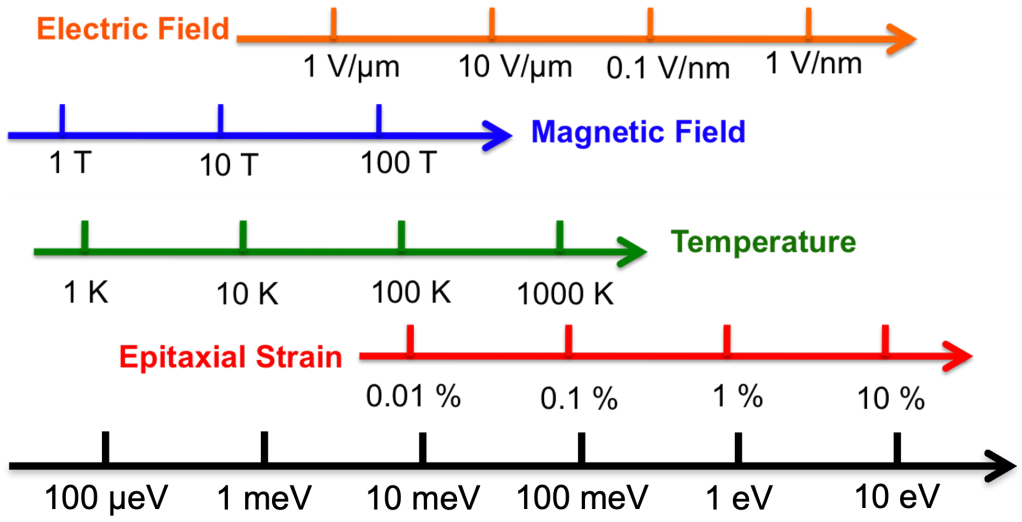


Figure 1.1: Illustration of the energy scales of different external stimuli. Adapted from [1].

1.1 A case study on stability in extreme conditions

An excellent example of materials regularly subjected to extreme conditions are the superalloys and their accompanying thermal barrier coatings that are used in airplane jet engines[2]. These

materials are not only subject to high temperatures and many thermal cycles, but also extreme stresses, at times in excess of 20 atmospheres[3]. These are a material that have been pushed to further and further extremes to match an increased demand for performance to keep up with rising fuel costs. In gas turbines, an increase in temperature generally results in an improvement in efficiency, as such, the operating turbine inlet temperature of these turbines has intentionally been increased over the years[3]. In fact, the inlet temperature has increased so much as to be beyond materials capabilities, requiring clever feats of engineering such as thermal barriers and complex cooling systems, allowing the inlet temperature to reach over 1600 ºC in recent systems[4, 5]. At these inlet temperatures, without cooling, even these highly complicated superalloys would melt, and even with cooling they can be subject to significant creep. The gap between material capability and gas inlet temperature is clearly observed in **Figure 1.2**, where it is clear that with the development of cooled turbine blades, there was a decoupling of material capability and inlet temperature.

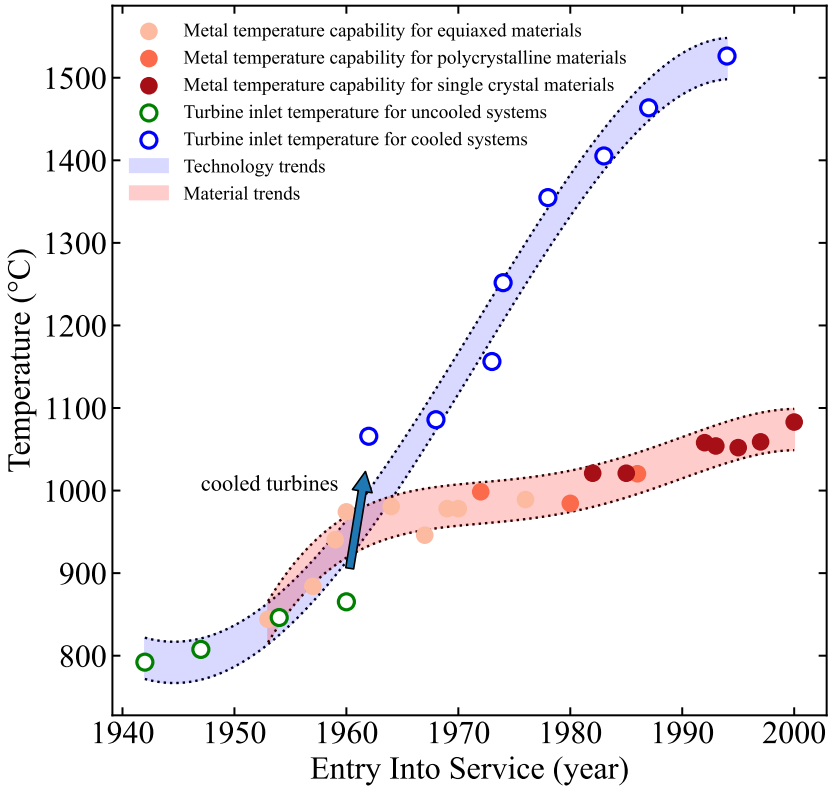


Figure 1.2: Evolution of turbine material capability and of turbine gas inlet temperature. Adapted from data in [6]. With inlet temperatures ever increasing to improve engine efficiency, we observe a divergence of metal turbine temperature capability, and the actual operating temperatures of the turbine. This is achieved through the use of internal cooling structures and thermal barrier coatings.

While the extraordinary development of jet engines and superalloys is mainly a feat of engineering mechanical properties in a metal, the same principles can be applied to functional materials. Additionally, many of the same failure modes occur when subject to extreme stimuli. For the case of temperature, some typical failure modes include grain growth, oxidation (corrosion) and creep[7, 8]. Additionally, for materials in contact with other materials, such as coatings, delamination, interdiffusion and other diffusion related processes can be the cause of failure[9, 10]. These are failure modes that superalloys have been designed to prevent, the use of single crystal materials eliminates grain growth, while careful alloying can help to alleviate oxidation issues[11, 12]. While materials subject to other extreme stimuli, such as field or strain, might experience different failure modes, these failures modes are often mediated similarly, through the motion of defects, vacancies and impurities, or by changes in phase. These processes can be activated thermally, or through other energies such as charged particles in a field or interaction with strain[13, 14].

1.2 Functional oxide materials

In a similar manner, many functional materials are being pushed to further and further extremes with the goal of achieving improved performance. Materials that allow for increased fields or increased operating temperatures than today's state of the art can improve performance in many applications and industries. Ceramic materials, such as oxides, can have advantages under certain conditions when compared to metals such as superalloys, including corrosion (oxidation) resistance[15, 16]. In fact, the use of protective oxides is already prevalent in the turbine industry due to the required oxidation resistance[17]. Besides this, many interesting functional properties, such as semiconductor properties or ferroelectricity are also exhibited by ceramic materials[18].

Oxide nanostructures, in particular, have become an important class of materials, used widely in computation, energy collection, and storage[19]. There are a number of examples of oxide-based devices that could be improved by new materials or new processing that allows operation at a higher temperature or under a higher field. Although accompanied by an increase in performance per watt, CPUs are generally operating at higher frequencies and higher power consumptions than ever before[20]*, with power consumption expected to increase by approximately 7% per year[21]. This increases the likelihood of failure of these devices, which can be managed through several different approaches. Further work can be invested to reduce the power consumption of these devices, by investing in novel materials. More aggressive cooling solutions can be used to maintain

*An interesting fact to note is that many computer uses will choose to "overclock" their CPU, that is increasing the operating voltage to increase frequency (improve performance) at the expensive of potentially a shortened component lifetime, demonstrating the potential for improved performance under more extreme conditions, at the cost of stability[22–24].

device temperature and improve operation without any direct change to the CPU. Or the device stability can be improved at these extreme powers through understanding of the failure mechanism and adaptive design of materials processing.

Another example is thermophotovoltaic (TPV) systems, to efficiently convert heat to electricity, it is desirable to have devices operate at ultra-high temperatures. An increase of operating temperature from 1200 ℃ to 1800 ℃ has been predicted to an efficiency enhancement of almost 10%[25, 26]. It is possible to further increase the efficiency of these TPV systems by utilizing spectrally selective filters, however, it is also necessary for these systems to be stable at comparable temperatures due to their proximity to the rest of the TPV system[27]. The relationship between emitter temperature and figure of merit for TPV systems is shown in **Figure 1.3**, showing a generally positive correlation between increased temperature and increased performance.

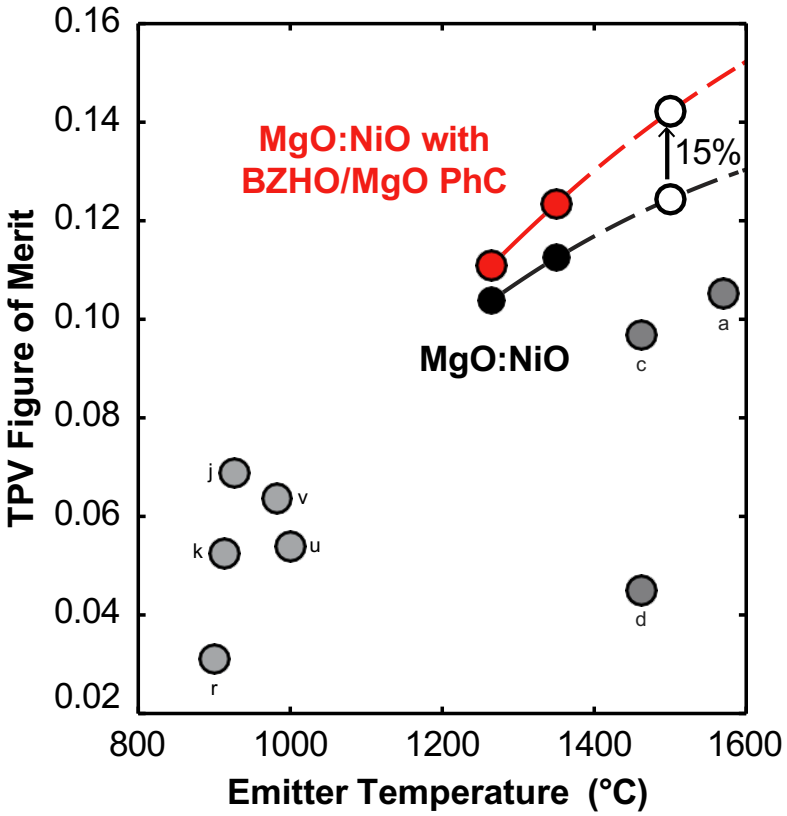


Figure 1.3: Estimate of TPV efficiency as a figure of merit versus emitter temperature, comparing different emitter plus filtering approaches in different atmospheres, including several data points for a single MgO:NiO based TPV system. Generally, a higher efficiency is observed for higher emitter temperatures, requiring more stable filtering solutions. Adapted from [28]. Data collected from [29–34].

A further complication is composite structures, in addition to all the stability considerations listed above, composite materials must also be stable while in contact with each other. This can mean that these materials need similar lattice parameters, similar coefficients of thermal expansion, and to be immiscible, that is to not interdiffuse. Nevertheless, realizing nanocomposite functional materials that are stable in extreme environments such as high temperature is a key challenge for many applications. Nanocomposite structures, such as nanoparticles matrices, aligned nanocomposites, and superlattices exhibit many exciting properties, such as multiferroicity, negative capacitance and directional emission to mention a few[35–45]. Many TPV systems actually make use of nanocomposites, utilizing a reflective coating to control thermal emission at elevated temperatures[46]. For many of these applications it is important that the coatings are highly crystalline, to prevent grain growth related failure modes. However, the production of highly crystalline nanocomposites with high temperature stability requires careful materials consideration. This greatly limits the number of available configurations[47]. Besides grain growth, other common issues for nanocomposites like this include thermal stresses, delamination, oxidation and intermixing[48, 49].

1.3 Failure mechanisms

It is clear that there is an ever present driving force in many industries, pushing materials further and further to extremes to try to achieve improved performance. As important as the development of new, increasingly stable materials, is the understanding failure mechanisms of the current materials selection available. A deeper understanding of material failure can lead to a change in processing or environment that can result in an improvement in the stability of that material. Or, this deeper understanding can be used to development future materials, more resistant to the problem failure mechanisms identified for a particular material or application.

As mentioned above, typical failure mechanisms will vary with material and application, with bulk and nanomaterials often exhibiting very different failure mechanisms. In bulk materials, common failure mechanisms include phase transformation, grain growth, corrosion, fatigue-based failure and creep under load[8, 50, 51]. While for the thin films, grain growth and phase transformation are potential failure mechanisms, many thin film failure modes are closely related to diffusion or strain. Examples of these include misfit dislocations formed through strain relaxation, migration of vacancies or defects, delamination or interdiffusion with the substrate material or other film layers[52–57]. These failure mechanisms are primarily related to or further activated by temperature or strain, but they can also be enhanced by the application of other stimuli such as electric field. Stimuli related to functional properties, such as electric field, also have some unique

failure modes, such as the breakdown of dielectric materials under very large fields, the formation of conductive regions through the migration of vacancies, or electromigration[58]. Electric fields are even capable of driving phase transformation in some materials[59–61]. Although many of these failure mechanisms are clearly linked, we need to examine and understand each failure mode separately to understand the behavior of materials under extreme conditions.

1.3.1 Phase transformations

While phase transformations can place an intrinsic limit on the temperature stability of a material, this type of failure is often easily predicted due to computational models and the abundance of phase diagrams in the literature, over 29000 are reported in the NIST database[62, 63]. A schematic phase diagram is shown in **Figure 1.4**. Phase transformations induced by other stimuli, such as stress-strain or applied electric field can be harder to predict. While in structural materials, phase transformation may result in a loss of mechanical properties, in functional materials, phase transformation is often considered a failure mode due to the loss of some desirable functional property[64–66]. In more complex oxide materials, partial phase changes can be common under elevated temperatures, as solubility of each component may vary significantly with temperature. Even the loss of a small proportion of one component can cause the degradation of functional properties in many doped materials. Certain material phases can be stabilized in thin films, through the use of epitaxial templating, allowing for phases to be stable under conditions at which they may not be in bulk[67].

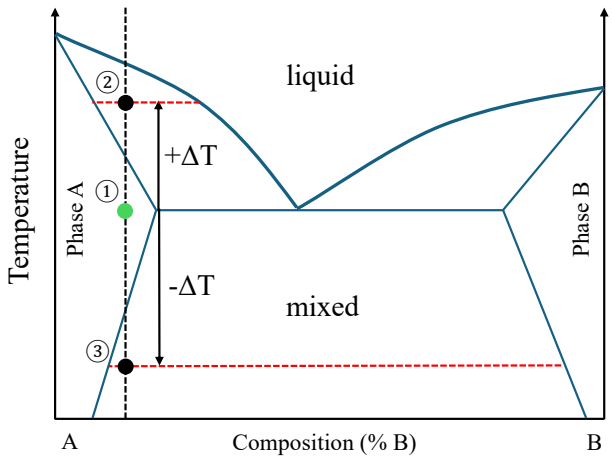


Figure 1.4: A schematic phase diagram of a simple eutectic system. Starting from ①, a single phase (A) composition a change of +ΔT or - ΔT will result in a phase transformation into a mixed (A + liquid, ②, or A + B, ③) phase. Although this is illustrated for temperature, it is also possible to cause this transformation with other stimuli, such as strain or electric field.

1.3.2 Grain growth

Grain growth occurs at elevated temperatures in polycrystalline or nanograined materials, including nanostructures such as thin films. The driving force behind this is a reduction in grain boundary energy[68]. There have been many proposed models [69–71]. It is generally considered that grain growth is the result of grain boundary migration, through the detachment of atoms from one grain and attachment to another. There is an energy barrier associated with this process, and additionally, elevated temperatures and the presence of vacancies can increase migration rates through enhanced diffusion[72]. Grain growth failure can also be induced through stress based recrystallization[73].

In both bulk and nanostructured systems, grain growth can be managed by careful control of the initial grain structure. In many cases, amorphous or polycrystalline materials can be recrystallized into a more desirable grain structure, with better properties and greater stability[74]. In this case, grain growth is desirable, as it is happening as the result of an intentional annealing process, however grain growth failure is unwanted grain growth when a material is subject to an external stimulus. In ideal cases, a single crystalline material could be used to completely eliminate grain growth, as in the case of turbine blades (**Section 1.1**). However, the anisotropic properties of single crystals are not desirable in certain applications, or the fabrication of a single crystal may not be feasible.

1.3.3 Corrosion (Oxidation)

Corrosion encompasses a vast number of failure mechanisms, dependent highly upon the material and the environment, of which there is a broad array[75]. Corrosive environments include oxidizing, acidic, alkaline, underground, humid/moist, and any number of combinations of these[76]. Here we are going to focus primarily on oxidation based corrosion. At extreme temperatures, even our atmosphere can be considered corrosive to many materials due to the presence of water and oxygen. Reaction with these compounds can result in structural degradation or sometimes, the evolution of a gaseous product. These issues are typically worse at elevated temperatures, with diffusion driven high temperature oxidation is one of the most important failure mechanisms of protective thin films in industrial applications[77, 78]. Oxidation, and corrosion in general, can be managed through careful material selection, considering the operating environment. Metals are typically susceptible to many types of corrosion, while ceramics are often more resistant, particularly to oxidation. Because of this, metals may often be coated with a protective oxide or make use of a protective oxide scale or sacrificial anode[79, 80]. While many oxides are not susceptible to corrosion through oxidation, reactions with water to form hydroxides can often be problematic[81].

1.3.4 Fatigue

There are a number of fatigue based failure mechanisms, such as thermal cycling, electric field cycling, or load cycling. Typically, load-based fatigue failure involves the propagation of existing imperfections under loads well below the yield stress of the material[82, 83]. All materials, regardless of fabrication technique or processing, will contain some level of defects. Under cycling these defects will evolve into a macroscopic crack that can eventually lead to the failure of the material, due to fracture. Thermal fatigue occurs through a similar mechanism, the propagation of existing defects, however this occurs due to thermal strains, either a result of localized heating or of materials with different coefficients of thermal expansion and can occur in loaded or unloaded materials[84]. Although thin films also contain intrinsic defects, fatigue typically occurs at the interface between materials, either the film-substrate interface, or an interface between two films, as there are not likely to be any significantly sized flaws in such a small volume of material[85].

Electric field fatigue failure can vary depending on the electrical properties of the material. In electronic materials such as ferroelectrics, fatigue based failure is often associated with an increase in non-switching volume, through mechanisms such as the pinning of domains or transformation to a non-polar phase[86]. Because of this, the fatigue of ferroelectric materials is typically highly related to the presence of charged point defects, for example, oxygen vacancy density[87–89]. In memristive devices, fatigue is often associated with undesired reactions of the dielectric layer and electrodes, or random diffusion and overgrowth of the conductive filament responsible for the memristive properties[90].

1.3.5 Defect migration, interdiffusion and electromigration

Diffusion related processes are often a cause of failure at elevated temperatures. In composite materials, interdiffusion of the phases can result in structural or property changes, while in most materials, the presence of mobile defects, for example, oxygen vacancies, can be closely related to material failure and property degradation. These defects can enhance diffusion rates or agglomerate to form voids and other defect structures[91–94]. The migration of defects can result in the pinning of structures such as domain or grain boundaries, however this is a coupled process, the defects also become pinned at the locations. In some materials, a large enough density of defects can result in conductivity, through charge transport or the formation of conductive filaments, leading to high leakage currents[95–97].

Interdiffusion can be difficult to manage, depending largely on the selection of immiscible materials. The Hume-Rothery rules provide a rough guideline to which atoms will be soluble, or conversely insoluble. If the atoms of one phase are insoluble in the other, then the two materials

can be considered immiscible, and thus will have limited interdiffusion. For a substitutional solid solution, the rules can be summarized as less than 15% difference in atomic radius, similar crystal structures, same valency and similar electronegativity. For an interstitial solid solution, the solute much have a radius below 59% of the solvent atoms, they must have the same valence, and similar electronegativity[98–100]. Therefore, the most direct way to design an insoluble composite is to select ions with different charge states and different sizes.

Defect migration is primarily managed by reducing defect concentration, typically done with a treatment such as plasma treatment, annealing or doping[101–103]. Electromigration is an analog of diffusion, as it is the movement of atoms due to an electric current[104, 105]. This can cause failure at material interfaces due to the formation of voids, but it can be mitigated by increasing the cross-section of the conductor, for example[106, 107].

1.3.6 Strain relaxation failure

Applying particularly to materials with confined dimensions, for example, thin film materials that have been deposited on a substrate, strain relaxation failure mechanisms include direct failure, such as delamination, cracking, and buckling[108–110], as well as secondary failure mode, such as the formation of defects like misfit dislocations, that can then result in failure through another mechanism or by disrupting further deposition[111–113]. These dislocations can also act as fast diffusion pathways, leading to failure through defect migration and interdiffusion mechanisms [114, 115]. Strains in film-substrate systems are introduced both through deposition, where the film is clamped to the lattice of the substrate, and also upon heating, due to difference in thermal expansion between the two materials. These issues are especially relevant to single crystal materials, which have no other strain compensation mechanism. Polycrystalline and amorphous materials do not typically experience such strains during deposition, due to the greater flexibility in atomic arrangement.

1.3.7 Dielectric breakdown

Dielectric breakdown occurs as an immediate and catastrophic failure, caused by a large electric field. There is also time-dependent dielectric breakdown, a failure mechanism where breakdown occurs as a result of a relatively low electric field over a long period of time[116]. During the process of dielectric breakdown, local materials transition from insulating to conductive through the generation of defects and broken-bonds[117]. This is more likely to occur in highly defective or oxygen deficient materials. While dielectric breakdown places an upper limit on the electric field that a device can withstand, time-dependent dielectric breakdown is more difficult to manage as many semiconductor devices make use of MOSFETs, where this type of failure is common. Many

factors influence time-dependent dielectric breakdown, including field, temperature, dielectric polarity and more.

This dissertation will seek to understand the stability of materials with the potential to be highly stable under extreme conditions such as temperature, strain and electric field. In each case, a link between material stability and failure mechanism is hypothesized. **Chapter 2** will review the experimental methods most used throughout this dissertation. **Chapter 3** describes high entropy oxides, which are predicted to be highly stable at extreme temperatures due to the configurational entropy. The phase stability of bulk (MgCoNiCuZn)O, the prototypical high entropy oxide, is investigated from 1300 ºC to 1700 ºC. **Chapter 4** further investigates thin film (MgCoNiCuZn)O as a component of a composite with an optical property focused approach before investigating the optical properties and strain-related failure of a more stable, novel system consisting of $BaZr_{0.5}Hf_{0.5}O_3$/MgO, capable of withstanding 168 hours at 1100 ºC in dry air without structural or functional degradation. It is found that the material fails through the formation of an HfO_2-based phase. **Chapter 5** further investigates a similar material, $Hf_{0.5}Zr_{0.5}O_2$, which is of particular interest as a relatively new ferroelectric material that could be integrated into the semiconductor industry. The high field and high cycle stability and the conductivity related failure mechanism are investigated in this system. **Chapter 6** details future directions for the development of materials that will be stable under extreme conditions.

CHAPTER 2

Experimental Methods

2.1 X-ray Diffraction

XRD can be utilized to assess the crystal structure of a material. This is particularly useful when investigating the stability of materials subjected to extreme conditions, as a before and after comparison of the crystal structure can quickly and simply reveal phase degradation. A number of different XRD techniques exist that can provide different information about both bulk and thin film materials.

2.1.1 Symmetric scan

Bragg's law[118] gives a condition under which it is possible to observe a beam that has diffracted from a sample. **Eq 2.1** gives the relationship between the incident angle θ, the planar (hkl) spacing d_{hkl} and the X-ray wavelength λ. This technique uses a symmetric configuration (angle of incidence equals angle of reflection). These X-rays are scattered from planes of atoms within the crystal, and hence provide information about the crystal structure[119].

$$2d_{hkl} \cdot sin(\theta) = n \cdot \lambda \tag{2.1}$$

where n is the diffraction order, which can generally be taken as 1. The lattice parameters of a unit cell where $a \neq b \neq c$ and ($\alpha = \beta = \gamma = 90$ °) can be determined using **Eq. 2.2**. For unit cells with angles not equal to 90 degrees (or hexagonal cells) the lattice parameters can still be calculated from the planar spacing, however it is much more complicated.

$$\frac{1}{d_{hkl}^2} = \frac{h^2}{a^2} + \frac{k^2}{b^2} + \frac{l^2}{c^2} \tag{2.2}$$

Therefore, the lattice parameter, $a(a \equiv b \equiv c)$, of a material with a cubic unit cell can be

calculated using **Eq. 2.3**, where $N^2 = h^2 + k^2 + l^2$.

$$\frac{1}{d_{hkl}^2} = \frac{h^2 + k^2 + l^2}{a^2} \quad \equiv \quad a = N \cdot d_{hkl} \tag{2.3}$$

This technique is typically used in a Bragg-Brentano geometry to measure the crystal structure of bulk crystals[120], but a modified geometry, known as parallel beam geometry can also be used to evaluate the crystal structure of thin film samples[121].

This parallel beam configuration also has a number of more specialized techniques, capable of discerning other properties of thin film samples, such as thickness, strain, or to improve the signal ratio of polycrystalline thin films, compared to the much higher intensity of the usually single-crystalline substrates on which they are deposited.

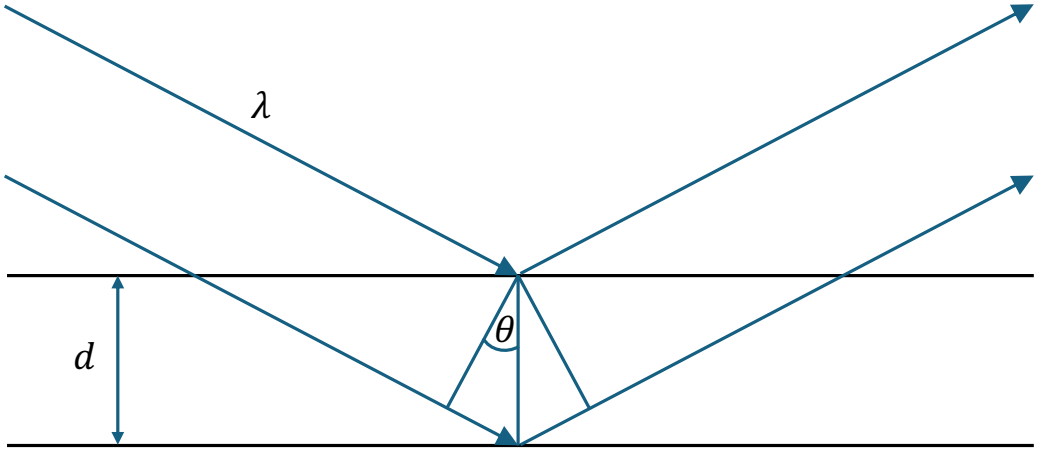


Figure 2.1: A XRD schematic, demonstrating the conditions for reflection, or Bragg's law conditions. Spacing between the planes is d and the angle of incidence is θ with a wavelength λ.

2.1.2 X-ray Reflectivity

X-ray reflectivity (XRR) can be used in a parallel beam geometry with thin film samples to analyze film thickness, roughness, superlattice periodicity and to some extent, density.

At angles below the critical angle, θ_c, the incident X-ray beam is totally reflected. These X-rays are reflected by each interface between different materials, depending on the difference in density. These reflected beams interact constructively and destructively, depending on angle, resulting in an oscillating pattern that can be fit to determine the film properties mentioned previously. A schematic showing the interaction of film parameters and XRR patterns for different samples is shown in **Figure 2.2**.

The θ values can be related to the thickness, t, of the film using the modified Bragg equation **Eq. 2.4**, where θ_i is the value of the maximum or minimum of the ith fringe, Δn is 1/2 and 0 for maximum and minimum respectively[122].

$$sin^2(\theta_i) = \theta_c^2 + (n_i + \Delta n)^2 \cdot \left(\frac{\lambda}{2t}\right)^2 \tag{2.4}$$

Additionally, the density can be related to the refraction index using **Eq. 2.5** [123], where n is the refraction index, Z_J is the atomic charges in the unit cell A_J is the atomic mass, and ρ is the mass density. As the critical angle is defined as $cos(\theta_c) = n$, which for small angles leads to $n = 1 - \theta_c^2/2$, this can be reduced to **Eq. 2.6**, where f' is the real part of the atomic dispersion relation[122].

$$n = 1 - 2.701 \times 10^{-6} \left(\frac{\sum Z_J}{\sum A_J}\right) \rho\lambda^2 \tag{2.5}$$

$$\theta_c^2 = 5.402 \times 10^{-6} \rho\lambda^2 \frac{Z + f'}{A} \tag{2.6}$$

When considering more complex situations, such as a film deposited on a substrate, or multilayer materials, these oscillating patterns are often fit using software, capable of extracting the thickness and density of each layer, provided sufficient signal-to-noise ratio and a non-negligible difference in refractive index (density) between the layers[124].

2.1.3 Reciprocal Space Mapping

A reciprocal space map (RSM) is produced by scanning the reflection from a peak with an in-plane component, and can be used to measure the orientation, texture and strain of deposited films. This technique also makes use of a parallel beam geometry.

This is done by aligning χ and ϕ (sample tilt and rotation) so that the out of plane reflection is perpendicular to the direction of scanning. Then a number of asymmetric $2\theta - \omega$ scans are completed. These real space θ values must then be converted to a reciprocal space coordinate, such as, Q_x or Q_z where x and z are lattice directions like [100] and [001]. This can be done using **Eq. 2.7** and **Eq. 2.8**.

$$Q_x = \frac{2\pi}{\lambda} \left(cos(\omega) - cos(2\theta - \omega)\right) \tag{2.7}$$

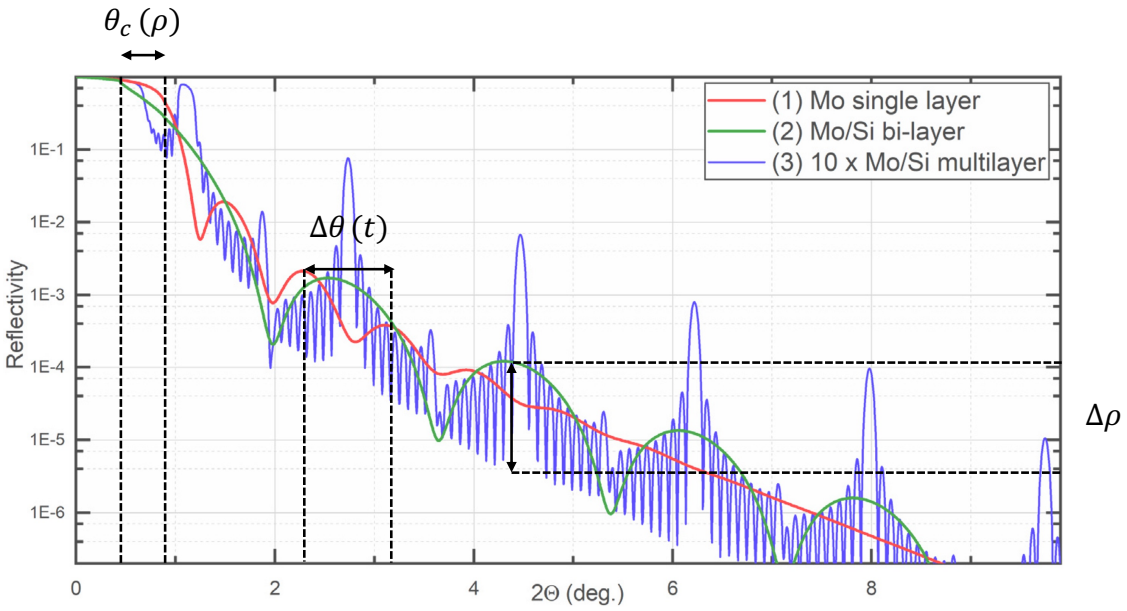


Figure 2.2: A XRR schematic, demonstrating the relations between film properties and observed patterns, using computed data. The density is determined from the critical angle, θ_c, where the intensity initially drops, while the period of oscillations, $\Delta\theta$ fits the film thickness, and the amplitude of oscillation is related to the difference in layer density, $\Delta\rho$. Not shown on the figure, the rate of intensity decay is related to the film roughness. Adapted from [124].

$$Q_z = \frac{2\pi}{\lambda}\left(sin(\omega) - sin(2\theta - \omega)\right) \tag{2.8}$$

From the relative positions of the film and substrate reflections it is possible to obtain both the in-plane and out-of-plane lattice parameters, and the strain state of the film. A fully relaxed film will have a reflection along the line that connects the origin of the reciprocal space and the reflection of the substrate peak. A fully strained film will fall along a line between the substrate reflection and the horizontal axis. This is demonstrated in **Figure 2.3**. Films are typically partially relaxed, as strain in thin films is often alleviated through the formation of misfit dislocations[125].

2.1.4 Grazing Incidence X-ray Diffraction

Another XRD technique that makes use of parallel beam geometry is grazing incidence X-ray diffraction (GIXRD). In GIXRD, the incidence angle, ω, is fixed to an angle slightly above the critical angle, θ_c and the detector is moved along the 2θ circle. The low angle of incidence results in a significantly lower penetration depth, and so the intensity of the film peaks is enhanced compared to those of the substrate in a typical parallel beam geometry, allowing probing of the surface area specifically[126–128]. This is particularly beneficial for polycrystalline thin films, which are

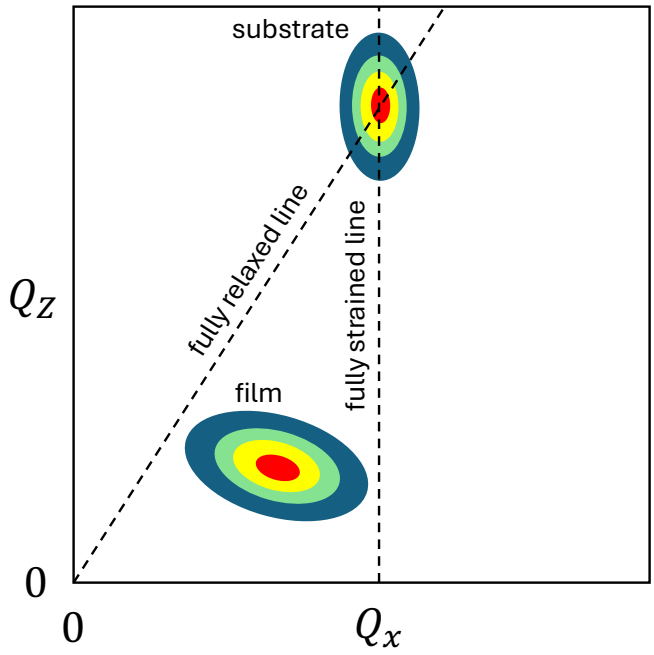


Figure 2.3: An RSM schematic in reciprocal space coordinates, demonstrating a film that is in a partially relaxed strain state compared to the substrate. The fully strained and fully relaxed lines are also shown.

typically very hard to obtain a diffraction from, due to the relatively low number of grains that are in the correct configuration to satisfy Bragg conditions in a $\theta - 2\theta$ setup. By reducing the contribution from the substrate, it may be possible to observe these low-intensity peaks.

Additionally, provided that there are a sufficient number of grains in the film, it is likely that the Bragg condition will be satisfied even with the asymmetric scan (as the crystal planes are not parallel to the surface of the polycrystalline sample), and so it is possible to obtain a Bragg-Brentano-like diffraction pattern (reflections present for all planes of sufficient intensity) for these materials using GIXRD.

2.2 Electron Microscopy

Electron microscopy is a very useful technique, which can examine the microstructure and atomic composition of both bulk and thin film samples. Electron microscopes function much like optical microscopes, however, instead of visible light, a beam of electrons is focused on the sample using magnetic lenses. An image can then be produced using backscattered electrons, transmitted electrons, secondary, emitted electrons, or even X-rays, depending on the technique.

2.2.1 Scanning Electron Microscopy

One type of electron microscopy is scanning electron microscopy (SEM). This microscopy focuses on the surface of a sample, with the electron interaction volume typically being less than a few microns (depending on type of electron collected), meaning that all of the data collected comes from this region of the sample. Magnifications of $10\times$ to $500000\times$ can typically be achieved in SEM tools, providing a resolution of 1-2 nanometers.

In this technique, the data is primarily collected from secondary electrons, electrons that are ejected from the sample, due to their low kinetic these electrons come from primarily from the first few nanometers of the sample[129]. These are collected by a Everhardt-Thornley detector (ETD), which accelerates the electrons using an electric field. Image contrast is produced by topographical information only when using secondary electrons. Backscattered electron images can be used to provide contrast between different composition regions[130, 131]. These techniques are useful for examining the decomposition of microstructure or composition segregation.

Sample preparation for other techniques can also be performed in SEM, such as using a focused ion beam to prepare thin cross-sections of samples for transmission electron microscopy (TEM). A typical SEM microscopy setup is shown in **Figure 2.4**.

2.2.2 Transmission Electron Microscopy

In TEM, rather than collecting emitted or scattered electrons, the electrons must transmit through the sample, requiring the preparation of very thin cross-sections. A more advanced technique scanning transmission electron microscopy (STEM) is typically used for thin film samples and is able to achieve magnifications of $10^7\times$ [132] and atomic resolutions. While there are a number of different imaging modes, the most commonly used is high-angle annular dark field (HAADF) imaging. In this mode, contrast is sensitive to only atomic number, Z, however lighter elements will typically not appear as contrast scales with Z^2, allowing for very high resolution imaging of crystal structure. This means in oxide materials, typically only the metal cations are visible. Due to the high-angle of the collected electrons, this mode provides relatively little diffraction or phase contrast[133], however these can be obtained through a bright-field image or through the use of nanobeam diffraction. A typical TEM microscopy setup is shown in **Figure 2.4**.

2.2.3 Energy Dispersive Spectroscopy

Both SEM and TEM are capable of a secondary technique, energy-dispersive spectroscopy (EDS), which is capable of estimating atomic composition. In this technique, the electron beam from

the microscope is used to excite electrons in the sample, which emit characteristic X-rays upon de-excitation. The intensity of these characteristic X-rays can be used to quantify relative atomic composition. This can be used to map segregation of cations following extreme conditions such as an anneal.

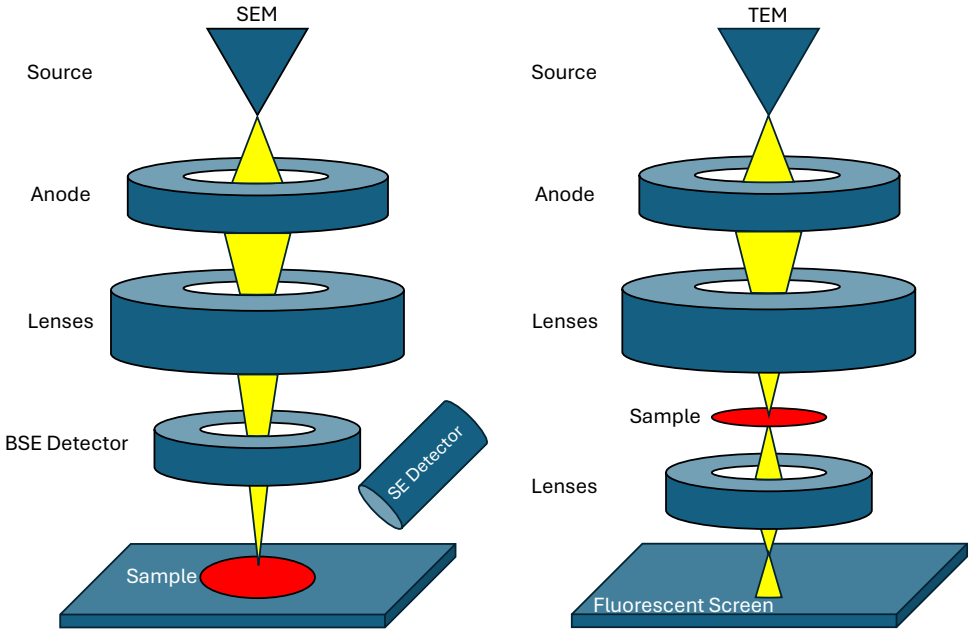


Figure 2.4: A schematic showing the difference between the SEM column, where the beam is focused on to a sample, with additional detectors to collect backscattered and secondary electrons and a TEM column, where the beam is directed through a sample and collected by a detector afterwards.

2.3 Thin Film Deposition Techniques

There are a wide range of techniques capable of depositing a thin film or coating of one material on to another, the substrate. These can broadly be defined as physical vapor deposition (PVD) or chemical vapor deposition (CVD). PVD techniques utilize a physical process to deposit thin films. The material is vaporized from the solid source and allowed to condense onto a substrate to form a coating[134]. CVD techniques produce films by a chemical reaction. Usually, gaseous source material is allowed to react near the substrate to form a coating on the substrate[135].

2.3.1 Pulsed Laser Deposition

pulsed laser deposition (PLD) is an example of a PVD technique. In PLD, a high power excimer laser (typically KrF 248 nm wavelength) is used to ablate a powder target inside a vacuum cham-

ber. The ablated powder absorbs the incident photons, resulting in a plasma plume of species ejected from the target and directed towards an appropriate substrate, held on a heater opposite the target[136]. These high energy species impinge upon the substrate and re-organize as adatoms to form a continuous film (in an ideal scenario). These films are typically highly epitaxial. The gas pressure present in the vacuum chamber can be controlled to not only assist in the formation of fully oxidized films, but also to control the energy of the plasma, due to scattering by the gaseous species. A schematic chamber is shown in **Figure 2.5(a)**.

As described earlier, under ideal conditions, a continuous film will form through layer-by-layer growth (Frank van der Merwe), however in non-ideal conditions, it is possible for films to form under different growth modes such as island growth (Wolmer-Weber) or layer plus island growth (Stranski-Krastanov)[137]. The structure of films grown through each of these methods are shown in **Figure 2.5(b)**. The following parameters can be tuned to influence the film growth mode:

- Gas pressure
- Gas species
- Substrate temperature
- Laser fluence (energy and spot size)
- Laser frequency
- Target material
- Target-substrate distance

One primary advantage of PLD is the stoichiometric transfer of the powder target composition to the condensed film, although in multicomponent targets, high laser fluence can lead to preferential self-sputtering of light atoms[138]. It has also been suggested that the large kinetic energies and high quench rates (from the plume to the substrate) can facilitate the synthesis of metastable thin films[139, 140].

2.3.2 Atomic Layer Deposition

A modification of CVD, known as atomic layer deposition (ALD) is still based on chemical reactions but rather than allowing the gases to react in-situ above the substrate, in ALD, the gases are carefully controlled using pump/purge processes, so that the reaction only occurs between at molecules adsorbed by the substrate surface[141–143]. This is done in cycles, with one precursor gas being introduced, allowed to adsorb to the substrate surface, and then being purged to remove

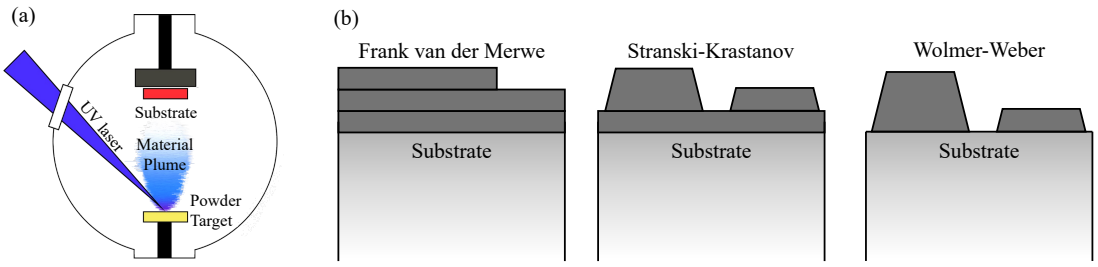


Figure 2.5: (a) A schematic detailing the components of a PLD chamber. (b) Schematic structure of films grown under each growth mode described in the text.

any excess gas. The second precursor would then be introduced and allowed to react with the first, before also being purged to remove any excess[144, 145].

Unlike PLD, ALD typically produces amorphous or polycrystalline films rather than highly epitaxial films. However, it has the advantages of operating at low temperatures, due to highly reactive precursors, excellent thickness controller (self-limiting less than monolayer growth[146]) and excellent step coverage, as the gas precursors attach to the surface, rather than line-of-sight deposition in the case of PVD techniques[147]. Additionally, amorphous films can often be re-crystallized using annealing techniques, such as rapid thermal annealing[148]. Like PLD, there are a number of parameters that can be optimized for better film deposition:

- Precursor choice
- Precursor pressure
- Precursor temperature
- Substrate temperature
- Precursor dose (exposure time)
- Purge length

There are also variants of ALD such as plasma-enhanced ALD, which utilize plasmas based on various gaseous species, such as O_2, N_2 and H_2, to create radicals which can react with the sample surface. It has benefits such as deposition at lower temperatures than conventional ALD, as well as improved film properties[149].

CHAPTER 3

Investigating Materials Predicted to Withstand Extreme Temperature

The results presented in this chapter are largely adapted from my own work in 'M. Webb, et al. High temperature stability of entropy-stabilized oxide $(MgCoNiCuZn)_{0.2}O$ in air. *Appl. Phys. Lett.* (2024)'[150].

3.1 Background: high entropy materials

The field of high entropy materials started in 1985 with the proposal of 5 component alloys, referred to as high entropy alloys (HEAs)[151]. HEAs have been defined as compositions comprised of 5 or more constituent metals, each of 5-35 at% (or a configurational entropy above about $1.5k_B$). These materials garnered interest when it was observed that many of these multi-component alloys could be synthesized in a single phase. This was unexpected as the maximum number of phases allowed increases with the number of components according to Gibbs' phase rule[152].

In these materials, there is a configurational entropy as expressed below in **eq. 3.1**, where k_B is the Boltzmann constant, x_i is the atomic fraction of element i on the disordered site, and N is the total number of disordered elements.

$$S_{conf} = -k_B \sum_{i}^{N} x_i ln x_i \tag{3.1}$$

For an equimolar composition with N elements on a disordered site, this can be simplified to **eq. 3.2**. This relationship between number of elements and configurational entropy is calculated and displayed in **figure 3.1**. There is an obvious diminishing return in configurational entropy with increasing number of elements.

$$S_{conf} = -k_B ln N \tag{3.2}$$

This configurational entropy can overcome the unfavorable enthalpy associated with adding more elements to a compound, resulting in a negative Gibbs' free energy, hence stabilizing the single-phase material. Even at room temperature, entropy overwhelms enthalpy in controlling phase stability of these multi-component system[153].

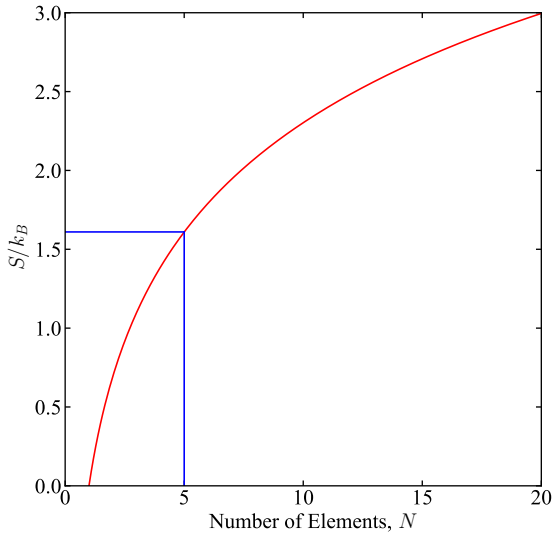


Figure 3.1: Calculated (**eq. 3.2**) using configurational entropy for an equimolar compound with N elements on the disordered site, the value for an equimolar compound with 5 disordered elements is highlighted, being the most common type of high entropy compound.

There is interest in these high entropy and entropy-stabilized materials due to the immense number of compositions that can be realized through this new method to achieve single phase materials and a number of effects hypothesized in these high entropy materials[154, 155]. These effects include sluggish diffusion, severe lattice distortion, 'cocktail' effects, and enhanced solubility of elements into unusual crystal structures.

In particular, there is significant interest in the high temperature applications of HEAs, which are thought to be particularly suited for this work, as the domination of the entropy term limits phase segregation and formation of defects at extreme temperatures[156, 157]. This can be understood through the Gibbs' free energy[158], shown below in **eq. 3.3**, where $\Delta G(T)$ is the change in Gibbs' free energy as a function of temperature, ΔH is the enthalpy of formation, T is the absolute temperature and ΔS is the entropy of formation. A negative Gibbs' free energy indicates phase stability at a given temperature, therefore a large positive entropy term is expected to improve stability with temperature.

$$\Delta G(T) = \Delta H - T\Delta S \tag{3.3}$$

While these HEAs do suppress the formation of intermetallic compounds, they are often prone to oxidation at elevated temperatures[159].

Recently, the concept of high entropy materials has been extended to multi-cationic oxide alloys (high entropy oxides (HEOs) and entropy-stabilized oxides (ESOs)) with the synthesis of $Mg_{0.2}Co_{0.2}Ni_{0.2}Cu_{0.2}Zn_{0.2}O$ ((MgCoNiCuZn)O) by Rost et al. in 2015[160]. Being oxides, these materials have a lower risk of experiencing failure due to oxidation at these same elevated temperatures; hence, it is believed that HEOs also have a lot of potential as refractory materials[161]. In the case of ESOs, the entropy stabilizing effect can be used to incorporate high fractions of oxides in metastable structures. In the prototypical entropy stabilized oxide, (MgCoNiCuZn)O, both CuO and ZnO have been incorporated in to a rocksalt structure oxide, despite tenorite and wurtzite being the respective stable structures. The limited solubilities and structural mismatches of tenorite CuO and wurtzite ZnO are overcome by entropy. This is confirmed by observing that the transition is endothermic and reversible, and removing any component oxide results in a multiphase system[162]. Hence this is an entropy stabilized oxide, as well as a high entropy oxide.

Compared to HEAs, there is a lesser effect of entropy stabilization per unit volume in HEOs. While the chemically ordered oxygen sub-lattice is important for the formation of ESOs and HEOs, the presence of the ordered oxygen ions within the unit cell typically results in a larger unit cell for oxide crystals. In these materials, the entropy promotion is mediated by the anion sub-lattice by:

- producing a similar nearest-neighbor environment for all cations
- accommodating deformation due to differences in cation sizes and bonding[162]

Variations in the cation-anion bond length and Jahn-Teller distortions with Cu have been observed in (MgCoNiCuZn)O, experimentally illustrating how cation disorder is accommodated by the oxygen sub-lattice[163].

When considering entropy per unit volume, the important parameter to consider is the number of disordered sites per unit volume. This is more variable in oxide materials, which have a larger unit cell and a greater range of crystal structures than metals and is exacerbated by the ordered oxygen sub-lattice, which tend to be either close-packed (face-centered cubic (FCC), hexagonal close-packed (HCP)) or body-centered cubic (BCC) structures. This effect is illustrated in **figure 3.2**.

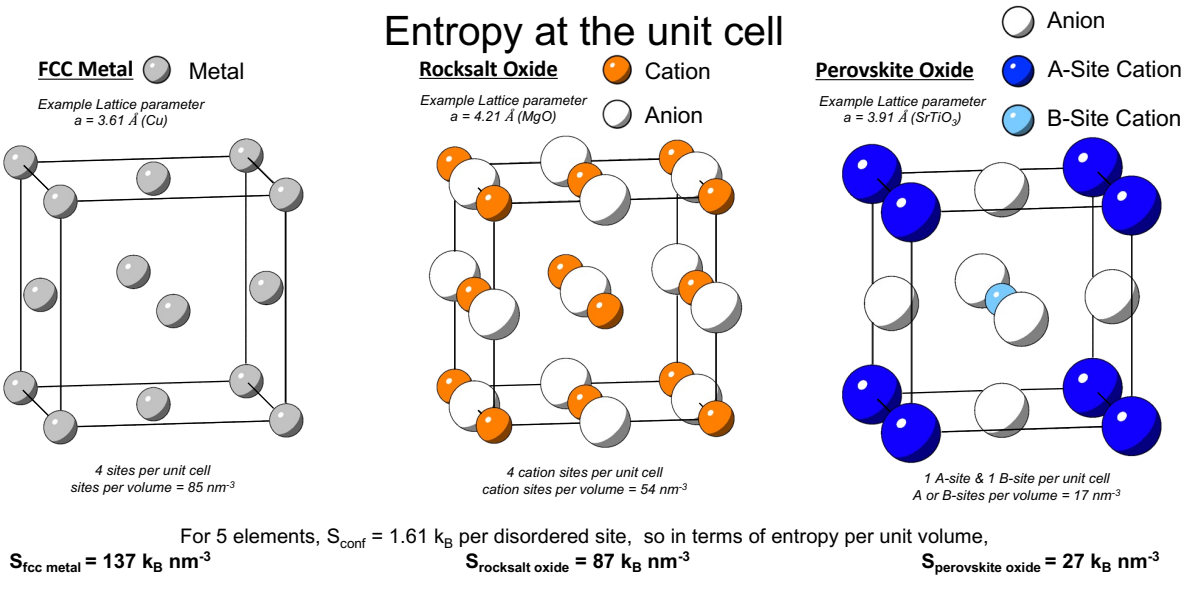


Figure 3.2: Schematics showing the unit cell for: an FCC metal, a rocksalt oxide, and a perovskite oxide. Included are the calculated entropy values using **eq. 3.2**. This is then converted to an entropy per unit value to illustrate the lower magnitude of configurational entropy for HEOs compared to HEAs due primarily to the presence of the oxygen sub-lattice.

Like HEAs, the high temperature prospects of these HEOs are very promising due to the wide array of compositions and properties that can be investigated when using 5 or more constituent oxide components, potentially from several crystal structures[164–166]. Additionally, the risk of oxidation is reduced in these materials, as they are already oxides (although not impossible). Typically, these HEOs (and ESOs) are metastable at ambient temperature and only stable at high temperatures, (MgCoNiCuZn)O, for example, is quenched from 1000 ºC to obtain a single-phase material. However, due to the relative youth of the field, the high temperature stability of HEOs has only been investigated rigorously in a few cases[140, 167] and typically not above 1000 ºC.

As a new and emerging field, there is much that is unknown about HEOs. Generally, it is unknown how the local structure and interaction between disordered cations will cause the macroscopic physical properties to deviate from a rule of mixtures. To be able to predict properties such as thermal stability, magnetic ordering, and electronic behavior, it is important to be able to understand HEOs on a fundamental level.

In this chapter, we discuss and investigate the hypothesized high temperature stability of HEOs, using thermal annealing, XRD and SEM to characterize any changes in phase or composition. Details of these techniques were discussed in **Section 2.1** and **Section 2.2.1** This will be done using the prototypical example of HEOs/ESOs, (MgCoNiCuZn)O, as this material is expected to

be stable up to extreme temperatures. (MgCoNiCuZn)O is also an interesting material because of its unique wealth of functional properties. It is antiferromagnetic[168, 169], has memristive properties[170], tunable optical properties[171, 172], energy storage capabilities[166, 173], and can incorporate other metal oxides to tune certain properties[174–178]. It is believed that many of these unique capabilities could be extended to other high entropy compositions.

(MgCoNiCuZn)O is synthesized from the binary rocksalt oxides, MgO, CoO, NiO and the binary non-rocksalts, ZnO (wurtzite) and CuO (tenorite)[160], where the Zn^{2+} and Cu^{2+} cations are stabilized into octahedral coordination by the entropy of mixing. This is not without consequences for the crystal, as it has been shown that the local and global structure of (MgCoNiCuZn)O is distorted from an ideal rocksalt, due in part to the Jahn-Teller distortion of the Cu^{2+} ions[163, 168]. The structural evolution of (MgCoNiCuZn)O due to this local distortion has been investigated at annealing temperatures up to 800 ºC[179]. Despite the significant property changes stemming from these distortions, however, no thorough investigation has been done into the stability of (MgCoNiCuZn)O at higher temperatures.

3.2 Solubility of copper and zinc in (MgCoNiCuZn)O

Before we discuss the fabrication and characterization of (MgCoNiCuZn)O, it is important to consider what contributes to the potential stability of the material. The entropy-stabilization hypothesis has been challenged by suggesting that general solubility of the species dictates the formation of (MgCoNiCuZn)OcitefracchiaConfigurationalEntropyMain2022. Under this hypothesis, the loss of Cu from the compound would be due to the solubility limit decreasing with increasing temperature; they did not consider Zinc in depth in this work.

To understand the phase stability and the failure modes of (MgCoNiCuZn)O, it will be important to understand whether the formation is dominated by entropy, as suggested by Rost et al.[160] or whether it is simply a result of solubility as suggested by Fracchia et al.[180]. It is important to note that while Rost was not able to obtain a single phase four-component equimolar oxide material, hypothesized to be because of the lower entropy, this would be 25% of each element. Conversely, Fracchia was able to obtain single phase two- and four- component oxides by including only 20% of Cu and/or Zn, suggested to be roughly the limit of solubility. Recently, it has also been shown that percentages of ZnO and CuO larger than 20% can be incorporated into the high entropy system[181].

To investigate this theory further, we compiled reports of the solubility of CuO and ZnO in the literature to create **Figure 3.3**. This was done by taking the composition of the solidus between the rocksalt phase and the mixed liquid phase for each binary oxide system. However, while the reports

for CuO were relatively in depth, and as expected, the high (and increasing) solubility limit for ZnO in the rocksalt oxides was somewhat of a surprise. Aside from $Cu_xNi_{1-x}O$ which shows high solubility, the other CuO binaries exhibit much lower solubilities for CuO than observed, while all the ZnO binaries suggest far higher solubility. Due to the highly volatile nature of ZnO[182], it is important to note that the high temperature, in air, solubility of Zn in $Mg_xZn_{1-x}O$ has been reported[183].

Additionally, significant extrapolation was necessary for the ZnO-rocksalt systems as much of the data was not report beyond 1000 ºC. Beyond that, NiO-ZnO data is obtained from the NiO-ZnO axis of a ternary Fe_2O_3-NiO-ZnO phase diagram as no NiO-ZnO data could be found. This leaves us not knowing if the solubility for ZnO decreases beyond some temperature within this range, as is the case for many of the CuO-rocksalt binaries. As such, the phase diagrams were computed by our collaborators in 'M. Webb, et al. High temperature stability of entropy-stabilized oxide $(MgCoNiCuZn)_{0.2}O$ in air. *Appl. Phys. Lett.* (2024)'[150]. Details of the methodology can be found in **Appendix A**, along with the phase diagrams reported in **Figure A.1**.

This new computational data can be used to enhance **Figure 3.3** to give **Figure 3.4**, from which it is clear that while the computational and extrapolated data for the ZnO-rocksalt systems are not in complete agreement, the overall trend, that of a monotonic increase in solubility, is observed in both. By averaging these solubilities, it is possible to calculate an expected maximum cation % achievable for Cu and Zn in the high entropy system. Based on an initial 20% of each cation, we can predict that we would not expect any loss of Zn in this temperature range, but we would expect Cu to drop below 5%.

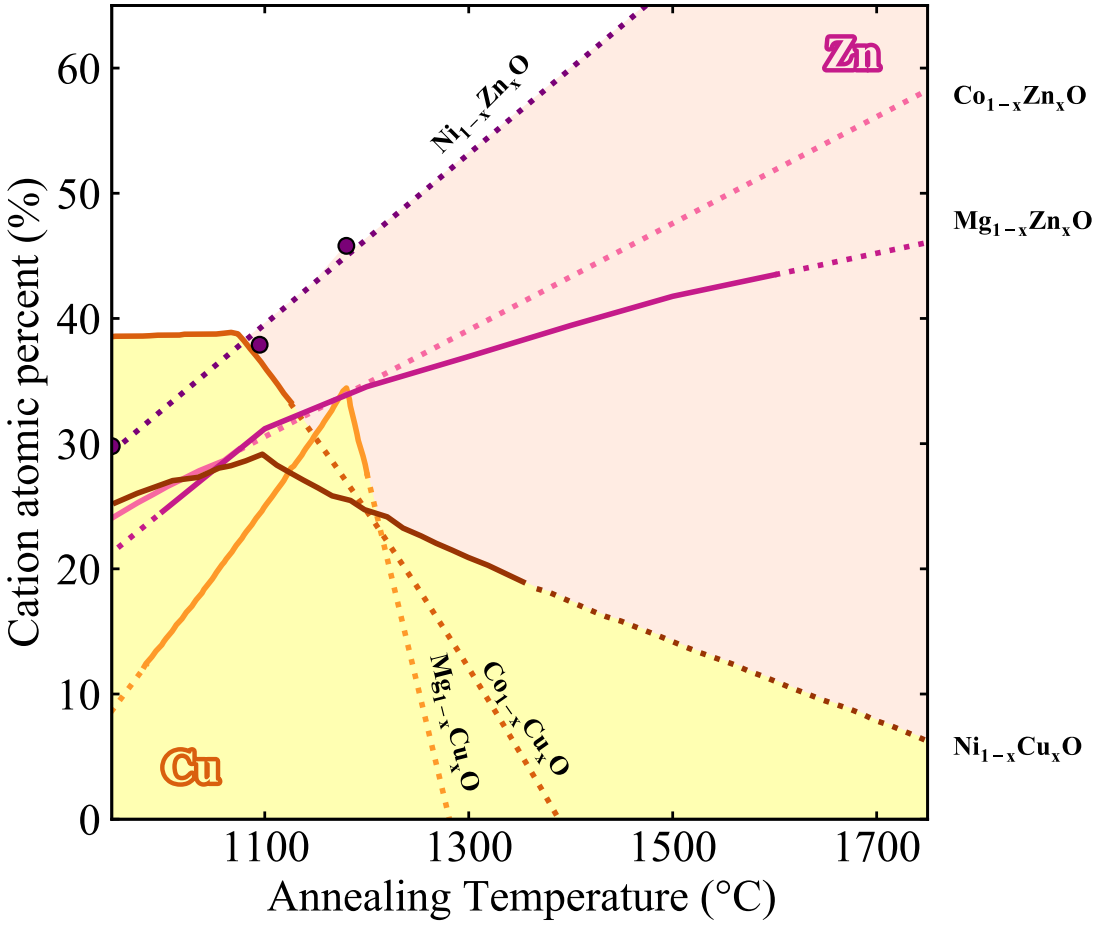


Figure 3.3: Solubility of Cu and Zn in the rocksalt oxides, extracted from the binary phase diagram solidus. The data used to produce this figure is from [183–188]. Solid lines and points indicate experimental data, while dotted lines indicate a linear extrapolation from the measured data. The shaded area is the maximum range of miscibility predicted for the binary rocksalt-CuO and rocksalt-ZnO systems. It is observed that the copper solubility in the rocksalt oxides generally peaks around 1100-1200 ºC, before dropping rapidly. Conversely, within the temperature range considered here, the Zn solubility in the rocksalt oxides monotonically increases. Note that there is a region of $\geq$ 20% solubility for CuO and ZnO in all the rocksalt oxides from about 1050-1200 ºC. The NiO-ZnO data is shown as individual points as it is obtained from the NiO-ZnO axis of a ternary Fe_2O_3-NiO-ZnO phase diagram as no NiO-ZnO data could be found.

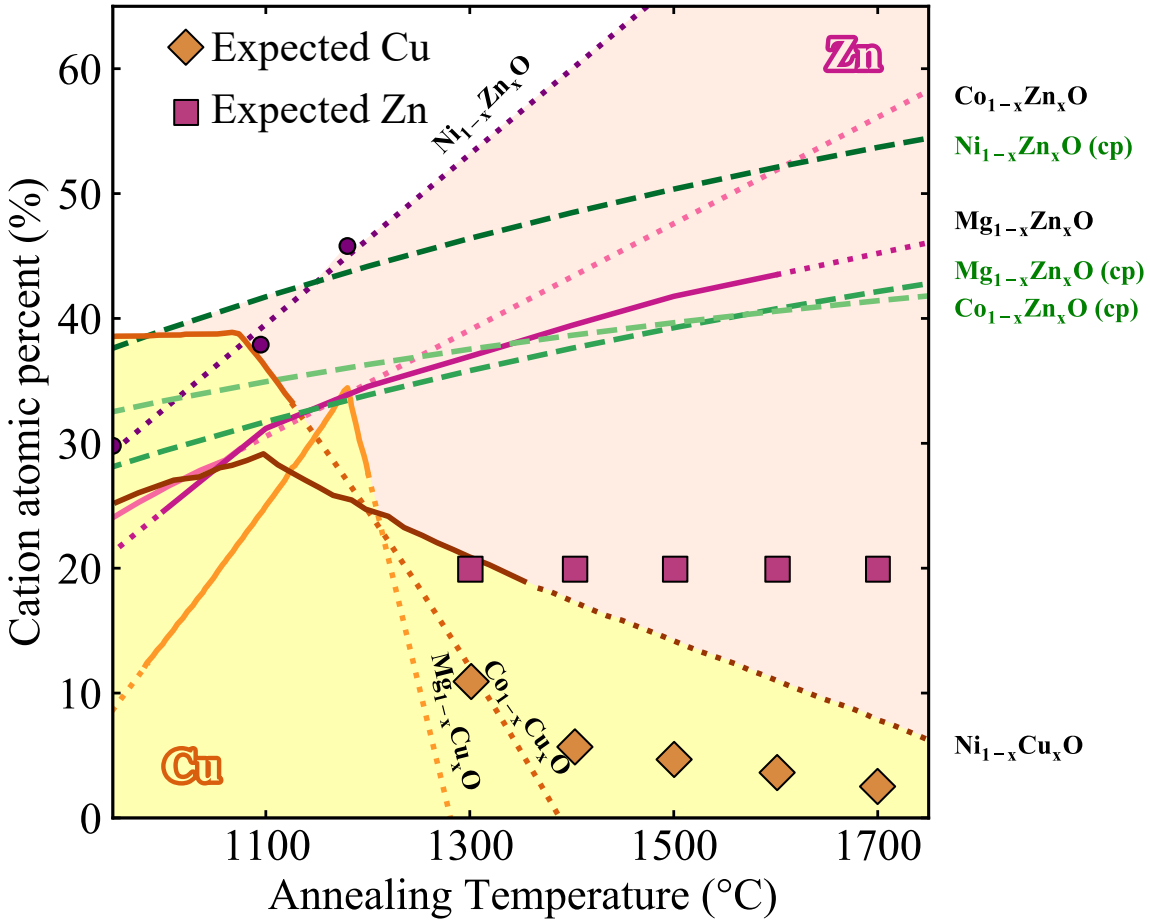


Figure 3.4: This figure is constructed using data from **Figure 3.3** and **Figure A.1**. The additional computational data is highlighted in green and denoted by (cp). By averaging the solubility of the binary rocksalt oxides, we can produce a simplified hypothesis on the solubility of Cu and Zn in (MgCoNiCuZn)O. This gives the expected Cu and Zn values shown, assuming an initial composition of 20% of each.

3.3 Fabrication of (MgCoNiCuZn)O

A single-phase, polycrystalline (MgCoNiCuZn)O pellet was prepared by mixing and grinding the constituent powders (MgO, CoO, NiO, CuO, and ZnO (Alfa Aesar, 99.99%)). The MgO, CoO, and NiO powders were all rocksalt structured, while CuO was tenorite and ZnO was wurtzite. This was followed with pressing at 70,000 psi and sintering at 1100 ºC for 18 hours before air quenching to room temperature[150]. The air quench is necessary as this phase is only stable at temperatures above 1000 ºC, by quenching, diffusion is limited and this metastable phase can be preserved down to room temperature. This procedure is performed twice to ensure homogeneity. The target weight of 10g was made up of $\sim$ 1.15g MgO, 2.14g CoO, 2.13g NiO, 2.30g CuO and 2.32g ZnO, calculated using the molar mass of each oxide. Homogeneity of the pellet and the nominally equimolar composition was confirmed using SEM EDS. The XRD scans with $2\theta - \omega$ configuration reveal diffraction peaks consistent with a rocksalt structure and a lattice parameter of 4.239 ± 0.001 Å (determined by Rietveld refinement using International Centre for Diffraction Data's Powder Diffraction File PDF-5[189] 00-073-0933) in agreement with prior reports of bulk (MgCoNiCuZn)O[160, 163, 169, 190]. This is illustrated in **figure 3.5**.

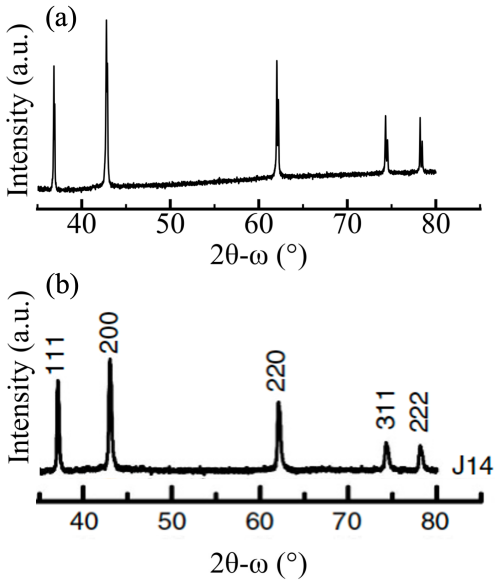


Figure 3.5: (a) X-ray diffraction data for an as-sintered pellet (1100 ºC for 18 hours) of polycrystalline (MgCoNiCuZn)O. (b) X-ray diffraction analysis of (MgCoNiCuZn)O produced in the seminal work by Rost et al. This sample was sintered at 1000 ºC for 12 hours twice. Data adapted from [160], note that J14 is another name for (MgCoNiCuZn)O. The same peaks are observed in both sets of data with a similar ratio of intensity between the differently indexed peaks, indicating that a single-phase rocksalt structured polycrystalline sample has been obtained.

3.4 Phase stability of high entropy oxide (MgCoNiCuZn)O under extreme conditions

After the composition and single-phase nature were confirmed, the pellet was fragmented into multiple samples, each to be annealed separately up to a chosen temperature and subsequent characterization, to elucidate the stability of the (MgCoNiCuZn)O material. Individual samples were annealed at 1300, 1400, 1500, 1600 and 1700 ºC. These temperatures were chosen because it is already known that (MgCoNiCuZn)O is stable up to at least 1100 ºC, as this is the temperature at which the phase was stabilized prior to quenching.

Initially these anneals were performed in a 1700 ºC capable Thermo Scientific Lindberg/BlueM 5000 W furnace suspended on yttria-stabilized zirconia (YSZ) media in a 50 x 40 x 20 mm^3 alumina crucible, with a heating rate of 20 ºC per minute. The cooling rate was nominally set to the same value, however as the furnace was only cooling passively, cooling slowed down as the temperature approached room temperature. However, this initial approach exposed two issues. Firstly, it was not possible to air quench the sample post-anneal from this furnace without damaging the heating element. Foregoing the quench leads to the presence of secondary phases in the pellet, as observed in the XRD in **Figure 3.6(a)**. As the single-phase rocksalt (MgCoNiCuZn)O is metastable below $\sim$ 900 ºC[160], it cannot be discerned if these secondary phases are formed because the material is not being stable above 1300 ºC or if it is simply because of its metastable nature at low temperatures. Secondly, when examining the pellets post-anneal, it was found that at the highest temperatures, the (MgCoNiCuZn)O had reacted selectively with zirconia from the media, resulting in deposits of zirconium along the grain boundaries; it is unclear what effect this may have had on the high temperature stability of (MgCoNiCuZn)O. This outcome is highlighted in **Figure 3.6(b)**, it is additionally noted that the reaction is evident on the remaining YSZ media (**Figure 3.6(c)**).

Because of this a new approach was used to conduct the anneals on the next set of samples (which were taken from the same original (MgCoNiCuZn)O pellet, with XRD as shown in **figure 3.5**). These anneals were conducted using a SentroTech ST-1700 ºC bottom loading furnace to facilitate post-anneal air-quenching. Rather than being suspended on YSZ media, these samples were instead suspended on a powder bed of (MgCoNiCuZn)O. This sacrificial powder bed layer will react with the surface of the alumina crucible, rather than allowing the (MgCoNiCuZn)O sample to react. This new configuration is illustrated in **Figure 3.7**, ultimately a cylindrical crucible with a lid was used. The samples were introduced into this furnace at the target temperature (1300, 1400, 1500, 1600, 1700 ºC), to limit the effects of heating rate, and then held at this temperature for two hours, and then air-quenched.

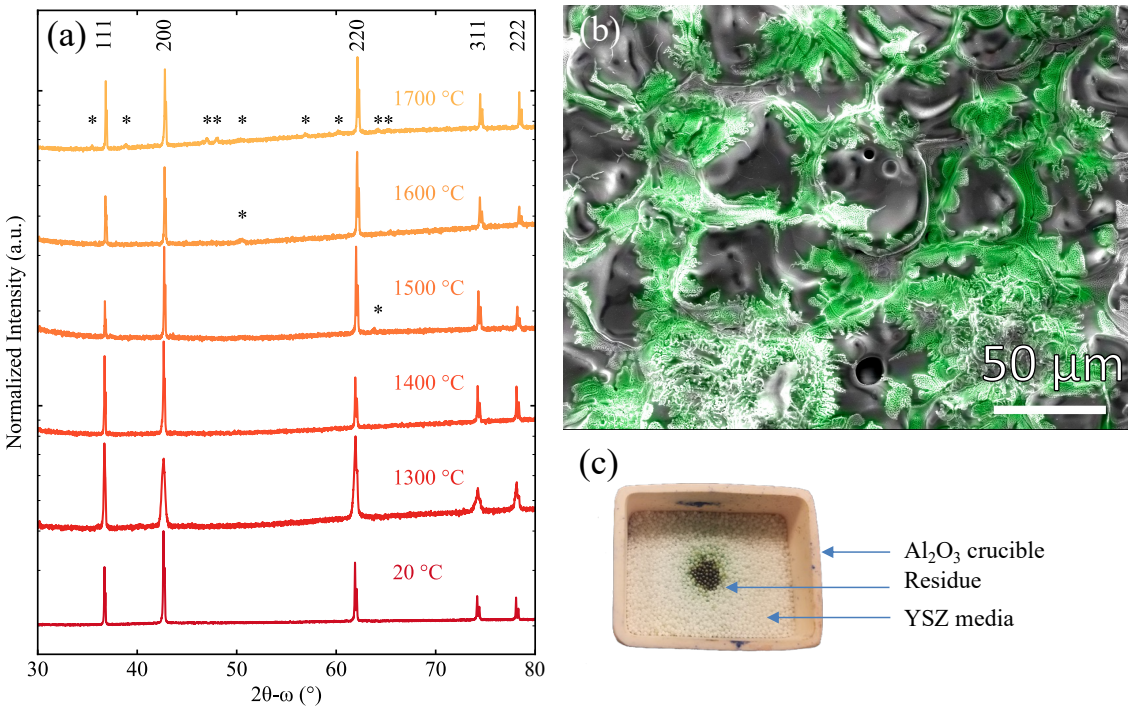


Figure 3.6: (a) X-ray diffraction analysis indicating the presence of wurtzite and tenorite secondary phases, consisting of CuO and ZnO that is metastable in the rocksalt structure. Without quenching from $\sim$ 900 ℃, these elements segregate from the rocksalt phase. An * marks a secondary phase identified as either wurtzite or tenorite. (b) SEM EDS analysis of a (MgCoNiCuZn)O sample following an anneal at 1700 ℃ for 2 hours. An ETD image is shown, overlaid with an EDS image (colored green) indicating the regions of high zirconium concentration, it is clear that the zirconium has predominantly deposited around the grain boundaries. (c) Photograph of the alumina crucible and YSZ media, post-anneal. The green discoloration is due to a reaction with the media, resulting in an oxide that has deposited on the YSZ media.

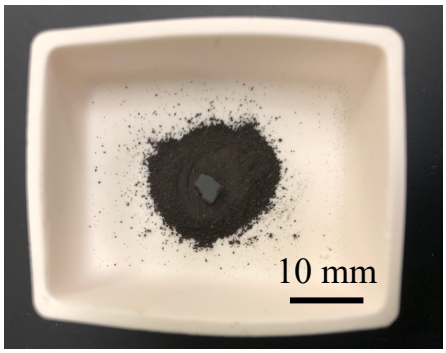


Figure 3.7: Image showing the configuration used for annealing in the SentroTech ST-1700. A (MgCoNiCuZn)O sintered pellet is protected from reaction with the crucible by using excess (MgCoNiCuZn)O powder that was confirmed to be single-phase (ground from a single-phase (MgCoNiCuZn)O pellet).

As inhomogeneity in the samples was a concern initially, due to a reaction with other elements present, this is the first measurement that was conducted in the revised samples. Following the anneal, SEM EDS was used to evaluate the compositional changes in the samples. The as-sintered (no anneal) sample was used as a control. The analysis reveals clear evidence of inhomogeneity following the anneal, however, it appears now to be intrinsic to the stability of the samples, rather than due to the methodology of the experiment. The composition of the elements expected within the (MgCoNiCuZn)O pellet are shown in **Figure 3.8**[150], no significant contamination was observed. The pristine (as-sintered) sample is observed to be homogeneous in all of the six elements present. However, following annealing this changes, the rocksalt ions (Mg, Co and Ni) and Zn appear to be segregated into the rocksalt grains, while Cu ions are segregated into the grain boundaries. Some slight segregation is also seen in the oxygen ions, with the concentration being lower at the grain boundaries (where Cu is present) than in the grains. As Zn is observed to be homogeneous, even in the limit of extremely low concentration at the highest temperatures, we hypothesize that Zn is sublimating from the rocksalt particles, going directly into a gaseous phase. Sublimation is known to occur in ZnO in the wurtzite structure[182].

Images in **Figure 3.9**[150] were produced using the Cu concentrations maps from **Figure 3.8** to color SEM ETD images of the same region (presented in grayscale).

From this analysis, it is clear that in samples annealed between 1300-1600 ºC, this matrix of high Cu concentration surrounds the grains. It is hypothesized that Cu ions act like mobile defects in the rocksalt structure, as it is unfavorable, as CuO is stable in the tenorite structure. As such, at high temperatures, these Cu ions cluster within the rocksalt particles, forming localized regions of tenorite CuO, possibly as a mechanism to reduce strain due to Jahn-Teller distortions. It has been shown in other Cu-containing materials that strain due to the Jahn-Teller effect can promote long-range interactions and even be suppressed through the application of a sufficiently large pressure, clearly indicating that strain is an important effect of the Jahn-Teller distortions[191, 192].

These tenorite CuO regions then melt to form a Cu-rich liquid phase, as the melting point of tenorite CuO is 1326 ºC[193], and the melting point of Cu_2O is even lower at 1235 ºC[194]. Lower still is the melting point of Cu metal, which is 1083 ºC[195]. It is important to take note of all the relevant phases of Cu and their respective melting temperatures, as we cannot discern for certain which phase the Cu ions are acting like in the high entropy structure, although CuO would be the expected phase. This Cu-rich liquid phase is more present along the grain boundaries, where there are many dislocations, as the lattice orientation changes from that of one grain to another[196]. Upon air-quenching the pellet (to retain the high entropy phase) post-anneal, the Cu-rich liquid phase is rapidly solidified along the grain boundaries.

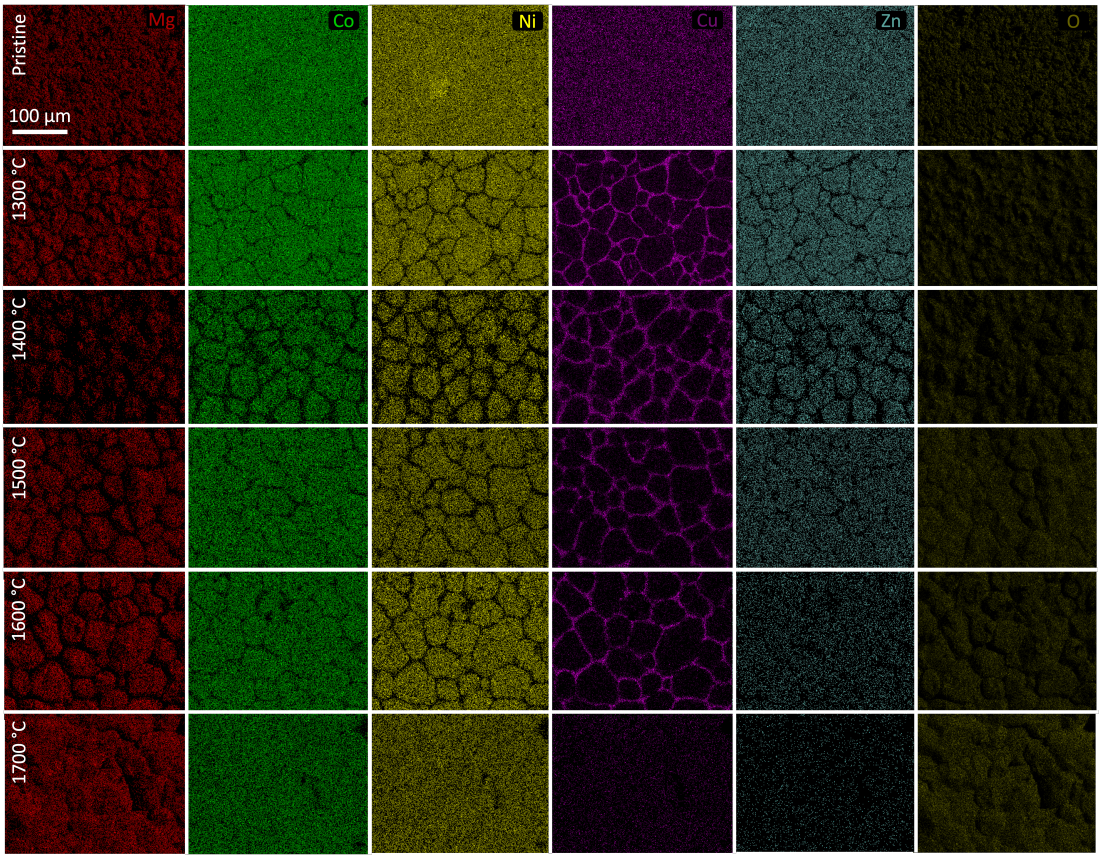


Figure 3.8: SEM EDS maps of annealed (MgCoNiCuZn)O. Atomic percent maps of Mg, Co, Ni, Cu, Zn and O, shown for pellets annealed at 1300-1700 ºC alongside the un-annealed sample. Quantification was done using the $K\alpha_1$ transitions. The rocksalt particles are homogeneous in Mg, Co, Ni and Zn, with a decreasing Zn concentration with increasing temperature due to sublimation.

At 1300 ºC, a significant amount of Cu remains in the rocksalt particles, and less copper appears to have been deposited along the grain boundary. This is because, at the highest temperatures, the lower viscosity of the Cu-rich liquid allows it to drain from the pellet prior to quenching, leaving the fused rocksalt grains that are observed at 1700 ºC in **Figure 3.9**. The Cu content along the grain boundary is estimated from both a compositional approach and an image analysis approach. These results are shown as a function of temperature in **Figure B.1**.

It has been shown computationally that the local strain around Cu^{2+} and Zn^{2+} ions reduces the formation energy of cation vacancies[197], and it has also been shown that the distortions around the Cu ions^{2+} increase with temperature [198]; we theorize that the higher vacancy concentration and distortion around these ions results in greater mobilities at these high temperatures, allowing clustering and net diffusion of these ions out of the rocksalt structure, through melting and sublimation respectively.

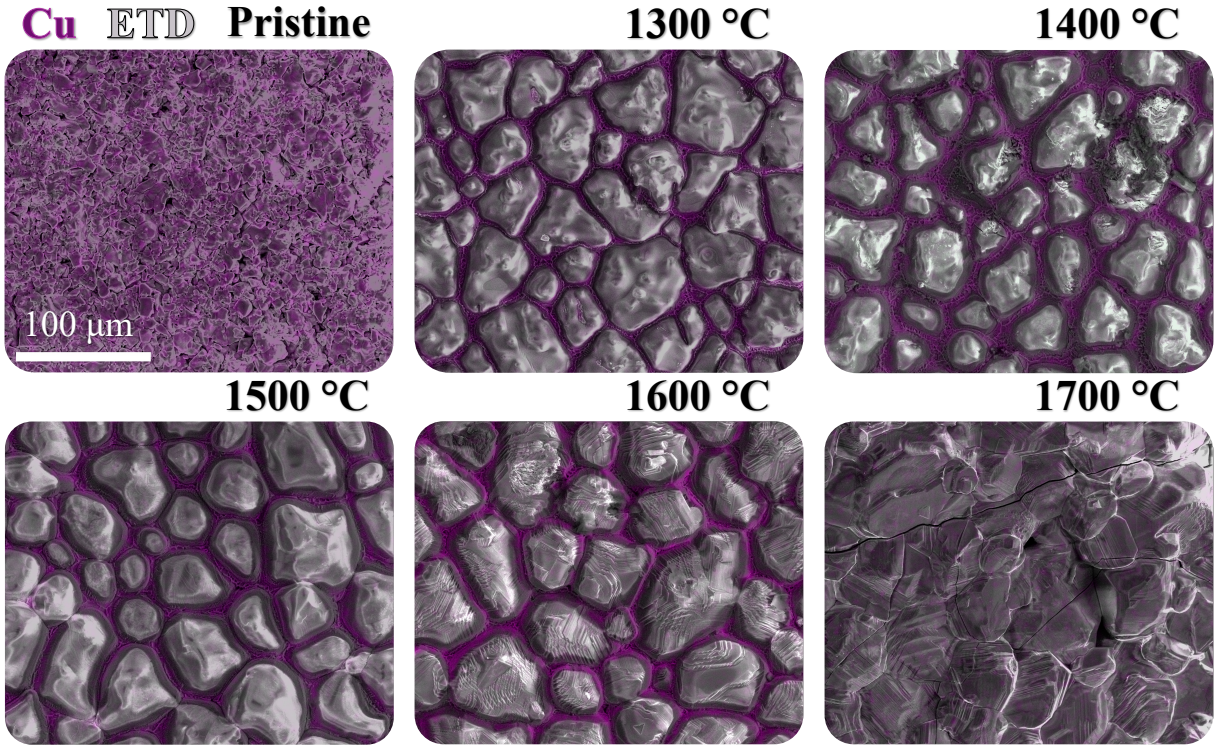


Figure 3.9: Composition and morphology of (MgCoNiCuZn)O sintered pellets following high temperature annealing. SEM EDS of pellet following annealing at up to 1700 ºC showing inhomogeneous distribution of Cu following annealing. Regions of high Cu concentration are observed between rocksalt particles after annealing. There is still a non-zero Cu concentration in the rocksalt particles, however it is not easy to see in the EDS maps due to the much larger segregated Cu concentration. Images were taken using an ETD and colored using the Cu concentration maps collected using EDS.

After anneals, the particle size increases significantly and the samples appear as smooth, round particles, with the boundaries between particles filled by a Cu-rich matrix. However, once the samples are annealed at 1600 ºC or higher, the particles begin to exhibit striated facets. The emerging faceting is consistent with an increased ionicity of the rocksalt particle as the unfavorable Zn and Cu concentrations are reduced. Upon annealing at 1700 ºC, large intragranular cracks form across the surface of the pellet, likely due to the extreme nature of the quench, resulting in significant thermal strains. Additionally, at this temperature, the particles have fused and there is no evidence of a Cu matrix.

Next, the samples were investigated using XRD, to investigate the phase stability of the rocksalt particles. $2\theta - \omega$ scans revealed diffraction patterns consistent with a rocksalt structure (**Figure 3.10**). Through the XRD, we observe no secondary peaks, neither tenorite nor wurtzite, following annealing at any temperature. This indicates both that the quench is successfully retaining the

rocksalt phase, and additionally that the Cu-rich matrix is amorphous. This reinforces the hypothesis that this phase was molten at these elevated temperatures, and as we see a diminished presence of oxygen within these region (**Figure 3.8**), suggests that the composition is likely close to Cu_2O, albeit fairly defective. Additionally, an unusual trend is observed in the peak intensity ratios of the annealed samples, that the $\frac{I_{200}}{I_{220}}$ ratio decreases from 1300 to 1500 ºC before increasing again when the annealing temperature is increased further. This is seen to inversely correlate with the Cu-rich fraction (shown in **Figure B.1**), and could be due to a changing magnitude of the Jahn-Teller effect, due to the loss of Cu ions, which are the most prone to a Jahn-Teller distortion[191].

To further assess the stability of the rocksalt material, the composition of each pellet was investigated following the annealing process, using SEM EDS. This enables an understanding of the chemistry of the emergent phases. This data is shown in **Figure 3.11(a)**, plotted versus annealing temperature. Analysis of samples annealed at temperatures above 1400 ºC show a significant deviation in composition from the expected equimolar compositions, shown as a dotted line. This deviation is a result of a loss of Zn and Cu from the rocksalt phase. As a result of this there is a drop in the configurational entropy, shown below the composition, along with the temperature entropy product. This entropy is calculated using **Eq. 3.2** and in the sample annealed at 1700 ºC, has dropped to approximately the configurational entropy of an equimolar three component oxide system. This can be understood through the compositional change, as nearly all of the Cu and Zn has been lost from the rocksalt oxide phase. The compositional changes correspond to an entropy change from $\sim$1.60 k_B to $\sim$1.16 k_B. For an ideal five-component system, S_{conf} is 1.61 k_B, in a four-component system it is 1.39 k_B, and in a three-component system it is 1.10 k_B The drop in the ideal configurational entropy of the pellet also leads to a decrease in $-T\Delta S$. This change in entropy to below that of a four-component oxide supports a hypothesis that Zn sublimes from the rocksalt phase due to the entropy no longer being sufficient to counteract an unfavorable enthalpy.

After annealing at 1500 ºC and higher, a strange trend is observed in the Mg concentration, as it is seen to increase. However, using cross-sectional EDS shown in **Figure B.2**, it is revealed that this increase in concentration is primarily a surface effect. It is hypothesized that this is a possible result of the strain induced by quenching the sample from extreme temperatures, however more study would be needed to fully support any particular theory. Using the compositions measured, the expected lattice parameter can be calculated using Vegard's law[199] shown below in **Eq. 3.4**, where $a(x)$ is the lattice parameter of the mixed oxide, N is the total number of different constituent oxides and x_i and a_i are the fraction and lattice parameter of the ith component oxide.

$$a(x) = \sum_{i}^{N} x_i a_i \tag{3.4}$$

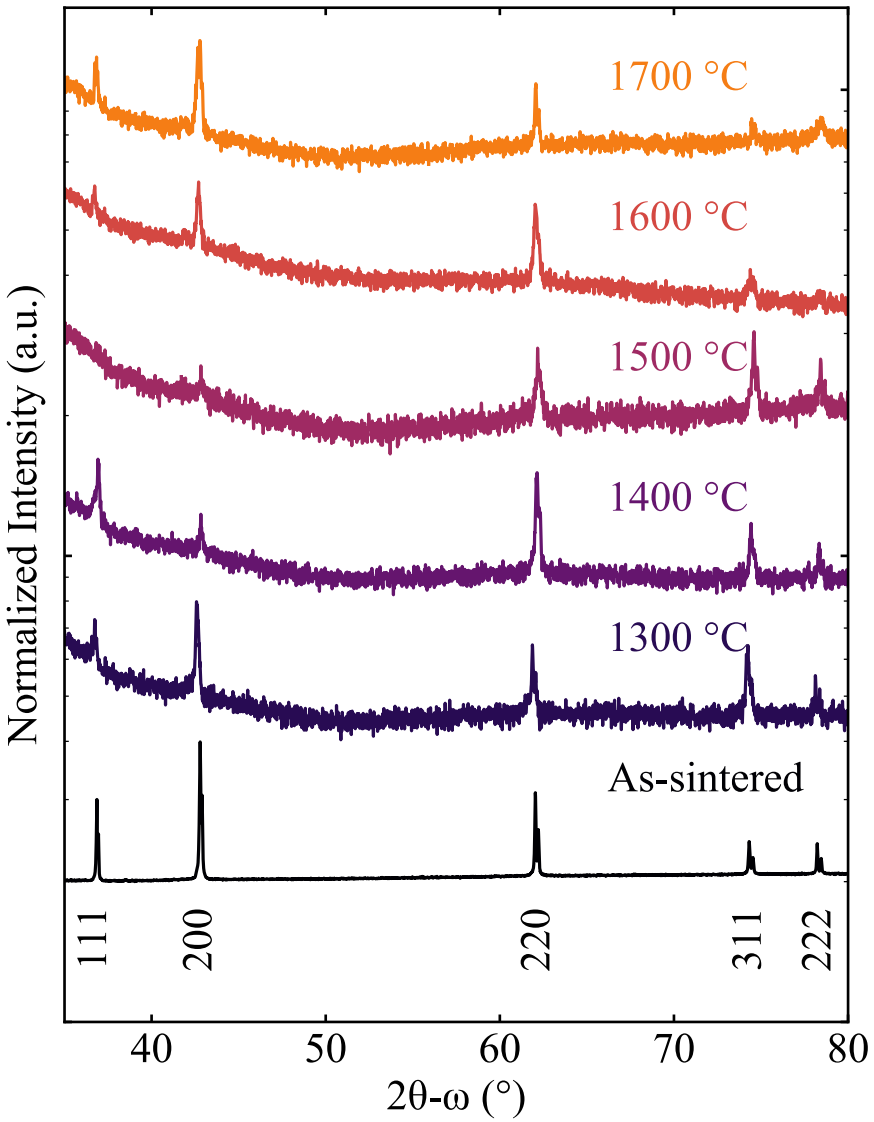


Figure 3.10: XRD patterns following annealing and air-quenching of (MgCoNiCuZn)O. XRD data for an as-sintered pellet (1100 °C for 18 hours) of polycrystalline (MgCoNiCuZn)O (as shown in **Figure 3.5**) and the same (MgCoNiCuZn)O pellet after annealing for 2 hours at the given temperature and subsequent air quench. The peak intensity ratios for the as-sintered sample are typical of a rocksalt structure. Following annealing, the peak intensity ratio of the XRD of the samples is varied, often with an increase intensity for the 220 peak. It is possible that this is due to local structure or distortions. It has also been suggested that it could be due to a change in the Jahn-Teller effect, due to the loss of Cu during the anneal[191]. No secondary phases (tenorite-CuO or wurtzite-ZnO) are observed. Datasets are offset vertically for clarity.

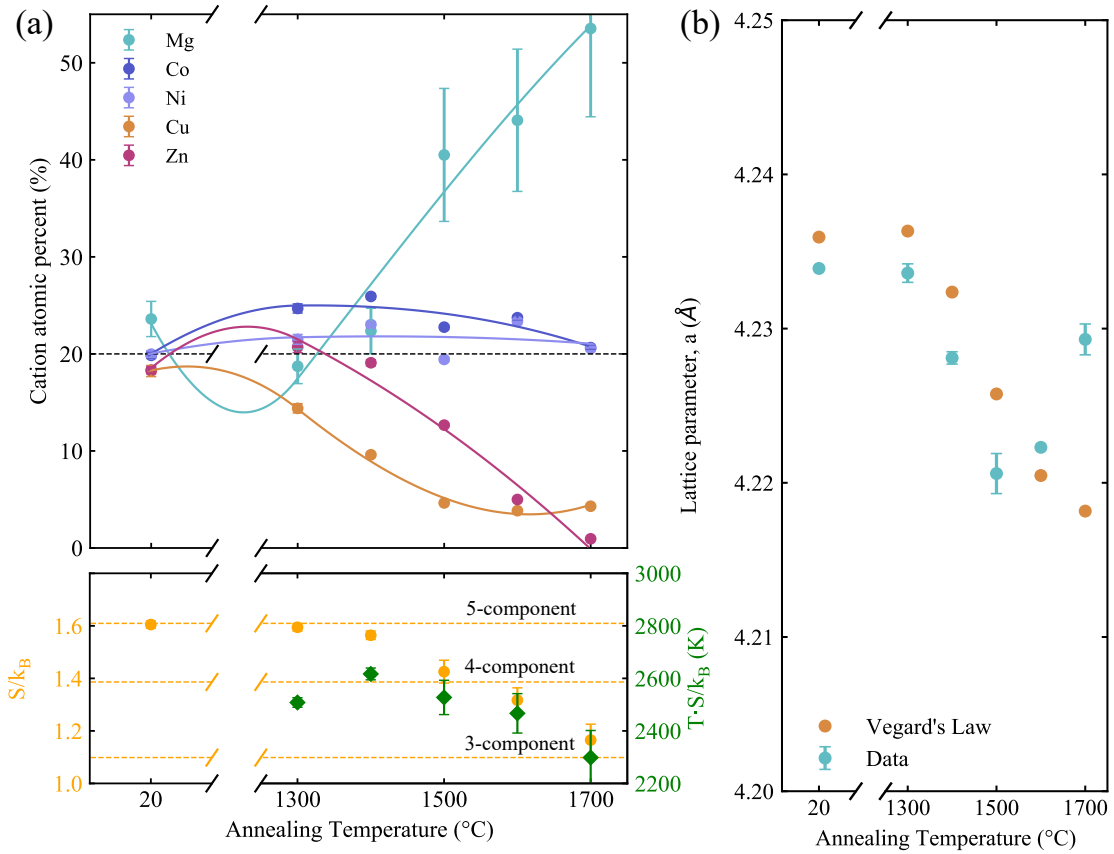


Figure 3.11: Selective loss of Cu and Zn at high temperature in (MgCoNiCuZn)O. (a) SEM EDS data showing the cation atomic percent of a rocksalt particle surface following a 2-hour dwell at the given temperature. The 20 °C sample is as-sintered and has not undergone an annealing treatment. Errors are the error in the fit according to the SEM software. Lines have been added to help guide the eye along the changes in each elemental composition and sum to 100%. Additionally, the calculated configurational entropy (S) of each composition, is shown in the bottom panel, along with the entropy-temperature (TS) product. The dotted lines represent the expected S/k_B values for ideal 5-, 4- and 3- component systems respectively, calculated using **Eq. 3.1**. We observe that significant losses in Cu and Zn occur, and correspondingly this results in a drop in entropy. (b) The experimental lattice parameters and errors as determined using Rietveld refinement for the $K\alpha_1$ peaks in **Figure 3.10**, along with the Vegard's law estimate using the compositions from (a). The Vegard's law[199] calculation was done using experimental values for MgO, CoO, and NiO, and using the octahedrally coordinated ionic radii[200] for Cu^{2+} and Zn^{2+}, to estimate the lattice parameter of rocksalt CuO and ZnO. While individual points have poor correlation, the overall trend between the change in Vegard's law and the measured lattice parameter is similar.

For oxides like CuO and ZnO, which do not exist in the rocksalt phase, the ionic radii as presented by Shannon[200] were used, alongside the experimental ionic radii for MgO, CoO, and NiO. These expected lattice parameters are shown in **Figure 3.11(b)** alongside the lattice parameter as calculated using Rietveld refinement on the XRD data shown in **Figure 3.10**. The generally good agreement between Vegard's law and the experimental lattice parameter indicates that the measured composition is being correctly identified as belonging to the rocksalt phase. The discrepancies may be attributable to the unusual Mg concentration observed at the surface, as this value is used in calculating the expected lattice parameter.

Based on the data presented here, it is hypothesized that the correlation between the Zn and Cu composition is an entropy driven effect. It is known that Cu has the least favorable enthalpy of formation for the rocksalt structure, and in addition, prior density functional theory (DFT) calculations have shown that the Cu cation in the rocksalt structure is associated with the most significant point defect densities[197]. Based on this, it could be expected that the Cu cations would be the first to segregate from the rocksalt structure, as observed here. Above $\sim$ 1300 ºC, segregated CuO would be expected to melt, regardless of phase, as detailed earlier in this section. This would result in a decrease in the total entropy of the rocksalt phase.

While it has been shown in 3.2, that the addition of ZnO to a rocksalt oxide, such as MgO, has high solubility limits, we theorize that this limit is reduced in the four-component rocksalt system, due to the reduced entropy gain when introducing a new species to an initially more numerous system. It follows that when the Cu and the configurational entropy it has introduced are lost from the structure, the solubility of Zn in the rocksalt phase is decreased, and the unfavorable enthalpy is no longer compensated, resulting in the loss of Zn from the rocksalt phase.

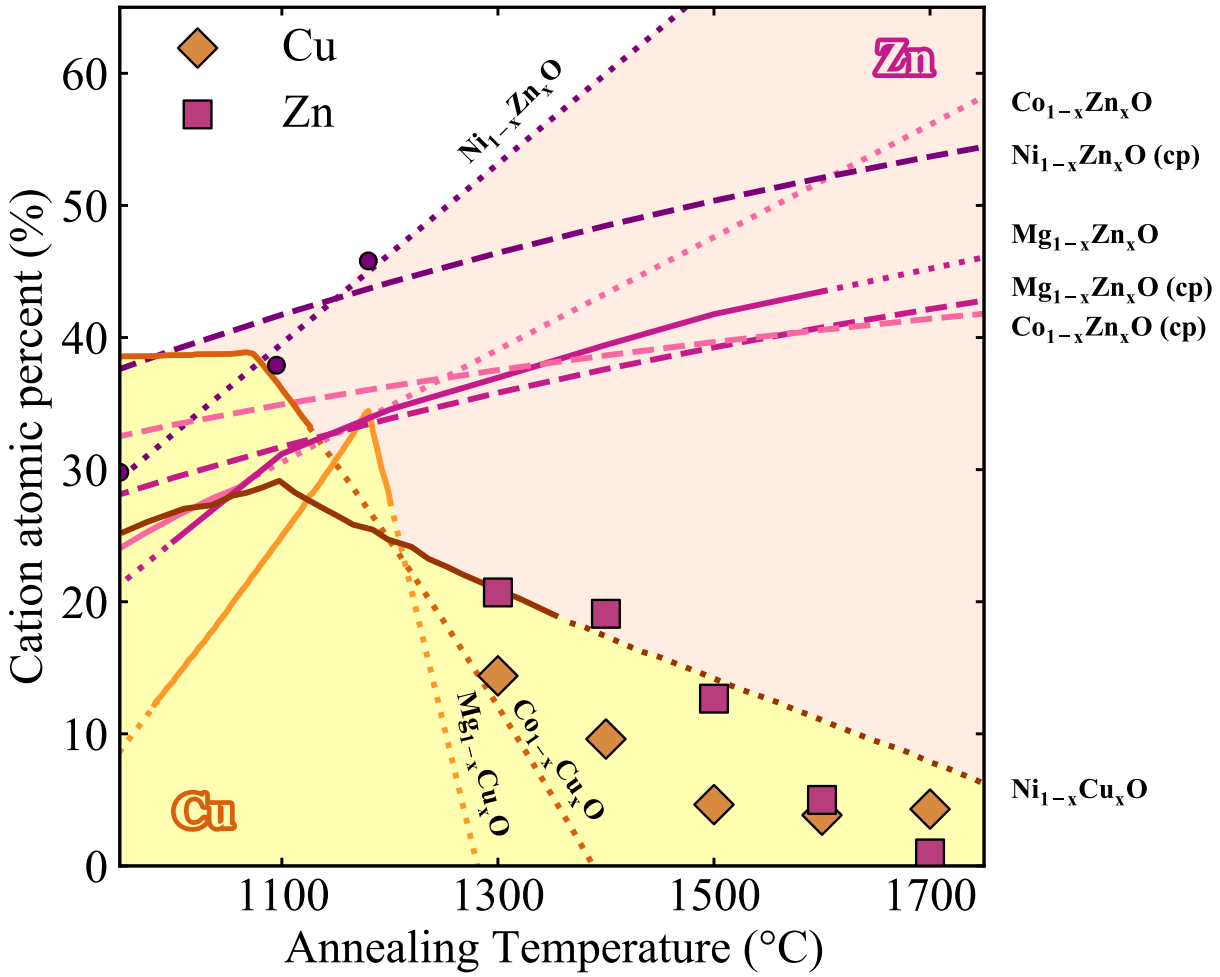


Figure 3.12: Comparison of observed Cu and Zn composition to maximum solubility at the solidus. The copper concentration in (MgCoNiCuZn)O is observed to correspond roughly with the solubility of Cu in the rocksalt-Cu oxide binary systems in the 1300 – 1700 ºC range. We note the observed Zn composition in (MgCoNiCuZn)O is much lower than the maximum solubilities in the associated binary oxide constituents and that the Cu and Zn concentrations are correlated. Produced by combining **Figure 3.4** and **Figure 3.11**.

3.5 Conclusion: the stability of bulk (MgCoNiCuZn)O

In this chapter, it has been demonstrated that (MgCoNiCuZn)O, the prototypical entropy-stabilized oxide, phase separates at high temperatures in air. This has been observed through a change in structure, composition, and particle morphology, following annealing treatments at temperatures up to 1700 ºC. The material loses a significant fraction of both Cu and Zn at temperatures above 1300 ºC in correlation. By 1700 ºC, this has resulted in the formation of a nearly pure rocksalt oxide material, with less than 5% Cu cation concentration and negligible Zn concentration. We anticipate that local cation vacancies around the Cu and Zn results in larger mobilities for these ions, allowing them to cluster and segregate from the (MgCoNiCuZn)O through selective melting and sublimation.

By considering the initial hypothesis, presented in **Figure 3.4** and the data collected in **Figure 3.11**, it is possible to produce a new figure, **Figure 3.12** demonstrating that while the Cu composition as a function of temperature is fairly close to the average of the rocksalt-binary oxides, the Zn composition is significantly lower than the maximum solubilities observed in the associated binary oxide constituents that make up (MgCoNiCuZn)O. Based on this, the correlative loss of Zn indicates that the formation of the (MgCoNiCuZn)O is not due to general solubility but rather due to the entropy-stabilized nature as demonstrated by Rost[160].

Unfortunately, the prototypical entropy-stabilized oxide did not achieve the expected high temperature solubility, decomposing at temperatures lower than many reported HEAs[201, 202].

However, it is still stable below approximately 1300 ºC, and with a large number of tunable functional properties[166, 168–178], so it would be inappropriate to consider it a material without potential for high temperature conditions after this study alone.

CHAPTER 4

Evaluating the Stability of Poly-Cationic Oxide Thin Films with Optical Properties

The results presented in this chapter are largely adapted from my own work in 'M. Webb, et al. Geometric defects induced by strain relaxation in thin film oxide superlattices. *J. Appl. Phys.* (2022)'[203] and an equal collaboration in 'S. McSherry[†], M. Webb[†], et al. Nanophotonic control of thermal emission under extreme temperatures in air. *Nat. Nanotechnol.* (2022)'[28].

4.1 Background: thermal stability and optical properties

Thin films with high thermal stability are of significant importance in many fields, including optical coatings[204, 205] and electronic sensors[206, 207]. But when considering thin films, there are often other extreme conditions to consider, aside from the applied temperature. Namely, the strain interaction between the substrate and the thin film can easily reach 1%, equivalent to a temperature of several thousand Kelvin (**Figure 1.1**).

In this chapter we will evaluate the stability of multiple poly-cationic oxide thin films, within a complex optical heterostructure, starting with thin films of (MgCoNiCuZn)O for the purpose of a coating capable of suppressing of a particular wavelength at elevated temperatures. These films are deposited using PLD, as detailed in **Section 2.3**.

The objective was to develop a multilayered photonic structure consisting of alternating oxide thin films that is air-stable at ultra-high temperatures and increases TPV efficiency. A TPV generator harvests heat from a local source and converts it to electricity using a suitable photovoltaic cell. These generators can have a high efficiency ceiling. Still, developments in management of the broad spectrum of thermal radiation can lead to significant gains in efficiency[46]. In fact, all thermal emitters can benefit from photonic materials that can suppress the amount of energy

[†]These authors contributed equally.

wasted by low-energy (undesirable) radiation, which cannot be converted into usable power by a photovoltaic cell.

A challenge for TPV generators has been the degradation of photonic materials under the extreme conditions to which they are subjected in thermal systems. Thus, new materials, with high stability with respect to extreme conditions (such as ultra-high temperatures, greater than 1000 ºC), and reactive, highly oxidizing environments are needed. Since TPV cells are more efficient at higher temperatures, it is important that the photonic materials can also withstand extreme environmental conditions[46, 208].

Control over thermal emission under these extreme conditions is desirable for a wide range of applications, including insulation for high temperature engines and waste-heat scavenging devices[209]. Existing bulk emitter approaches, including Yb_2O_3 foams[30], $Al_2O_3/Er_3Al_5O_{12}$ eutectics[29] and extrinsically doped materials such as MgO:NiO[210] can offer air-stable operation at temperatures as high as 1500 ºC but provide limited spectral control[28]. Nanophotonic approaches have tunable spectral and directional properties but are limited to lower temperatures and often inert environments, typically these methods are limited to below 1000 ºC, due to the nanostructured coatings used. Thin films are often observed to melt at significantly lower temperatures than their bulk counterparts[211]. There are additionally other complications, such as dewetting of thin films from the substrate[212]. Emission control is achieved by various structures, ranging from multilayers[48, 213–216] to metal/plasmonic arrays[33, 34, 49, 217–220] and 3D photonic crystals[32, 221, 222].

At extreme temperatures, these structures typically fail through one of several common failure modes that progress structures towards a more thermodynamically stable state, such as grain growth, interdiffusion[49, 221, 223, 224], and oxidation[216, 225–228]. A stability of over 1400 ºC has been demonstrated utilizing layers of W and HfO_2[48, 213], which is ultimately limited by grain growth of the oxide layer. Nonetheless, there is room for improving the stability of nanophotonic approaches under extreme and oxidizing conditions. Under these conditions, the highest operating temperature reported drops below 800 ºC in atmosphere[229].

One example of a nanophotonic structure is a structure of alternating materials with a difference in refractive index, this can result in reflection of undesirable radiation. This reflected radiation is then re-absorbed and re-emitted in a broadband spectrum, reducing the total percentage of radiation emitted as this undesirable wavelength.

Our initial approach consisted of alternating film layers of high and low refractive index of (MgCoNiCuZn)O that are lattice-matched and grown epitaxially on an MgO (001)-oriented substrate. This substrate is chosen based on a closely matched lattice parameter, its rocksalt structure,

and its use in prior literature[230]. Optical characterization experiments on the deposited structures, will demonstrate the effect of the photonic material upon emitting materials such as SiC or NiO-MgO[210].

While it has been shown in the previous chapter, that the prototypical high entropy oxide, (MgCoNiCuZn)O, is not as stable as theorized, it is still considered an exciting material, and stable until 1200 ºC. And while we have considered the properties of the bulk (powder pellet) material, the stability of other forms has not been investigated. If thin film (MgCoNiCuZn)O is stable until at least 900 ºC in air, this would be a new high operating temperature for a nanophotonic coating.

4.2 Optical properties and thermal stability of high entropy oxide thin films

Utilizing differences in lattice parameter and refractive index, achieved through different growth conditions during film deposition, it should be possible to produce a structure of two alternating (MgCoNiCuZn)O based structures.

The proposed structure and the deposition condition dependent refractive index has been reported previously[171], as shown in **Figure 4.1**, where a Δn of approximately 0.3 is achieved at large wavelengths, for structures deposited at 200 and 600 ºC respectively.

Initially, we demonstrate growth of five bilayers of deposited at 200 ºC and 400 ºC, as too large a difference in deposition temperature will effectively anneal the other layer.

The MgO substrate was baked for 20 minutes at 950 ºC, before cooling in 200 sccm of oxygen to 400 ºC. The target was then pre-ablated for 2000 pulses to clean the surface. Each layer was then deposited with a target-substrate distance of 7cm and a laser fluence and frequency of 1 J cm^{-2} and 5 Hz, with 500 pulses in 50 mTorr of oxygen, alternating between substrate temperatures of 200 and 400 ºC, with each layer being $\sim$ 5 nm thick.

Following deposition two distinct diffraction peaks, indicative of two different lattice parameters, one for each of the high and low refractive index films, were observed. However, following annealing at 400 ºC in air for 2 hours, only one broad peak was observed, indicating that the two distinct structures had intermixed into a single thicker layer of (MgCoNiCuZn)O, shown in **Figure 4.2**. This effectively shows that a multilayer of two (MgCoNiCuZn)O layers deposited at different temperatures, with different lattice parameters will not be stable at any significantly elevated temperature.

With the failure of this approach, the next approach was to produce a superlattice of

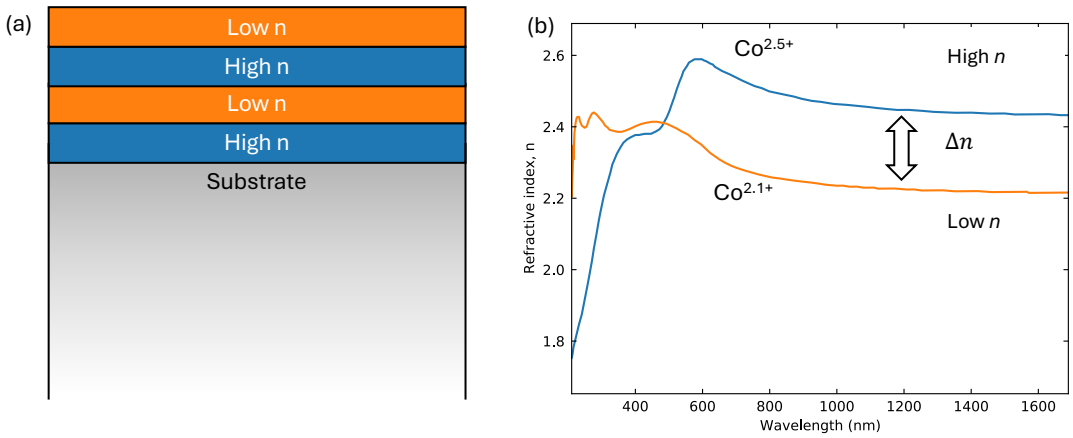


Figure 4.1: (a) Schematic photonic structure comprised of alternating layers of high and low refractive index (MgCoNiCuZn)O films, deposited at different substrate temperatures. (b) Refractive index variation with wavelength for (MgCoNiCuZn)O films grown at 200 ºC and 600 ºC. Adapted from [171].

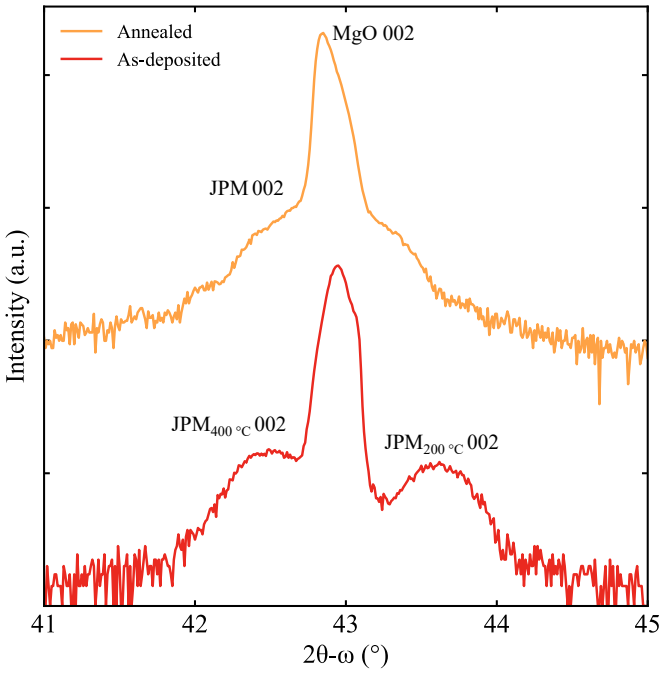


Figure 4.2: XRD data showing an as-deposited multilayer of (MgCoNiCuZn)O deposited at alternating temperatures of 200 and 400 ºC and XRD data following an anneal at 400 ºC for 2 hours, showing only one diffraction peak, indicative of intermixing of the two previously distinct structures.

(MgCoNiCuZn)O and MgO and test the stability of this. MgO was chosen due to its perfect lattice matching (as the substrate is also MgO) and known high melting temperature, over 3000 K[231]. However, first we decided to check the thermal stability of the (MgCoNiCuZn)O thin film by itself. For this a single layer of (MgCoNiCuZn)O deposited at 200 ºC was utilized. Upon annealing at 700 ºC for 2 hours in air, the film remained but the lattice parameter shifted from that of the 200 ºC deposited sample to the bulk lattice parameter, additionally a secondary phase peak was present. Following further annealing at 1100 ºC for 2 hours, no film peaks were present in the XRD. Additionally, the film was no longer visible on the substrate (prior to anneal the film had appeared as a brownish orange coating). These results are highlighted in **Figure 4.3**.

Further investigation using atomic force microscopy (AFM) and SEM reveals the potential failure mechanism of the film at 1100 ºC as dewetting, a failure mode common to thin film materials[212]. Following dewetting, particles are observed using both techniques, shown in **Figure 4.4**. AFM makes use of a small cantilever tip to detect deflections from these particles, while the details of SEM were discussed in **Section 2.2.1**.

So, it is clear that the (MgCoNiCuZn)O heterostructures are not stable above 400 ºC with respect to intermixing and even a single (MgCoNiCuZn)O film is not phase stable above 700 ºC, perhaps as a result of the bulk being metastable below about 900 ºC. It is therefore not possible to produce a highly stable heterostructure where one of the layers is a (MgCoNiCuZn)O film; A new approach is required.

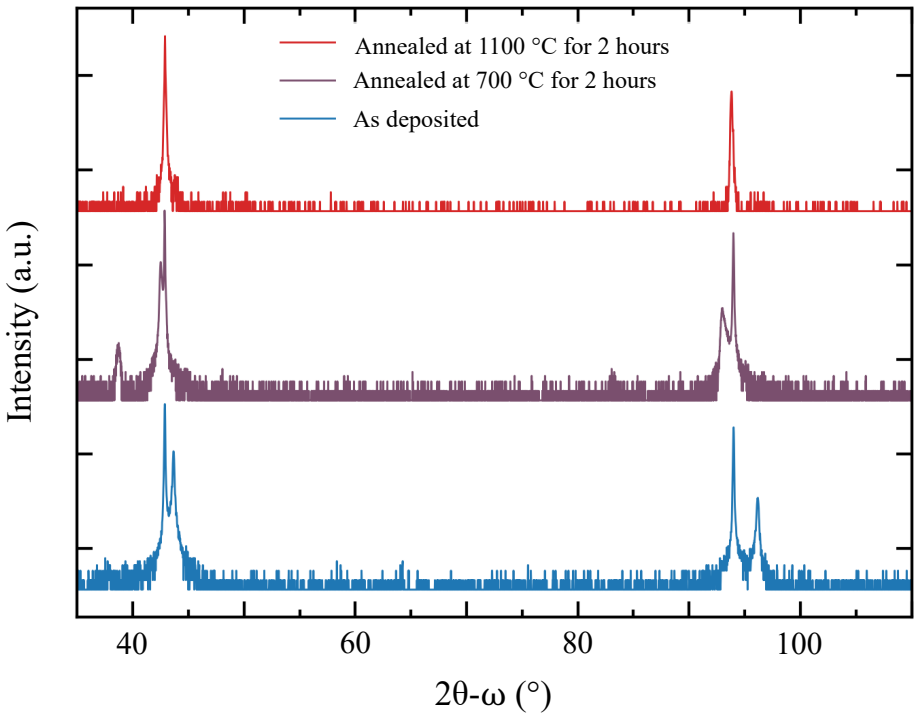


Figure 4.3: XRD data showing an as-deposited film of (MgCoNiCuZn)O deposited at a substrate temperature of 200 ℃ and XRD data following an anneal at 700 ℃ for 2 hours and 1100 ℃ for 2 hours. Following annealing at 700 ℃, a secondary phase peak is observed, while after annealing at 1100 ℃, no film is observed.

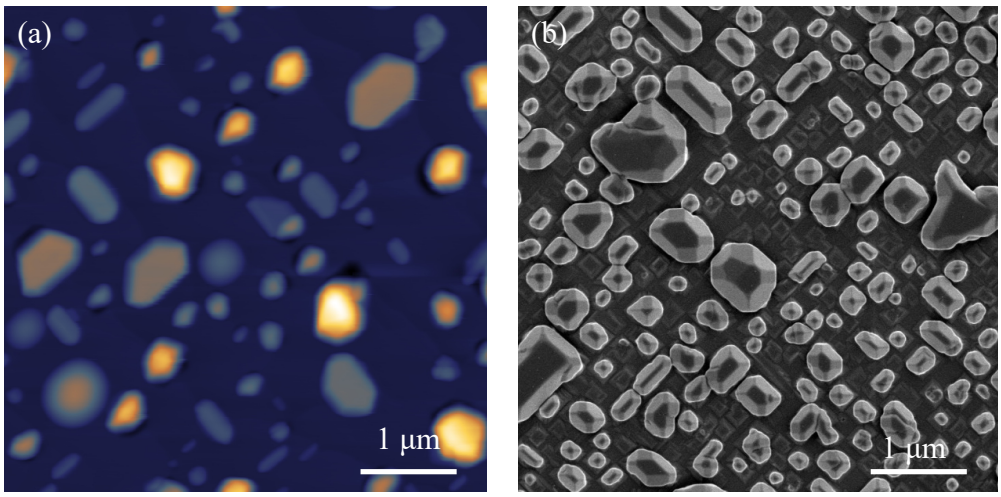


Figure 4.4: (a) AFM image collected using an NT-MDT NTEGRA and (b) SEM image both confirming the presence of particles following dewetting. SEM images were obtained using a Thermo Fisher Scientific Helios 650 Nanolab.

4.3 A new approach to overcoming failure modes

To design a thin film heterostructure with extreme high temperature stability is no easy task. To limit potential failure modes identified in the literature[232–234], our approach featured highly crystalline, immiscible refractory oxides.

As we had already decided to use MgO in our previous structure, due to its refractory properties, and its high availability as a substrate, our approach was to find another oxide to pair with MgO to produce our heterostructure. While it may be desirable to use a similar refractory oxide, for example, NiO, due to its excellent epitaxial match and high melting temperature, the refractive index is too similar to that of MgO[235, 236], and the intermixing would be essentially guaranteed[237].

Instead, we focus on using films comprised of dissimilar crystal structures, with differing ionic radii, with the hopes of reducing the risk of interdiffusion at elevated temperatures.

To this end, we decided to match $BaZr_{0.5}Hf_{0.5}O_3$ with the MgO substrate and film layers. $BaZr_{0.5}Hf_{0.5}O_3$ is a novel perovskite structured material, based on data collected about $BaZrO_3$, which has with a measured lattice parameter of 4.188 Å[238, 239] and a melting temperature of $\sim$ 2700 ºC[240], comparable to the lattice parameter[241] and melting point of MgO[242]. We hypothesized that by adding $BaHfO_3$, we would increase the configurational entropy and thus potentially improve the high temperature stability[165] despite the slight smaller lattice parameter of 4.171 Å[243]. The perovskite structure was chosen with the hypothesis that the difference between the rocksalt (MgO) structure and perovskite structure would limit interdiffusion due to the difference in cation size (Ba^{2+} vs Mg^{2+}) or charge difference (Mg^{2+} vs Hf^{4+}/Zr^{4+}). The similarities between the structures (cubic with similar lattice parameter) allows for greater epitaxial matching, reducing the risk of grain growth or delamination and dewetting at high temperatures.

This selection of a $BaZrO_3$-based material was later confirmed using data from Materials Project[244] in **Appendix C**. This approach can also be used to select other appropriate pairs of materials to suppress unwanted thermal radiation.

In the remaining sections of this chapter, we demonstrate a tunable and wavelength-selective $BaZr_{0.5}Hf_{0.5}O_3$ and MgO heterostructure, capable of suppressing undesired emission. To demonstrate the functionality of this heterostructure, the photonic crystal is utilized as a filter to suppress the emission from an MgO:NiO tape, the most selective emitter to date[210]. The estimated TPV gain at 1500 ºC is approximately 15%. This improvement has the potential of making a significant impact in remote, portable and mobile power systems[27, 245]. This approach is highlighted in **Figure 4.5**. Furthermore, we will investigate the factors that limit the high temperature stability of this approach.

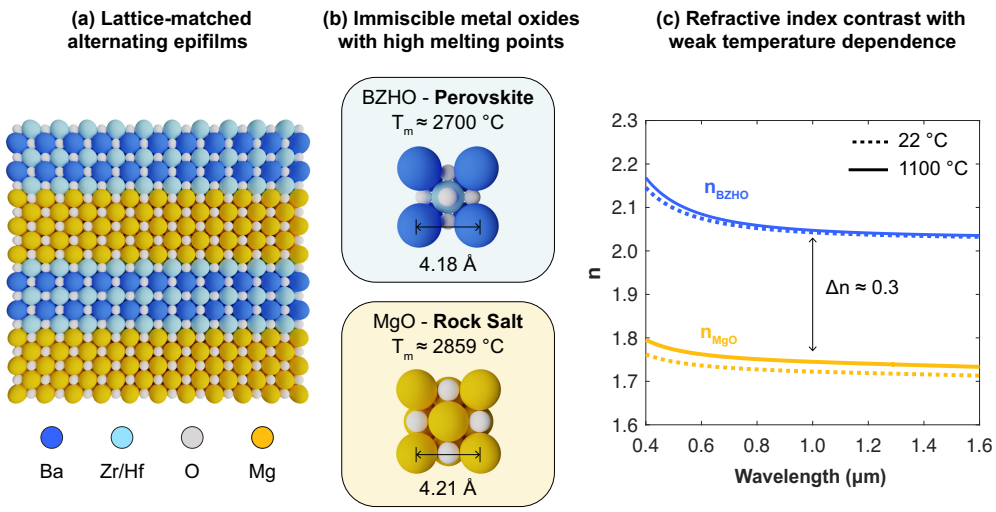


Figure 4.5: (a) Alternating films of $BaZr_{0.5}Hf_{0.5}O_3$ and MgO are chosen because of their low lattice mismatch and high melting temperatures. The high quality epitaxy will limit grain growth at extreme temperatures. (b) $BaZr_{0.5}Hf_{0.5}O_3$ and MgO are refractory oxides with dissimilar crystal structures. (c) Experimentally measured refractive indices of $BaZr_{0.5}Hf_{0.5}O_3$ and MgO[28]. The refractive indices of MgO and $BaZr_{0.5}Hf_{0.5}O_3$ were measured through spectroscopic ellipsometry and thermal emission infrared spectroscopy. Over the wavelength range of 0.4 – 1.6 μm the refractive indices were measured up to 1100 ºC using a custom-built, tip tilt hotstage on a Woollam M-2000 ellipsometer.

4.4 Fabrication and stability of $BaZr_{0.5}Hf_{0.5}O_3$ and MgO heterostructures

MgO and $BaZr_{0.5}Hf_{0.5}O_3$ targets were obtained from Kurt J. Lesker Co. Films were deposited on (001)-oriented MgO substrates by ablation from a 248 nm KrF laser fired at 6 Hz and 1.1 J cm^{-2} for the $BaZr_{0.5}Hf_{0.5}O_3$ target and 5 Hz, 1.8 J cm^{-2} for the MgO target with a spot size of $\sim$ 0.05 cm^2 and 0.11 cm^2 respectively. The substrates were baked at 950 ºC in base vacuum for 20 mins prior to being held at 700 ºC in 100 mTorr of O_2 throughout the deposition. The substrate-target distance is 7 cm. As $BaZr_{0.5}Hf_{0.5}O_3$ is not a known stable bulk phase, the $BaZr_{0.5}Hf_{0.5}O_3$ target was analyzed using XRD and found to be composed of $BaZrO_3$, $BaHfO_3$ and HfO_2 phases, this data is shown in **Figure 4.6**.

Thin films of $BaZr_{0.5}Hf_{0.5}O_3$, with a thickness of approximately 100 nm thickness and $BaZr_{0.5}Hf_{0.5}O_3$/MgO superlattices (10 bilayers) with bilayer thickness of 8 nm were grown epitaxially on MgO (001) substrates via PLD in 100 mTorr of O_2 at 700 ºC. Although thicker bilayers are desirable for thermal emission suppression (IR frequency), thin superlattices were used to characterize the thermal stability as it is easier to observe intermixing, and defect mobility on this length

scale. The perovskite structure of the $BaZr_{0.5}Hf_{0.5}O_3$ film was confirmed using atomic resolution EDS, shown in **Figure 4.7**. Only the Ba and Hf signals were used, as the Zr signal was significantly lower than Hf due to its much lower atomic weight.

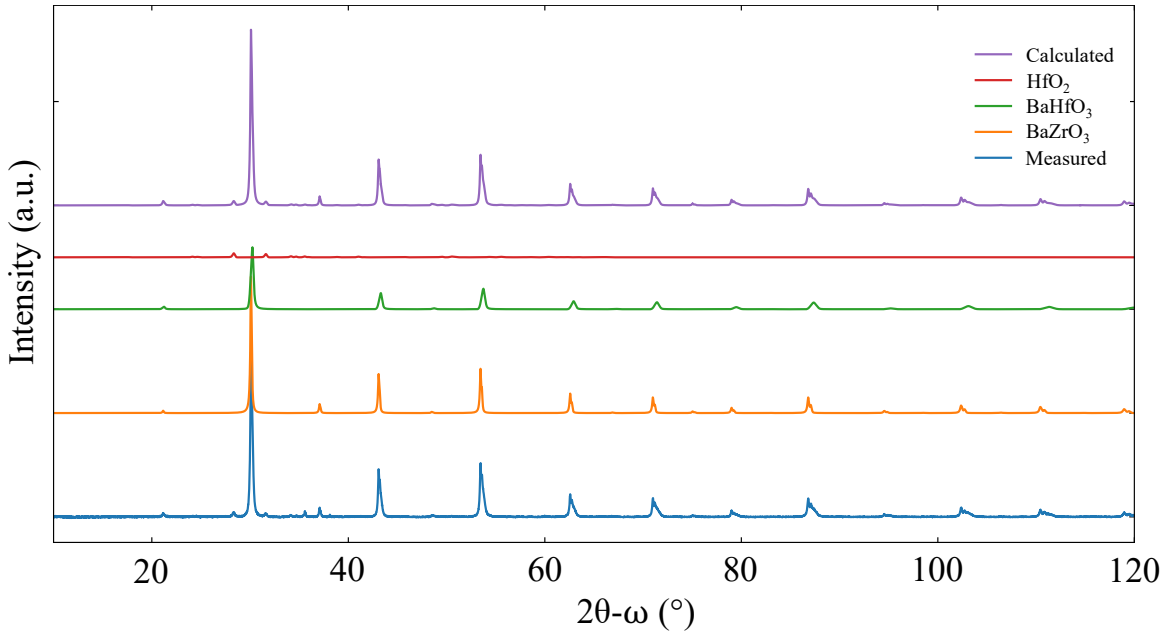


Figure 4.6: XRD analysis of the $BaZr_{0.5}Hf_{0.5}O_3$ target revealing that the target is predominantly composed of $BaZrO_3$ and $BaHfO_3$ perovskite phases, with some HfO_2 impurity phase.

These films were then characterized using in-situ heated XRD, however, prior to annealing the superlattice sample, it was imaged using STEM, so that the structure prior and post-anneal could be compared. It is possible to calculate the superlattice periodicity using both XRD and XRR [246]. Provided the layers in the superlattice are thin and flat enough, the interfaces act like additional scattering centers, resulting in satellite peaks around an average XRD diffraction peak for the constituent materials[247].

A heating stage is used to hold the samples at temperature intervals from 300-1100 ℃, holding for 1 hour at each temperature. The same measurement was also conducted on both a single $BaZr_{0.5}Hf_{0.5}O_3$ thin film and a $BaZr_{0.5}Hf_{0.5}O_3$/MgO superlattice structure. From **Figure 4.8**, we observe that above 900 ℃, a secondary phase is observed close to 34°, in both the superlattice sample and the single film sample. It is clear from this measurement that the secondary phase formation is degradation of the $BaZr_{0.5}Hf_{0.5}O_3$ phase, however both the superlattice and single film samples are not completely degraded at this temperature. Without more information, we cannot say for certain what phase is responsible for this peak, however, it is consistent with a textured monoclinic HfO_2-like structure.

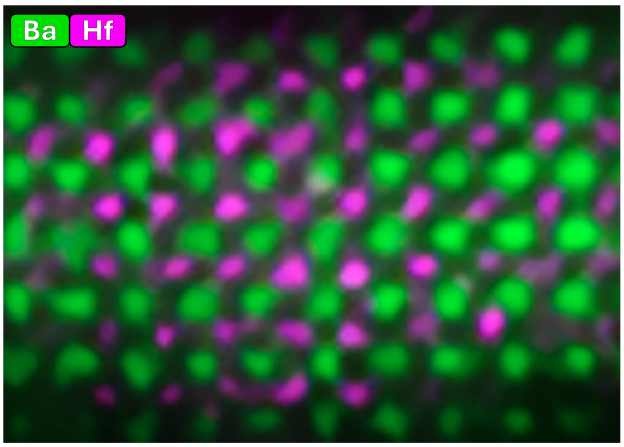


Figure 4.7: Average background subtraction filtered, up-scaled atomic resolution STEM-EDS image of Ba and Hf cations in the $BaZr_{0.5}Hf_{0.5}O_3$ phase. The arrangement is consistent with a perovskite structure with Ba on the A-site and Hf on the B-site.

From XRD alone, it is not possible to discern this mechanism, however, literature suggests that it may be through the reaction of Ba with water in the air to form a gaseous hydroxide, which is subsequently evolved from the superlattice[248, 249]. An HfO_2 secondary phase would be consistent with the loss of Ba from the $BaZr_{0.5}Hf_{0.5}O_3$ phase, leaving Hf and Zr cations with an excess of oxygen.

With the hypothesis that Ba is being lost from the structure through reaction with water, the next step was to anneal a similar superlattice in a different atmosphere. Initial studies were done with N_2 (inert) atmospheres. Once it was confirmed that the superlattice was stable at 1100 ºC in an inert atmosphere, we changed to a dry air atmosphere (below 200 ppm water vapor).

The results for the dry air anneal are shown in **Figure 4.9**, where it is observed that the structure is phase stable for 24 hours at 1100 ºC in dry air. Above this temperature, there is formation of a secondary phase along with degradation of the superlattice. A new sample was used following each degradation, but each sample was deposited at the simultaneously by utilizing three substrates on the PLD substrate heater at once. The improved phase stability of the superlattice in dry air supports our hypothesis that a reaction with water was responsible for the formation of the secondary phase. Additionally, it is important to note that no dewetting or delamination is observed, as was the case with the (MgCoNiCuZn)O approach.

Later, a new sample (14 bilayers) was annealed for up to 168 hours (1 week) at 1100 ºC in dry air, to confirm the stability at this temperature (**Figure 4.10**). No degradation of the superlattice is observed, although the $BaZr_{0.5}Hf_{0.5}O_3$ 001 XRD peak intensity does appear to be enhanced following the anneal.

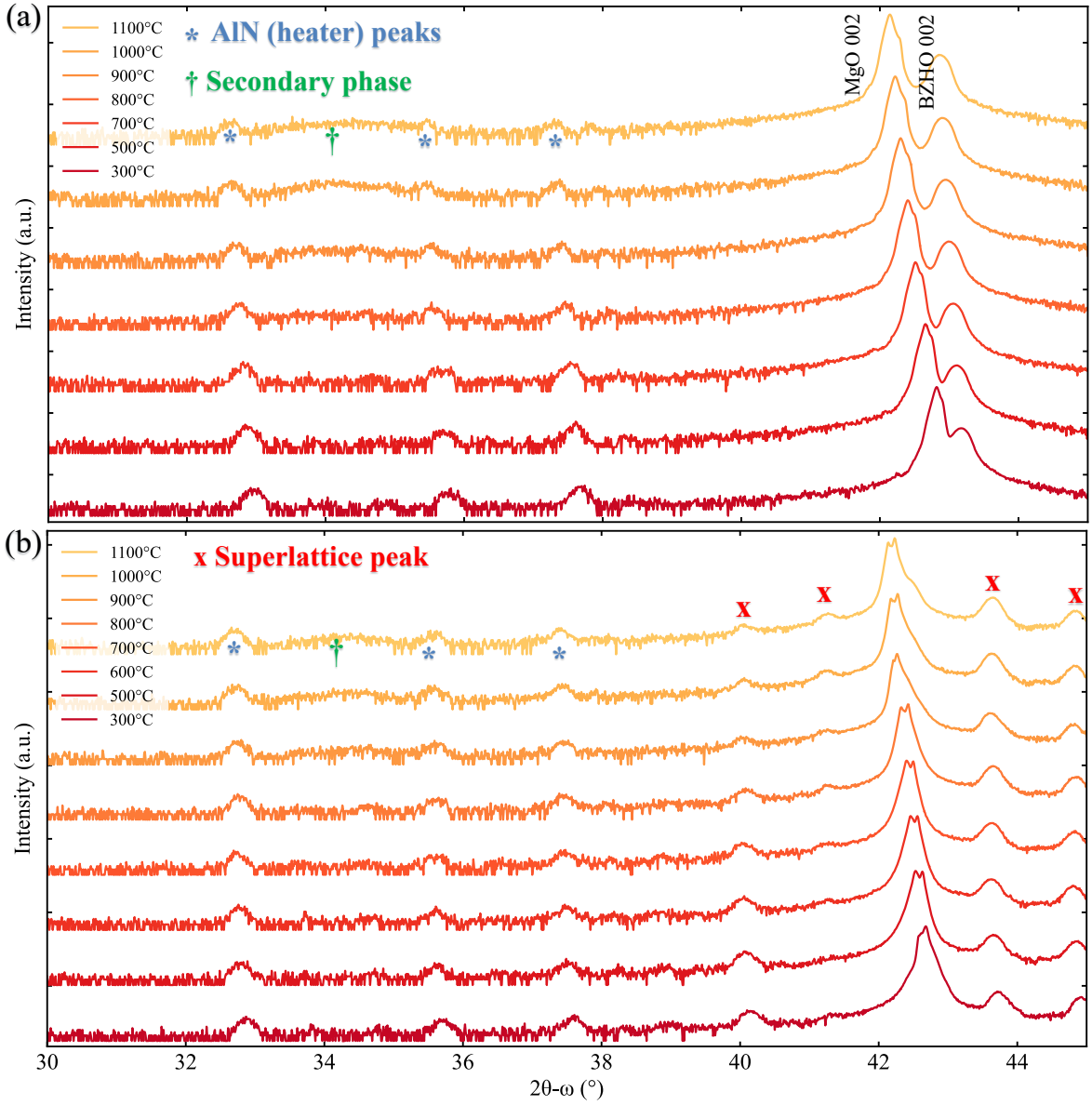


Figure 4.8: (a) XRD data showing in-situ annealing of a $BaZr_{0.5}Hf_{0.5}O_3$ single thin film at temperature intervals from 300-1100 ºC. No change was observed between the as-deposited film and the film at 300 ºC. At approximately 900 ºC, a secondary phase is observed at around 34º. (b)XRD data showing in-situ annealing of a $BaZr_{0.5}Hf_{0.5}O_3$ and MgO superlattice at temperature intervals from 300-1100 ºC. Similarly, at approximately 900 ºC, the same secondary phase is observed at around 34º. The peaks from the AlN XRD heater are also marked.

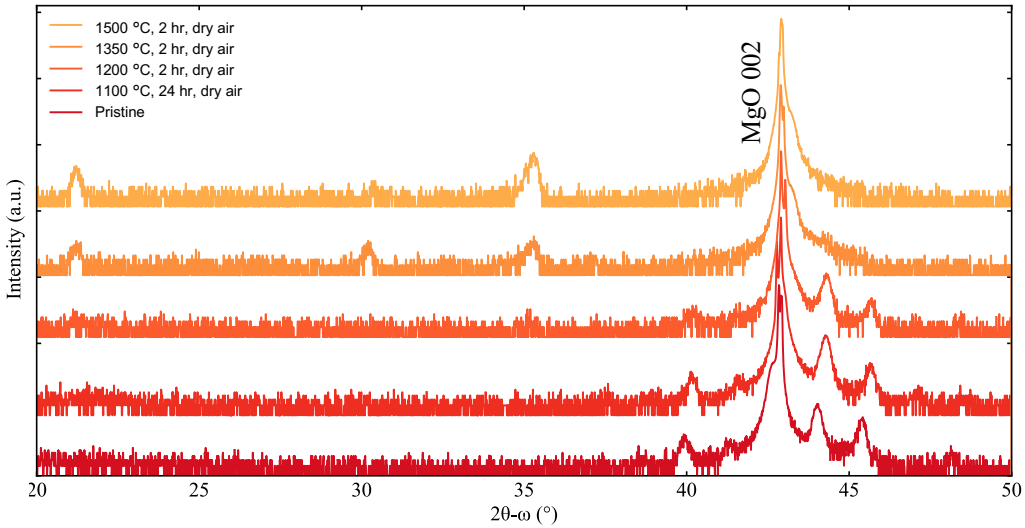


Figure 4.9: XRD data showing an as-deposited superlattice, as well as samples annealed in dry air at 1100 ℃ for 24 hours, 1200 ℃ for 2 hours, 1350 ℃ for 2 hours and 1500 ℃ for 2 hours. The same sample was used for the 1100 ℃ and 1200 ℃ anneals. Due to degradation other samples (deposited concurrently to the first) were used for the remaining anneals.

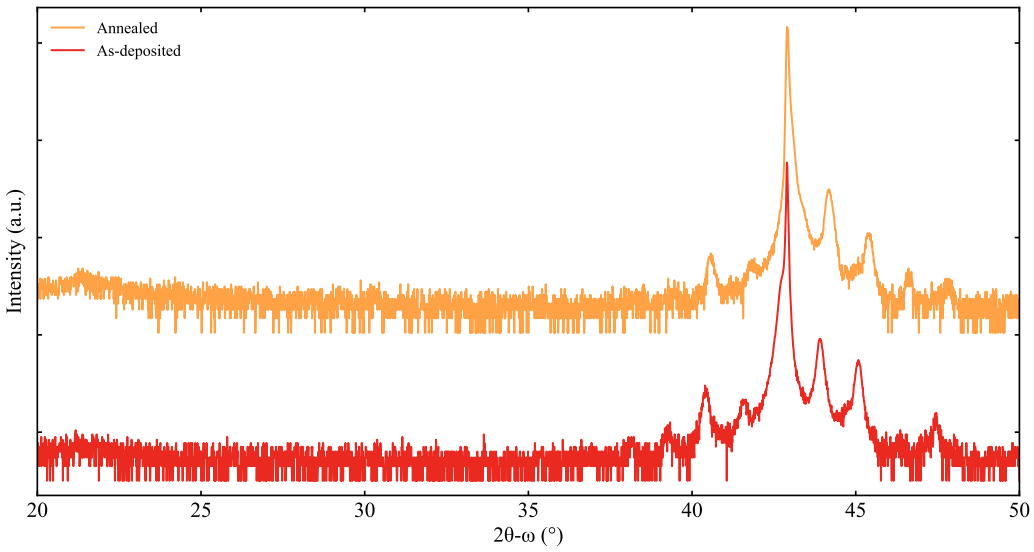


Figure 4.10: XRD data showing an as-deposited superlattice, as well as following a 168 hour anneal at 1100 ℃ in dry air.

At this point, we are aware of the limits of the thermal stability of the superlattice structure, and a basic understanding that it is limited by the stability of the $BaZr_{0.5}Hf_{0.5}O_3$ phase in moist air, which partially degrades to precipitate a small amount of secondary phase at 1100 ºC.

To further investigate the thermal stability and failure, STEM-HAADF imaging was used to reveal the high quality superlattice structure prior to annealing and after annealing in (moist) air. The sample from **Figure 4.8** was used for this part of the investigation. The analysis is shown in **Figure 4.11**. From this it is also possible to confirm the bilayer period calculated by fitting the XRD as $\sim$ 8 nm. We observe a large contrast in the HAADF imaging, due to the large difference in atomic number between Mg and the cations in $BaZr_{0.5}Hf_{0.5}O_3$. This reveals an abrupt and atomically sharp interface between the MgO substrate and the first $BaZr_{0.5}Hf_{0.5}O_3$ layer before (**Figure 4.8(a)**) and after annealing (**Figure 4.8(b)**). It is then observed that later layers remain continuous, without evidence of intermixing or coarsening following annealing (**Figure 4.8(c-h)**). To further probe any intermixing EDS was used to probe the composition in a line along the superlattice layers, revealing a clear periodicity in the Mg and Ba, Zr, Hf concentrations, with the distribution of each element retains its sharpness across each interface following the anneal. No phase changes are observed. These images were obtain using an aberration corrected JEOL 3100 R05 microscope operated at 300 kV, with a probe convergence angle of 22 mrad. EDS data were collected using a Thermo Fisher Scientific Talos F200X G2 STEM operated at 200 kV and equipped with a Super-X EDS detector.

This result demonstrates the effectiveness of this approach in avoiding common failure modes at elevated temperatures in nanophotonic materials such as grain-growth degradation, interlayer mixing, and oxidation. However, we are still not sure of the optical stability (how the functional properties behave under these extreme conditions) of the material.

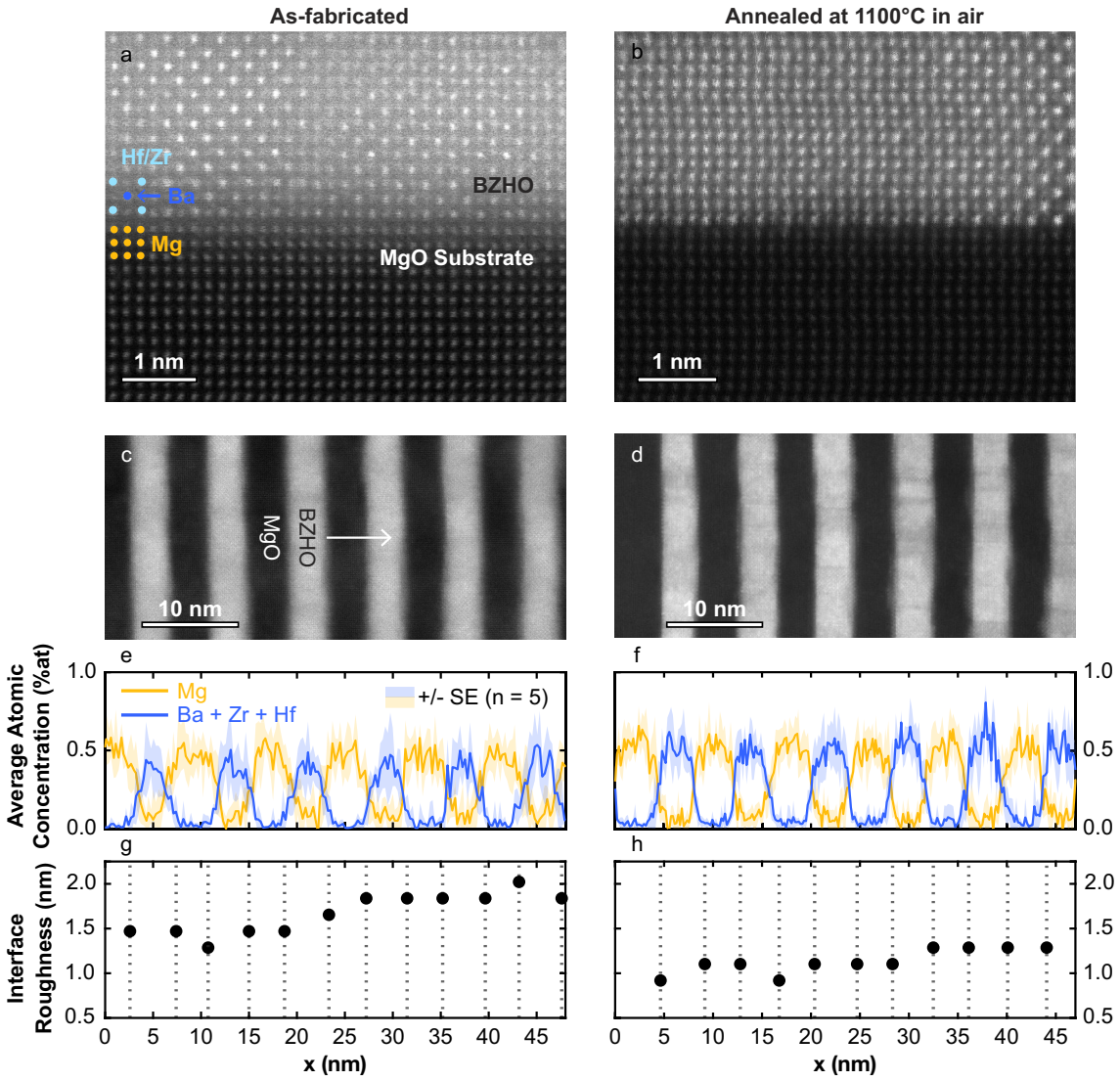


Figure 4.11: (a) STEM-HAADF imaging of the $BaZr_{0.5}Hf_{0.5}O_3$ superlattice prior to and (b) post-anneal, highlighting the preservation of the epitaxial flat interface at the substrate. (c) Superlattice layers 1-10 showing the layer roughness and intermixing prior to and (d) post-anneal. (e) EDS line scan along the above images, showing the conservation of distinct compositional regions before and (f) post-anneal. (g) analysis of the interface roughness showing no change prior to and (h) post-anneal. Roughness increases in the growth direction due to thermodynamic conditions during synthesis.

4.5 Optical performance under extreme conditions

Now that it has been demonstrated that thin $BaZr_{0.5}Hf_{0.5}O_3$/MgO heterostructures are stable in dry air up to 1100 ºC, it is necessary to evaluate the functional properties of these structures at elevated temperatures. For this purpose, we use a photonic crystal design for control of thermal emission. These photonic crystals are grown in the same manner as the $BaZr_{0.5}Hf_{0.5}O_3$/MgO superlattices, using PLD, however the bilayer thickness is now optimized to be half of the selected cut-off wavelength. Due to the unusually large thicknesses required and the limitations of PLD, we limited our structures to two-and-a-half bilayers.

Given their high temperature stability, $BaZr_{0.5}Hf_{0.5}O_3$/MgO photonic crystals can be deployed as spectral filters that are separated from the emission source by a small gap. The thermal break created by the gap allows the filter to be paired with ultrahigh-temperature sources (e.g., 1500 ºC). To demonstrate this strategy, the structure is paired with a 1770 ºC silicon carbide (SiC) thermal source. This optical measurement setup is shown in **Figure 4.12(a)**. In this experiment, the $BaZr_{0.5}Hf_{0.5}O_3$/MgO structure is separated from the heated SiC source by a small air gap, but the filter can also be directly attached to a 1500 ºC emitter with ceramic posts[28]. These thermal emission measurements were taken with a Nicolet iS50 Fourier-transform infrared spectrometer (FTIR).

The optical characterization in this configuration is shown in the bottom panel of **Figure 4.12(b)**, lowering the emission peak and the overall apparent emissivity of the SiC emitter, this capability is desirable in high-temperature environmental barrier coatings.

In addition, by growing structures with different bilayer thicknesses, we demonstrate the tunability of this approach. In **Figure 4.12(c)**, we show the different suppression wavelengths achieved, and the optical properties of each structure before and after annealing for 12 hours at 1100 ºC in dry air. A negligible change in transmittance is observed, and the suppressed wavelength is shifted to a slightly longer wavelength in each sample. This result represents a significant improvement in extreme temperature stability in an atmosphere containing oxygen, and is comparable to many vacuum and inert atmosphere reports[31–34, 48, 49, 213–222, 229, 250–253].

The results presented here demonstrate that an all-oxide tunable $BaZr_{0.5}Hf_{0.5}O_3$/MgO photonic crystal can be used to improve the emission profile of certain bulk emission sources (SiC and NiO:MgO[28]).

However, in the thick photonic crystal heterostructure, where the bilayer thickness is approximately 50× that of the thin superlattice samples, we observe a small fraction of polycrystalline $BaZr_{0.5}Hf_{0.5}O_3$ likely due to defects introduced during the on-going deposition process. The XRD

data confirming this polycrystalline fraction is shown in **Figure 4.13(a)**, where it is observed that the 001 and 002 reflections are much more intense than the 011 reflections. In the bulk sample, the 011 reflections is expected to be the highest for a general perovskite crystal, and thus we can say that this polycrystalline fraction must be small, and the majority of the crystal is at least textured if not epitaxial. As well as this, we noted a significant discrepancy in the filtering capabilities of the photonic crystal when compared to an ideal reflector model, shown in **Figure 4.13(b)**. This reduced efficacy is likely a result of the polycrystalline crystal structure, as the optical properties of the photonic crystal are linked with the structural properties.

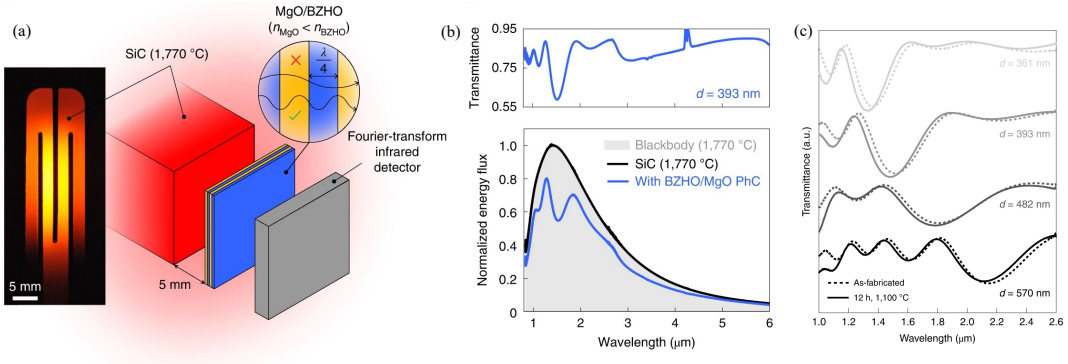


Figure 4.12: (a) Schematic illustrating the optical characterization setup utilizing emission from a SiC heater. (b) Optical measurements of a $BaZr_{0.5}Hf_{0.5}O_3$/MgO photonic crystal with two-and-a-half bilayers demonstrating suppression of thermal emission. (c) Transmission spectra of $BaZr_{0.5}Hf_{0.5}O_3$/MgO photonic crystals with varying bilayer thicknesses, before and after annealing at 1100 ℃ for 12 hours in dry air. The change in optical transmittance is negligible following annealing.

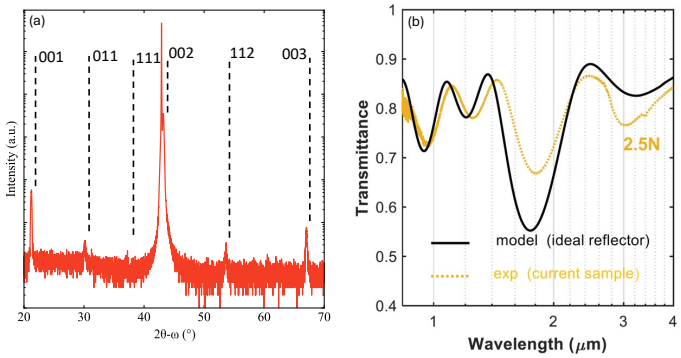


Figure 4.13: (a) XRD data from a $BaZr_{0.5}Hf_{0.5}O_3$/MgO photonic crystal with two-and-a-half bilayers deposited on an MgO (001) substrate, exhibiting a textured polycrystalline structure. $BaZr_{0.5}Hf_{0.5}O_3$ polycrystalline film peaks are labeled. (b) Model (ideal reflector) calculated versus experimental transmittance data for a partially polycrystalline $BaZr_{0.5}Hf_{0.5}O_3$/MgO photonic crystal, with a significant discrepancy between the expected and measured results.

4.6 Investigating the failure mechanism

Following the discovery of this reduced efficacy, further study was warranted to investigate the polycrystalline nature of the thick photonic structure, and whether this could be related to the failure of the superlattices at elevated temperatures. Using SEM imaging, it was possible to image the surface and cross-section of the photonic crystal with two-and-a-half bilayers, shown in **Figure 4.14**. The surface shows an uncommonly rough surface, appearing to be the result of the fusion of many small islands or grains. While in the cross-sectional image, the first bilayer appears to have a very low roughness, further deposition beyond this appears significantly less homogeneous, with many protrusions from the surface of each layer.

We hypothesize that this is the result of a Stranski-Krastanov growth mode (layer-by-layer plus islands) caused by further deposition on layers that are already populated with defects due to strain relaxation[254]. Deposition on top of these defects, then results in the formation of islands, eventually causing the complicated surface observed in **Figure 4.14**, by the merging of many such overgrowths.

Although, $BaZr_{0.5}Hf_{0.5}O_3$ and MgO were chosen, in part, for their lattice matching, our calculations have revealed a strain of $\sim 0.77\%$ at 700 ºC (for $BaZrO_3$ and MgO). From **Figure 1.1**, this is shown to be comparable to several thousand Kelvin, so it is certainly likely to have an impact on the film structure and failure.

Even if the first layers of deposition are fully strained (and thus free of dislocations), and thus provide a perfect template for the next layer of deposition, eventually thickening of the film will be accompanied by some strain relaxation process, as the large strains that can be accommodated in thin films are not able to be maintained into an indefinite thickness[255, 256]. It is expected that beyond a certain critical thickness, thin films will relax to form misfit dislocations due to lattice mismatch, this thickness, h_c, can be estimated using **Eq. 4.1**[257–260], where b is the extension of the misfit dislocation, ν is Poisson's ratio of the film and ϵ_0 is the lattice misfit at growth temperature.

$$h_c = \frac{b}{4\pi(1+\nu)\epsilon_0}\left(ln\left(\frac{h_c}{b}\right)+1\right) \tag{4.1}$$

Using the co-efficient of thermal expansion (CTE) of $BaZrO_3$ ($\sim$ 8 ºC^{-1}[261]) and MgO ($\sim$ 12 ºC^{-1}[262] averaged over the range 0-700 ºC), we can calculate an estimated misfit strain of $\sim 0.77\%$ at 700 ºC.

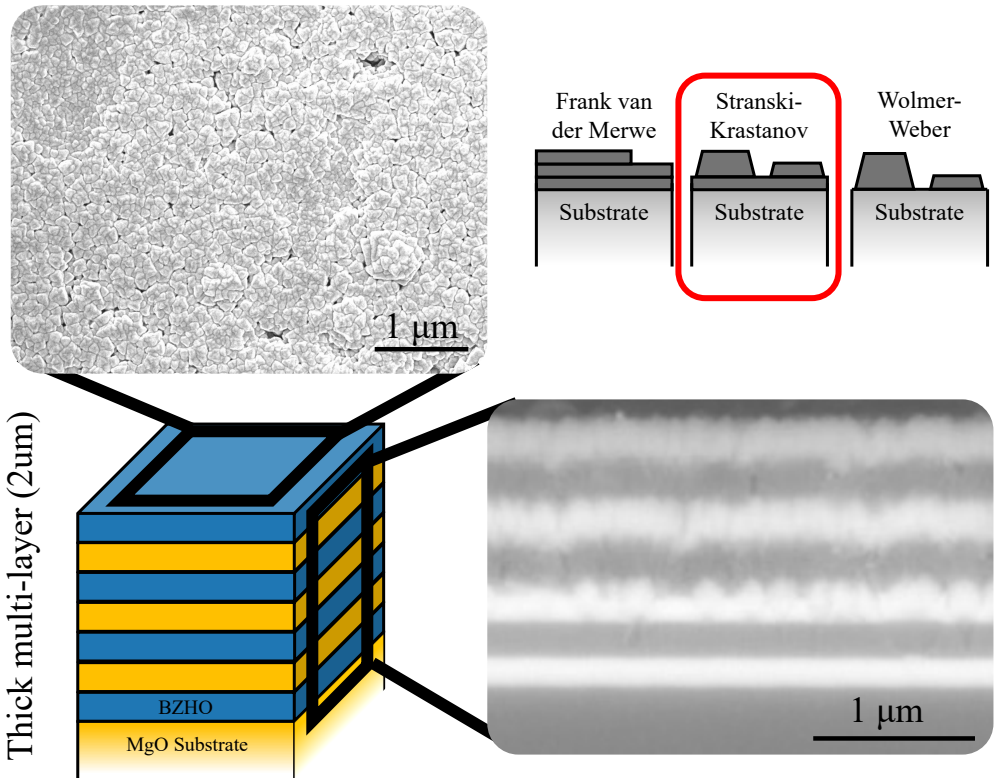


Figure 4.14: SEM images collected using an ETD, displaying the surface structure and a cross-sectional structure (following cleaving) of a photonic crystal with two-and-a-half bilayers. A schematic of different film growth modes is included, with Stranski-Krastanov, the most likely growth mode, highlighted.

In the perovskite system, dislocations can occur along <100> directions[263, 264], meaning that taking b as the lattice parameter of $BaZrO_3$ is a reasonable approach. Along with a Poisson's ratio of 0.237[261], we estimate a critical thickness of 16.3 nm for $BaZrO_3$.

Although each individual layer in the superlattice samples is less than 5 nm thick, the total $BaZr_{0.5}Hf_{0.5}O_3$ thickness in a $BaZr_{0.5}Hf_{0.5}O_3$/MgO superlattice with 10 bilayers is over twice this calculated critical thickness, and so it is possible that this strain relaxation could be related to the partial formation of secondary phase that was observed in samples at elevated temperatures (**Figure 4.9** and **Figure 4.10**).

To investigate whether this growth mechanism and strain was pertinent to the failure under extreme thermal conditions, a number of new samples were grown, with superlattices ranging from 8 to 18 bilayers. XRD data was collected, and no significant change was observed from the sample with 8 bilayers to the sample with 18 bilayers, with all samples exhibiting XRD comparable to **Figure 4.10** prior to annealing. A RSM was collected to assess the strain relationship between

the film and the substrate, however due to the close lattice matching, no substantive conclusions could be drawn.

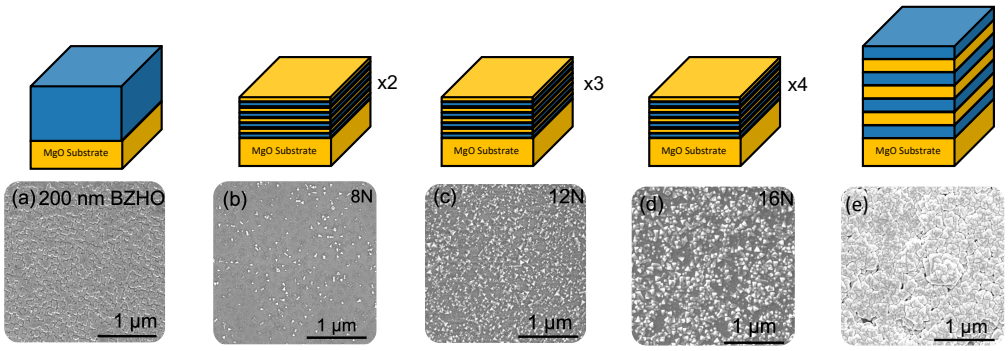


Figure 4.15: Top-down SEM images illustrating strain evolution. (a) A single $BaZr_{0.5}Hf_{0.5}O_3$ thin film exhibits a growth mode that includes the formation of square islands. In a (b) superlattice with 8 bilayers, a mixture of square and triangular islands are observed. In (c) and (d) with increasing number of layers, a significant increase in triangular island density is observed. In the photonic crystal ($\sim$ 2 μm thick) sample, these islands appear to have fused to form an uneven surface.

Instead, SEM was used to determine the surface morphology and growth mode of the superlattice. <100>-orientated "square" islands, averaging $\sim$ 100 nm in length and at a density of $\sim$ 70 μm^{-2}, are observed on the surface of the thick $BaZr_{0.5}Hf_{0.5}O_3$ single layer film, shown in **Figure 4.15**. In the thin superlattice samples, a change in the surface defects is observed with an increase in the number of bilayers, reinforcing the hypothesis that it is in some way related to strain and the thickness beyond the critical thickness. In the thinnest superlattice sample, consisting of only 8 bilayers of $BaZr_{0.5}Hf_{0.5}O_3$ and MgO, a mixture of both square and triangular defects are observed. From STEM imaging in cross-section, the height of these defects can be estimated to be between 10 and 50 nm and appear to retain layers of the superlattice. As the number of bilayers (total thickness) increases, the square defects are no longer observed and the density of the triangular defects increases from $\sim$ 30 to $\sim$ 220 μm^{-2}. These triangles primarily appear along the <110> directions.

From this, it appears that the surface defects observed in the thick photonic crystal originate as square protrusions on the $BaZr_{0.5}Hf_{0.5}O_3$ layer. An interaction with the MgO layer then results in these triangular growths, that eventually fuse to form an irregular surface, as observed. It is important to note that even at 16 bilayers, the total thickness is still only expected to be 128 nm, just over half the thickness of the single $BaZr_{0.5}Hf_{0.5}O_3$ film. Despite this, the density of defects on the surface of the $BaZr_{0.5}Hf_{0.5}O_3$ film is lower than the defect density of the sample with 16 bilayers, 70 μm^{-2} compared to 220 μm^{-2}. This observation reinforces the hypothesis that the interaction of strain between the $BaZr_{0.5}Hf_{0.5}O_3$ and MgO layers is resulting in more defects.

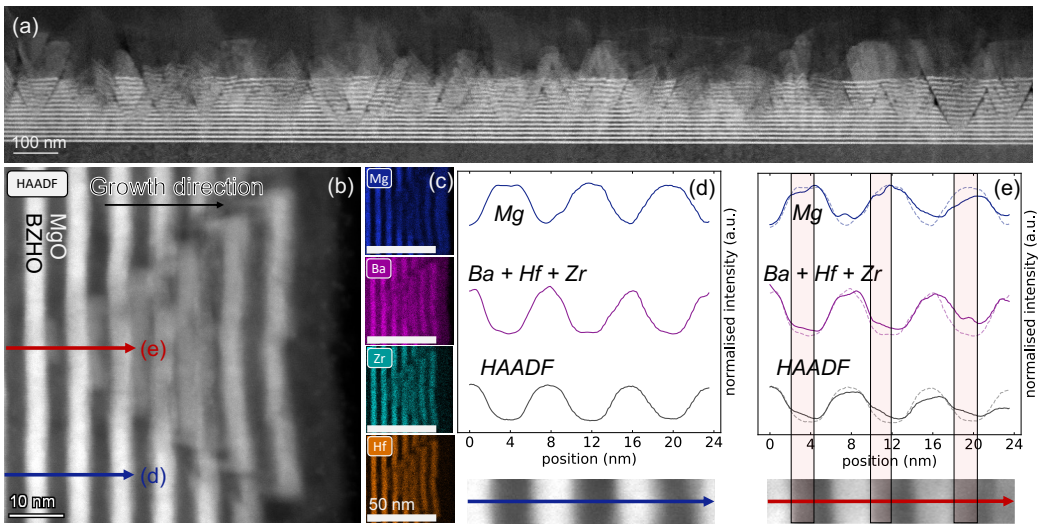


Figure 4.16: Cross-sectional STEM-HAADF imaging along the <100> direction of the substrate. (a) A significant number of defects are observed that extend from the bulk of a superlattice with 14 bilayers through the surface. (b) Image of an isolated defect in a superlattice sample with 10 bilayers, appearing to originate from a defect in the fourth $BaZr_{0.5}Hf_{0.5}O_3$ layer (first layer shown in this image). (c) EDS of the same region showing no compositional variation across the defect. (d) and (e) EDS and HAADF intensity linescans from the regions marked in (b). The data in (d) is also shown in (e) for comparison. Linescan (e) shows clear anomalies in the composition and HAADF intensity at the origin of the defect and at the start of each subsequent layer, indicating that the protrusion is continued through the rest of the superlattice sample.

To look beyond the surface of these samples and further understand the origin of these surface defects, cross-sectional STEM-HAADF and EDS data were collected using a Thermo Fisher Scientific Talos F200X G2 S/TEM operated at 200 kV and equipped with a Super-X EDS detector. A superlattice with 10 bilayers was imaged (**Figure 4.16**).

The first three layers of the superlattice are observed to be defect free, equivalent to a total thickness of 12 nm of $BaZr_{0.5}Hf_{0.5}O_3$ and another 12 nm of MgO. This is slightly larger than the predicted critical thickness, however this can be understood by the theoretically perfect lattice match between the MgO films and the substrate. In a typical Stranski-Krastanov growth mode, only the first few monolayers are expected to be defect free[265], potentially suggesting that the initial growth is not Stranski-Krastanov, and a transition in growth mode occurs during deposition.

From **Figure 4.16(b)**, it is clear that the first island or "bump" is seen in the 4th $BaZr_{0.5}Hf_{0.5}O_3$ layer, before progressing through the superlattice, as indicated by the atomic weight contrast. However, no difference in nanobeam electron diffraction is observed in these regions. In these regions, the superlattice appears to be offset by half a period but preserved, explaining why there is no clear evidence of these defects in diffraction.

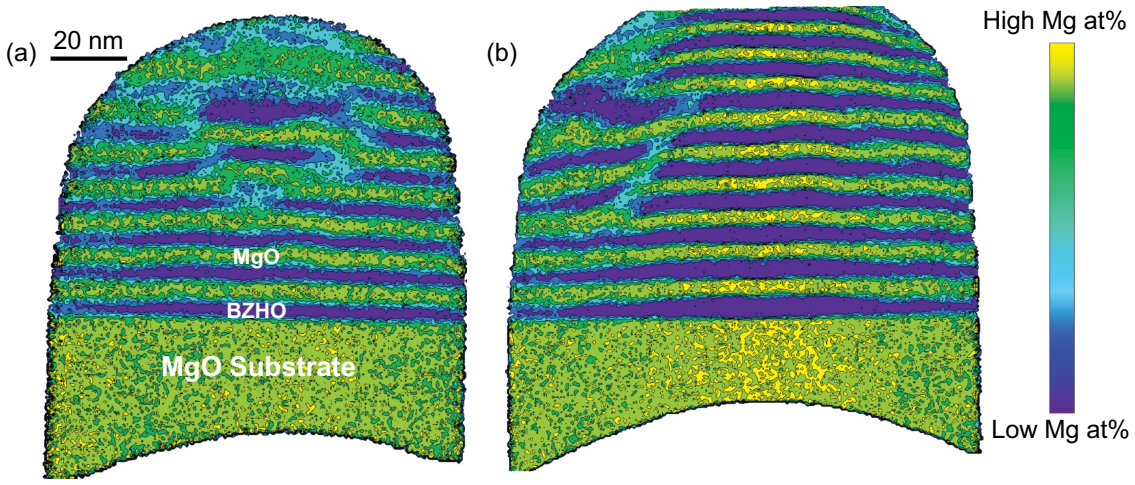


Figure 4.17: 2D slice of Mg concentration from APT. (a) and (b) represent two 10 nm thick 2D slices through a 3D reconstruction of the defect, at perpendicular directions.

In the SEM imaging in **Figure 4.15**, it is observed that these islands occur as rectangular (approximately square) overgrowths. However, in the superlattice structure, once one of these islands has formed in the $BaZr_{0.5}Hf_{0.5}O_3$ layer, the deposition is terminated and an MgO layer is deposited on top of it. We hypothesize that this leads to the defect structure observed simply due to the periodic deposition process. By depositing another layer over this bump, as the layers are immiscible, the bump embosses the next layer, resulting in an increase in size with each added film. This evolution is visible in both the HAADF and EDS images, the analysis of which is shown in **Figure 4.16(e)**. In this analysis, it is clear that the initial bump is comprised of a $BaZr_{0.5}Hf_{0.5}O_3$ protrusion into an MgO film, as there is a drop in Mg EDS intensity and an increase in Ba, Hf and Zr intensity. This change in intensity is low, as the STEM images an entire column of atoms in a cross-section roughly 20 nm thick.

From this analysis alone, the 3D structure and progression of these defects cannot be fully understood. From **Figure 4.15**, it is known that these defects appear as either rectangles or triangles on the surface of the film, and from **Figure 4.16**, it is known that the cross-sectional of these defects is a triangle. Using atom probe tomography (APT), it is possible to discern the 3D composition by removing atoms slowly using a laser and detecting them with a time-of-flight detector[266]. This can then be reconstructed to produce a 3D profile. In **Figure 4.17**, two perpendicular 2D slices through a $BaZr_{0.5}Hf_{0.5}O_3$/MgO superlattice sample.

There is a clear triangular outline to the defect in both of the two arbitrary perpendicular views, marked with an increased Mg concentration compared to the $BaZr_{0.5}Hf_{0.5}O_3$ film layers. This suggests that the defect is either pyramidal or conical in structure. Based on the surfaces observed

in **Figure 4.15**, it seems that either an inverted rectangular or triangular-based pyramid is most likely. Additionally, further STEM images, taken along the <110> zone axis, revealed a broader triangular cross-section with a wider apex angle.

In **Figure 4.17(a)**, a protrusion is observed in the 4th $BaZr_{0.5}Hf_{0.5}O_3$ layer from the substrate, consistent with the observations in **Figure 4.16(b)**. Using APT we are able to observe that this protrusion produces an anti-phase region, where the superlattice is shifted approximately 1/2 layer from the defect-free regions. Unlike in the STEM images, in the APT, we are able to observe an increase in Mg concentration in the $BaZr_{0.5}Hf_{0.5}O_3$ layers at the edge of the defect. We believe these regions are acting as diffusion channels, resulting in the high Mg concentration. There are already reports of extended defects such as misfit dislocations acting as easy diffusion paths in superlattice materials due to lower barriers to diffusion[267]. We also observe several seemingly discontinuous MgO layers around the defective region. It is possible that this is a result of tilt of the defect relative to the APT axis. However, it could also be a result of the displaced Mg concentration along the defect boundaries.

To investigate the interaction of these defects with the failure mechanism of the superlattice, in-situ high temperature STEM imaging was utilized. This allows rapid heating of the superlattice in-vacuo to 1000 ºC. It is unknown how the superlattice will behave in an evacuated environment, as it has only been tested in inert and air atmospheres. Additionally, as the sample must be thinned (to $\sim$ 20-50 nm) to make a cross-section, it is expected that degradation will progress more expediently.

High temperature STEM was performed using a Protochips Fusion Select holder with the sample deposited on a Vacuum Only, Carbon Coated MEMS chip, to a max temperature of 1000 ºC at a rate of 100 ºC min^{-1}; image series were recorded at 3 Hz for $\sim$ 60 minutes. The results are illustrated in **Figure 4.18**. In **Figure 4.18(a)-(f)** the progression of degradation is observed at the thinnest section of the cross-sectioned sample over a period of roughly two minutes. The degradation is observed to begin in the upper regions of the superlattice, where the most defects are present and the stabilizing influence of the substrate is reduced due to strain relaxation. Post-cooling analysis, shown in **Figure 4.18(g, h)**, shows a partially degraded superlattice, where regions of the superlattice that were defect-free were preserved through the heating treatment. Decomposition appears to occur through the loss of Ba to the vacuum (similar to the loss of Ba to reaction with water in non-dry air), leaving behind a phase containing Hf and Zr cations. In **Figure 4.18(l, m)**, nanobeam diffraction for the region highlighted in **Figure 4.18(h)** shows an atypically large number of diffraction spots. Nanobeam diffraction is comparable to XRD but using an electron beam rather than X-rays. The simulated diffraction fits a combination of MgO and an HfO_2-based phase, consistent with the secondary phase observed in earlier XRD.

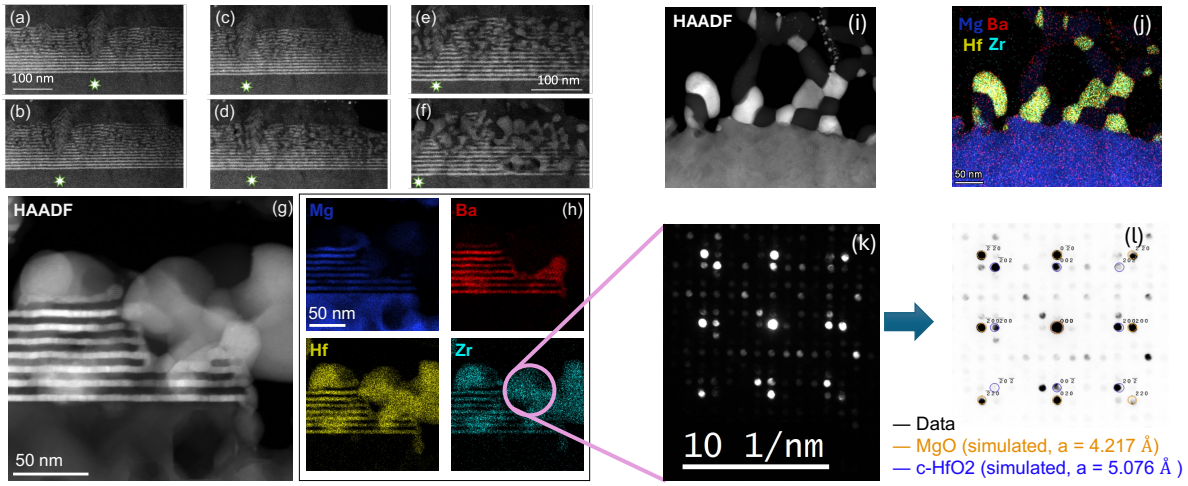


Figure 4.18: High temperature STEM. [(a)–(f)] STEM-HAADF images of a superlattice with 14 bilayers, held in-vacuo and at 1000 ºC in-situ over a period of 2 min at (a) 47, (b) 54, (c) 60, (d) 92, (e) 104, and (f) 164 s after reaching 1000 ºC. The star marks an approximately fixed position on the sample. (g) STEM-HAADF image of a partially degraded superlattice following cooling from 1000 ºC. (h) STEM-EDS mapping of Mg, Ba, Hf, and Zr composition of the region shown in (g) after heating for $\sim$ 50 min at 1000 ºC. (i) STEM-HAADF image of completely degraded region of the superlattice following the same treatment as (g). (j) STEM-EDS composite image of Mg, Ba, Hf, and Zr concentration, illustrating the total loss of Ba. (k) Nanobeam diffraction of the region highlighted in (h) and (l) the calculated single crystal diffraction patterns for (k).

Based on this observation, we hypothesize that despite the difference in heating techniques, a similar failure mechanism is occurring in other atmospheres, that being the loss of Ba around the edge of the defects. The preservation of the initial superlattice layers can explain why the superlattice is conserved despite the presence of secondary phase in **Figure 4.8**. Additionally, the survival of the remaining undamaged superlattice structure in **Figure 4.18** following heating at 1000 ºC, supports our prior findings that MgO and $BaZr_{0.5}Hf_{0.5}O_3$ are highly immiscible[28].

A thinner region, exhibiting total failure, is shown in **Figure 4.18(i, j)**, where a near total loss of Ba is observed, leaving only an agglomerate of MgO and regions of (Hf, Zr)O_2. HfO_2 is known to be a stable phase and has already been utilized in other filtering heterostructures[48, 213].

4.7 Conclusion: the stability of optical heterostructures

In this chapter we have demonstrated a photonic crystal capable of filtering undesired thermal radiation at extreme temperatures.

Initially, an attempt was made to produce a photonic crystal heterostructure using two different

(MgCoNiCuZn)O structures with different optical properties. However, using XRD and annealing treatments it was found that this heterostructure failed at comparably low temperatures ($<$ 400 ºC), due to layer intermixing, because of the similarity of the two different (MgCoNiCuZn)O structures. Additionally, we demonstrated that a heterostructure utilizing a different pairing of (MgCoNiCuZn)O and another oxide was also not viable. This is because (MgCoNiCuZn)O exhibits the formation of a secondary phase above 700 ºC, likely due to the metastable nature of the composition below approximately 900 ºC in bulk. Further, at even higher temperatures, 1100 ºC, the film undergoes a dewetting process, separating from the substrate and forming islands on the surface.

Following the relatively low temperature failure of this system, an extreme temperature stable system was produced by utilizing a heterostructure consisting of perovskite $BaZr_{0.5}Hf_{0.5}O_3$ and rocksalt MgO, capable of enduring 1100 ºC in an oxidizing environment with negligible changes in important functional properties. This pairing was designed to avoid typical thermal instabilities in these materials, such as grain growth, interlayer mixing and oxidation. The stability of this combination has been demonstrated using XRD, STEM and optical characterization.

This photonic crystal demonstrated a significant improvement in spectral control (TPV efficiency) when paired with the leading bulk thermal emitter, resulting in a 10% improvement, relative to the prior state-of-the-art value. However, we note that the filtering efficacy of our photonic crystal is significantly reduced from a perfect model.

Based on this, we realize that the films in our photonic crystal are polycrystalline as revealed by XRD due to strain relaxation and the presence of complex defect structures. This motivated a further study of the atypical failure mechanism of the $BaZr_{0.5}Hf_{0.5}O_3$/MgO system.

Rather than failing by grain growth, intermixing or oxidation, the $BaZr_{0.5}Hf_{0.5}O_3$/MgO system is observed to fail through the loss of Ba from the films, resulting in the formation of an HfO_2-based secondary phase. This loss occurs preferentially at the complex defects observed in the film. As such, these defects act as the limiting factor for the thermal stability of the heterostructure. We hypothesized that these defects form as a result of strain relaxation in the $BaZr_{0.5}Hf_{0.5}O_3$ phase, resulting in the formation of islands that transition into these complex structures with further deposition.

The presence of MgO and (Hf, Zr)O_2 following a 1000 ºC in-vacuo anneal in an $\sim$ 20-50 nm thick sample indicates the incredible stability of these phases.

Beyond the optical properties of HfO_2[48, 213], in recent years, doped HfO_2 materials, including Si- and Zr-doped, have been shown to have impressive ferroelectric properties[268–270].

CHAPTER 5

Examining Fatigue Behavior in Ferroelectric Thin Films

The work in this chapter is largely based on our submitted manuscript 'M. Webb[†], T. Chiang[†], et al. Conductive Filament Formation in the Failure of $Hf_{0.5}Zr_{0.5}O_2$ Ferroelectric Capacitors (2024)'.

5.1 Background: ferroelectric materials

A ferroelectric is a dielectric material that has a switchable and permanent polarization, that remains even after the removal of the electric field[271]. For this to happen the material must be non-centrosymmetric. While ferroelectricity was first reported in 1921 [272], it was only in 2000, that the first commercial ferroelectric memory was implemented in the Sony PS2 [273, 274]. Over time, the number of reports of ferroelectrics has increased exponentially, which is illustrated in **Figure 5.1**.

Modern ferroelectric materials show many promising properties for next-generation logic and memory devices, replacing existing charge based materials. The switchable non-volatile states allow for information to be stored as polarization and originate from a unique free energy landscape. Compared to existing complementary metal oxide semiconductor (CMOS), NAND, and dynamic random access memory (DRAM) systems, ferroelectric devices can offer improved bit stability, reduced power dissipation and scalability[275–279].

As ferroelectricity can only be realized in a non-centrosymmetric crystal structure, ferroelectricity is an uncommon material property, and historically was only observed in crystals with complex structures, like perovskites. Integrating these materials into a conventional semiconductor manufacturing process has proved troublesome, primarily due to the limited thermal budget used in the semiconductor industry and the high deposition temperature of many perovskite

[†]These authors contributed equally.

ferroelectrics[280–282]. Additionally, there is a difficulty maintaining ferroelectric properties in thin films due to the depolarization field, an internal field that occurs as a result of the polarization of the ferroelectric[283, 284]. Because of these factors, there has been little utilization of ferroelectric-based devices[277].

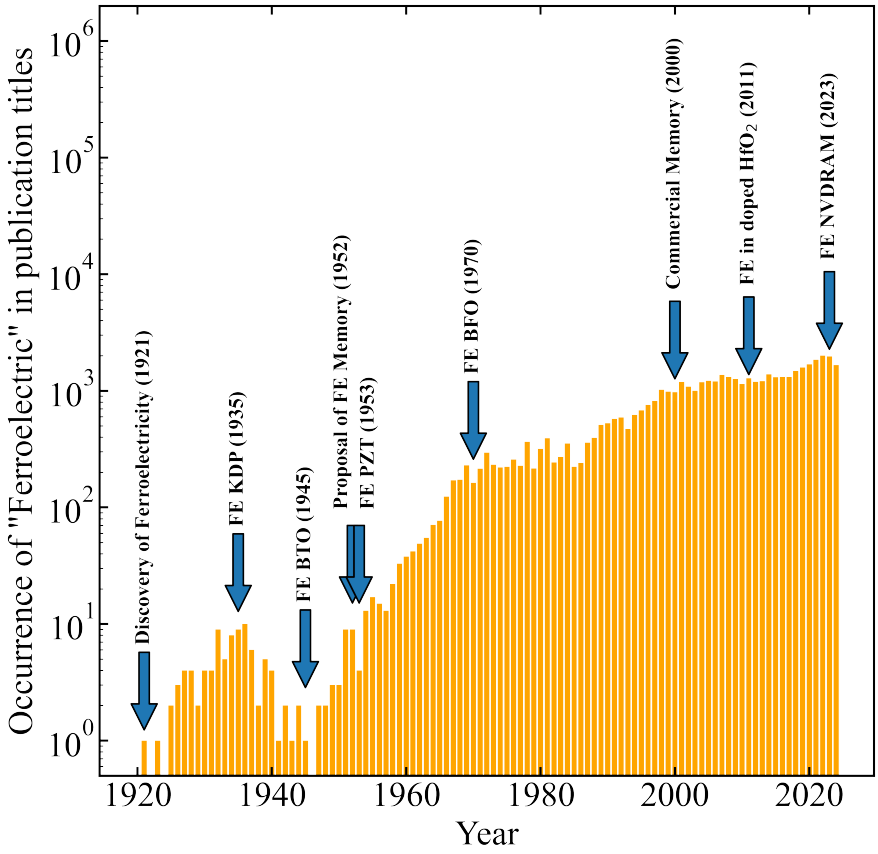


Figure 5.1: Occurrences of the term “ferroelectric” in publication titles on web of science[285]. Specific dates are identified from the relevant reports[268, 272–274, 279, 286–291]. Prior to 1945, the term ferroelectric was substituted for piezoelectric, as ferroelectric was not commonly used during this time period.

With the discovery of ferroelectricity in doped HfO_2[268], it has been considered a promising material for integration into devices[292]. This is, in part, because HfO_2 has been used in certain CMOS processes since 2007 in high-k metal gate technology[277, 293, 294]. Although the first HfO_2-based ferroelectric, was Si-doped HfO_2[268], the most exciting is $Hf_{0.5}Zr_{0.5}O_2$[270], which is suitable for integration into ferroelectric devices in many ways. Besides the CMOS compatibility, a result of the low temperature, highly conformal, depositions achieved with ALD[270, 295–298], $Hf_{0.5}Zr_{0.5}O_2$ also demonstrates a large polarization, and robust ferroelectricity in extremely thin films (below 5 nm)[299–302].

All of this solidifies $Hf_{0.5}Zr_{0.5}O_2$ as a promising ferroelectric material in addition to the benefits of scalability and low power consumption[303]. That is not to say that the integration of $Hf_{0.5}Zr_{0.5}O_2$ is without challenges. The large fields required to switch the polarization state in $Hf_{0.5}Zr_{0.5}O_2$ films and difficulty identifying the correct phase (only the orthorhombic phase can be ferroelectric) following deposition are still challenges that must be overcome[304, 305]. These coercive fields (> 1 V nm^{-1}) contribute an energy comparable to over 2000 K, illustrating how extreme these conditions are, and hence how close the films are to dielectric breakdown (**Figure 1.1**).

Many devices that utilize ferroelectric films are subjected to extreme electric fields, (epitaxial) strain and field-cycling. As such, studying the reliability of these ferroelectric films is a necessity. Common parameters that define the reliability of a ferroelectric device are the wake-up effect, retention and fatigue based failure, all of which can be limiting factors for the implementation of $Hf_{0.5}Zr_{0.5}O_2$ in non-volatile memory devices[306]. In some $Hf_{0.5}Zr_{0.5}O_2$-based memory devices, wake-up effect can be a major issue, for the first $\sim$ 1000 cycles, a low remnant polarization is exhibited by the film. It has been suggested that wake-up occurs in HfO_2-based ferroelectrics due to pinning of ferroelectric domains and phase transformation between the monoclinic to orthorhombic phases[307].

The performance of ferroelectrics under extreme cycling has been extensively studied at room temperature, primarily with a focus on improving the behavior through electrode selection and by changing the processing. Despite this, the underlying mechanisms of fatigue failure under extreme field and cycling are a topic of much contention, with many mechanisms being reported[308–312]. It is likely that the electrode choice and processing have a significant influence on the failure mechanism that occurs for a given $Hf_{0.5}Zr_{0.5}O_2$ film. One proposed failure mechanism is a phase transformation from the ferroelectric polar orthorhombic phase to a non-polar phase, such as the monoclinic phase. This transformation would cause a gradual decrease in polarization during cycling as the percentage of the material that is switching is decreased[313, 314]. Another proposed failure mechanism for an observed decrease in polarization is charge trapping via oxygen vacancies. These vacancies become pinned at interfaces, or at ferroelectric domain boundaries, preventing the switching of these domains and thus reducing the total switching polarization[315–318]. A third proposed failure mechanism is the formation of a conductive filament[319], similar to what is commonly observed in HfO_2-based memristor devices[320, 321]. However, unlike the memristor conductive filaments, which form under a direct current (DC) bias, the filaments in ferroelectric materials are expected to be a result of alternating current (AC) cycling, potentially as the result of lateral movement. The movement of charged oxygen vacancies and details on filament formation kinetics are described in **Appendix D**.

Despite these reports of different failure mechanisms, which depend on various processing factors, such as deposition and post-deposition treatments, there has been limited evidence for the formation of conductive filaments as the failure mechanism, despite the prevalence of filament formation in HfO_2 resistive switching devices[322, 323].

In this chapter we present a systematic study, with evidence for the formation of conductive filaments as the failure mechanism for $W/Hf_{0.5}Zr_{0.5}O_2/W$ ferroelectric capacitor devices. These devices are investigated as a function of temperature and device size, to enable evaluation of the mechanism of filamentary formation.

5.2 Fabrication and structural characterization of $Hf_{0.5}Zr_{0.5}O_2$

Our samples consist of $\sim$ 10 nm thick films of $Hf_{0.5}Zr_{0.5}O_2$ grown on a 50 nm thick W back electrode on a Si (001) substrate and topped with a 20 nm thick W top electrode.

Although ferroelectricity was initially discovered in $Hf_{0.5}Zr_{0.5}O_2$ grown on TiN[270], it has been shown that for $Hf_{0.5}Zr_{0.5}O_2$, W metal electrodes can be a beneficial choice, due to potential enhancement of polarization, a reduction of the wake-up effect and the existing use of W metal in the semiconductor industry, along with its CMOS compatibility[324–328].

$W/Hf_{0.5}Zr_{0.5}O_2/W$ devices were prepared following previously published procedures[311]. First, DC magnetron sputtering was used to deposit 50 nm tungsten onto a (001)-oriented silicon substrate using a custom sputter system equipped with a Meivac MAK 50.4 mm diameter sputter gun. A 3.3 W cm^{-2} sputter power density and 5 mTorr argon processing gas pressure controlled by an Alicat Scientific mass flow controller and a Meivac conductance flow valve were used. An Oxford FlexAL II plasma-enhanced ALD instrument was used to then prepare $Hf_{0.5}Zr_{0.5}O_2$ with tetrakis(ethylmethylamido)hafnium (TEMA-Hf) and tetrakis(ethylmethylamido)zirconium (TEMA-Zr) precursors for Hf and Zr, respectively. A 3:2 cycle ratio was used in 16 supercycles to produce an $Hf_{0.5}Zr_{0.5}O_2$ layer of 9.6 nm thickness. Plasma powers of 250 and 300 W were used with oxygen gas as the oxygen precursor for the HfO_2 and ZrO_2 layers, respectively. The substrate temperature was 260 ºC and a 90 s purge was used following each cation precursor dose. The general ALD process has been described in detail in **Section 2.3.2**. A 20 nm thick W layer was then deposited as the top electrode using the same parameters as the bottom electrode. Devices were annealed in an Allwin AccuThermo AW 610 rapid thermal annealer at 600 ºC in an N_2 atmosphere for 30 seconds with a heating ramp rate of 50 ºC s^{-1}.

The $Hf_{0.5}Zr_{0.5}O_2$ sample was characterized using GIXRD (**Figure 5.2(a)**), which confirms the absence of the monoclinic non-polar $Hf_{0.5}Zr_{0.5}O_2$ phase[329]. To measure the phase constitution

in the $Hf_{0.5}Zr_{0.5}O_2$ films, GIXRD was performed using a Rigaku Smartlab with a Cu Kα radiation source and a 0.7º incidence angle. The LIPRAS software package was then used to fit the pattern using Pearson VII peak shapes to determine phase fractions[330]. XRR was utilized to measure thickness of the $Hf_{0.5}Zr_{0.5}O_2$ films using an Empyrean X-Ray diffractometer with a Cu Kα radiation source. Patterns were fit using GSAS-II software package[331].

A technique, known as AFM can used to evaluate the surface topography of thin films, by measuring the deflection of a laser off the back of a thin tipped cantilever. The microstructure of our $Hf_{0.5}Zr_{0.5}O_2$ film was assessed using AFM with an Asylum Research Cypher-S instrument in AC mode off tip resonance. A BudgetSensors Tap300Al-G cantilever was used (40 N/m force constant, 300 kHz resonance frequency). The Heyn linear intercept method was used to measure average feature size[332]. AFM reveals an average lateral feature size (grain size) of $\sim$ 25 nm diameter following a rapid thermal anneal (**Figure 5.2(b)**). Due to the similarity of many the XRD peaks for $Hf_{0.5}Zr_{0.5}O_2$, it is not possible to confirm the presence of the ferroelectric phase from XRD alone.

The easiest way to confirm that the sample is ferroelectric is to produce a ferroelectric hysteresis loop by using a triangular voltage profile at low (quasistatic) frequencies. This is shown in **Figure 5.2(c)**. The samples were prepared using e-beam and optical lithography with an Ar ion mill etch to obtain a ferroelectric capacitor pillar (diameter spanning 0.4-10 μm), which was then encapsulated in an insulator and capped with a Ti/Au metal for probe contact. This is done in such a way to provide appropriate back, top and side electrodes for a radio frequency probe measurement configuration. This device configuration for this measurement and the radio frequency (RF) measurements that follow are shown in **Figure 5.2(d)**. The pseudo-DC polarization (measured at 100 kHz using a Radiant Precision Multiferroic II) versus electric field response of the $Hf_{0.5}Zr_{0.5}O_2$ shown in **Figure 5.2(c)** reveals a typical ferroelectric hysteresis loop, with a remanent polarization of $\sim$ 20 μC cm^{-2}.

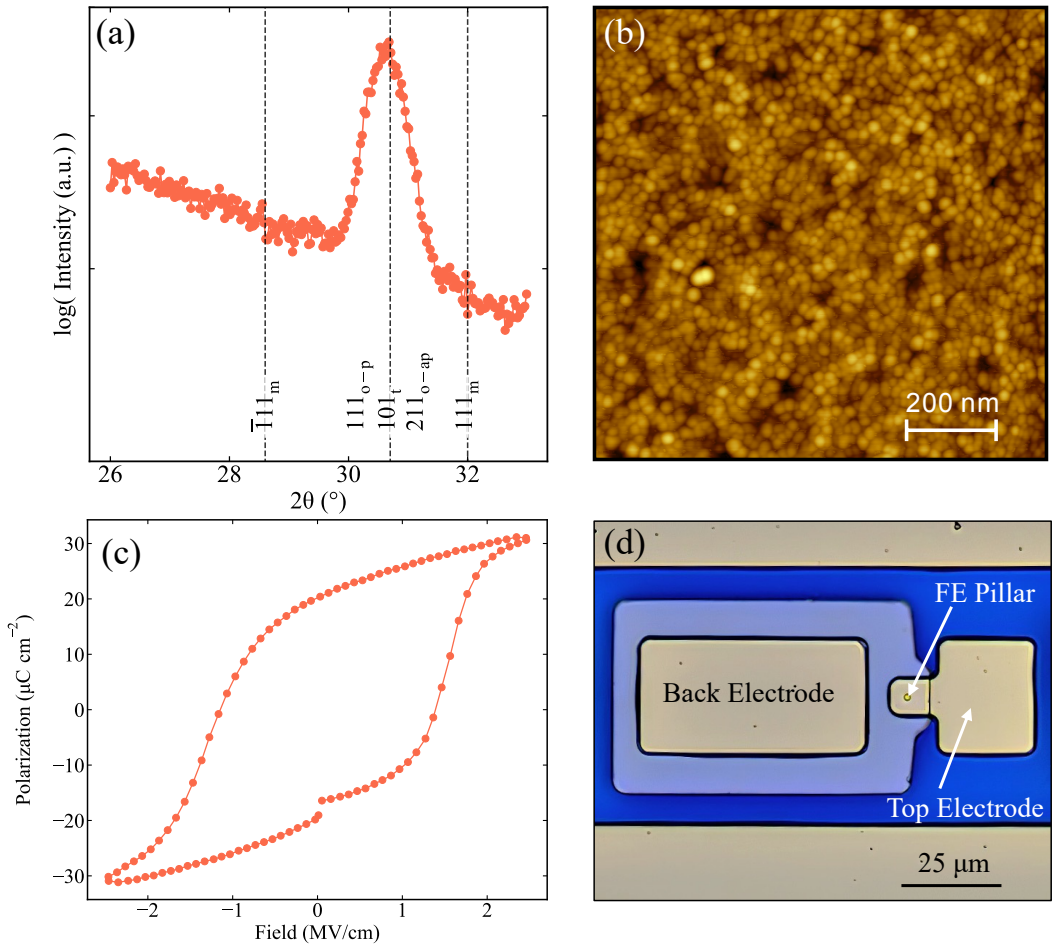


Figure 5.2: (a) GIXRD pattern of Si/W/$Hf_{0.5}Zr_{0.5}O_2$/W device stacks with a thickness of $\sim$ 10 nm. The dashed lines indicate the $\bar{1}11_m$ and 111_m reflections of the monoclinic $Hf_{0.5}Zr_{0.5}O_2$ phase and the non-equilibrium $Hf_{0.5}Zr_{0.5}O_2$ phases, namely the $111_{(o-p)}$ polar orthorhombic, 101_t tetragonal and $211_{(o-ap)}$ anti-polar orthorhombic phases. (b) 1×1 μm area AFM topography of $Hf_{0.5}Zr_{0.5}O_2$ after crystallization and removal of the top electrode, showing an average grain size of 26.4 ± 0.2 nm and a RMS roughness of 1.1 nm. (c) $Hf_{0.5}Zr_{0.5}O_2$ ferroelectric loop measured at 100 kHz. (d) Through-microscope photograph of the electrode configuration of $Hf_{0.5}Zr_{0.5}O_2$ nanodevice following ion milling to form a ferroelectric pillar under a larger top electrode for contacting with RF probes.

5.3 Cycling-limited stability of $Hf_{0.5}Zr_{0.5}O_2$

To understand the stability of the W/$Hf_{0.5}Zr_{0.5}O_2$/W structure, and its failure mechanism under fatigue, it is necessary to cycle the devices with extreme applied electric fields.

Endurance cycling was performed using the circuit configuration and pulse sequences shown in **Figure 5.3(a)**. A Keysight 33600A waveform generator and a 13 GHz capable Keysight Infiniium UXR0134A real-time oscilloscope were used to source the pulse sequence and measure the current response of the ferroelectric device respectively. The same setup was used for post-failure characterization. For thermal characterization, a heating stage with a Eurotherm nanodec controller was used.

The read/write pulses in **Figure 5.3(a)** were selected to better mimic the operational speeds of memory devices[279]. The circuit configuration utilizing the pulse generator and the oscilloscope, with the ferroelectric shown as a variable capacitor, are also shown in **Figure 5.3(a)**. The 10 ns, high duty cycle ($\sim$ 18%) dual write pulse (writes to the positive polarization and then the negative polarization, resulting in a change of $2P_r$) illustrates the potential for achieving high switching speeds in $Hf_{0.5}Zr_{0.5}O_2$-based ferroelectric memory. To accurately measure the polarization after a significant number of cumulative cycles, a longer read pulse is used. These read steps are an important method of evaluating the evolution of polarization with cycling, as a degradation in polarization is a characteristic symptom of several $Hf_{0.5}Zr_{0.5}O_2$ ferroelectric device failure modes. The evolution of polarization with cycling for our devices are shown as a function of device size and temperature in **Figure 5.3(b)**, while the number of cumulative cycles to failure are shown as a function of temperature in **Figure 5.3(c)**.

These measurements were conducted as a function of ferroelectric area and temperature to understand the effects of these variables upon the rate of failure. Additionally, measuring the temperature dependence allows for evaluation of diffusion based failure modes. Device diameters varied from 0.4-10 µm and measurements were taken every 20 ºC from 30-110 ºC. As every device was cycled until failure, a new device of a given size was used for each temperature. Furthermore, these elevated temperatures are representative of the operational temperatures typical in electronic devices[333].

In our W/$Hf_{0.5}Zr_{0.5}O_2$/W structures, we observe no polarization degradation during cycling, suggesting that neither ferroelectric domain pinning, nor an orthorhombic to monoclinic phase transformation are occurring as a result of cycling[313, 314]. Instead, we observe a sudden failure after applying an electric field for up to 10^9 cumulative cycles, following a slight increase in remanent polarization, possibly a result of a slight wake-up effect. Interestingly, when compared to literature, this is noted to be a relatively small wake-up effect, possibly a result of the W elec-

trodes, or an electric field driven transformation[334–336]. Achieving $> 10^8$ cycles at 110 ºC (in small devices) demonstrates the industry-applicable high stability and scalability when utilizing ferroelectric-based memory devices.

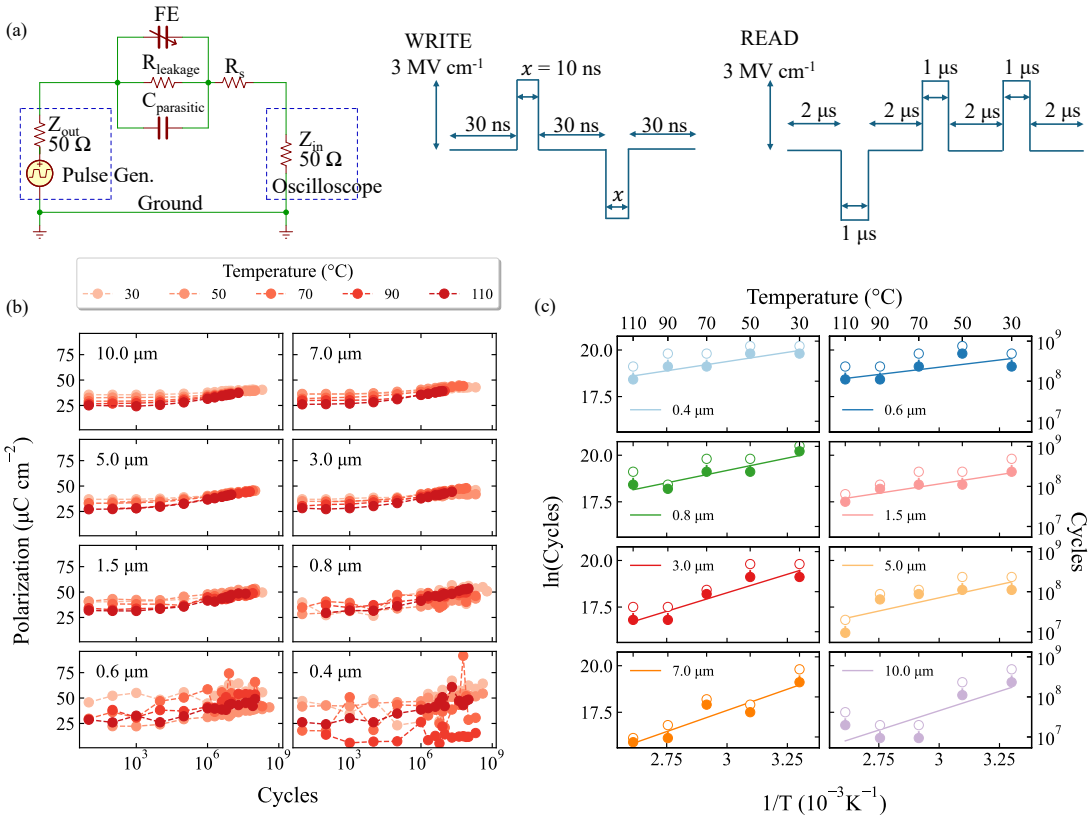


Figure 5.3: (a) Circuit design illustrating the use of a pulse generator and oscilloscope to achieve RF measurements, FE represents the ferroelectric devices, which can be considered a variable capacitor. Also shown are the "write" pulse, used to rapidly cycle the ferroelectric without recording polarization at a high duty cycle ($\sim$ 18%), and the slower "read" pulse, used to record the polarization of the ferroelectric device after a significant number of cycles. These PUND-like pulses ensure that the device is reset prior to polarization measurement (2 P_r measurement). (b) Polarization ($2P_r$) evolution under an applied field of 3 MV cm^{-1} with cycling up to nearly 10^9 full cycles shown for device diameters of 0.4 to 10 µm. An increase in $2P_r$ is observed before a sudden failure occurs. (c) Cumulative cycle count at failure of $Hf_{0.5}Zr_{0.5}O_2$ device. Due to the distribution of "read" pulses, failure occurred at an unknown cycle between the filled and unfilled data points. Data is shown as ln(Cycles) vs inverse temperature to allow for a linear fit based on an Arrhenius equation (**Appendix D**).

As we are observing a sudden failure, without a decrease in polarization, the most likely failure mechanism to be responsible is formation of conductive filaments. While these filaments are known to form under the application of DC voltage in memristive switching devices[322, 323], the

formation of filaments is somewhat different under the application of AC voltage. Some of these differences are highlighted in **Figure 5.4**. Under an alternating bias, the oxygen vacancies needed to form a filament are not expected to accumulate at either electrode. However, as the applied electric field is enormous, and out-of-plane, it is assumed that the formation of conductive filaments are limited by the rate of in-plane (lateral) motion of the oxygen vacancies in a random walk process. As such, the cycling behavior can be fit with a generalized inverse Arrhenius equation (**Eq. 5.1**, which is equivalent to **Eq. D.7**, the derivation of which is described in **Appendix D**).

$$ln(N) = A + \frac{E'_A}{k_B T} \tag{5.1}$$

N is the number of cycles to failure, E'_A is the field-modulated diffusion barrier (or activation energy), k_B is the Boltzmann constant, T is the temperature, and A is a constant that incorporates other terms such as diffusion length and the proportionality constant relating cycles and time. The field-modulated activation energy barrier can be related to the thermal activation energy barrier using the energy of a charged particle under the application of an electric field, given by **Eq. 5.2**.

$$E'_A = E_A + z\phi \tag{5.2}$$

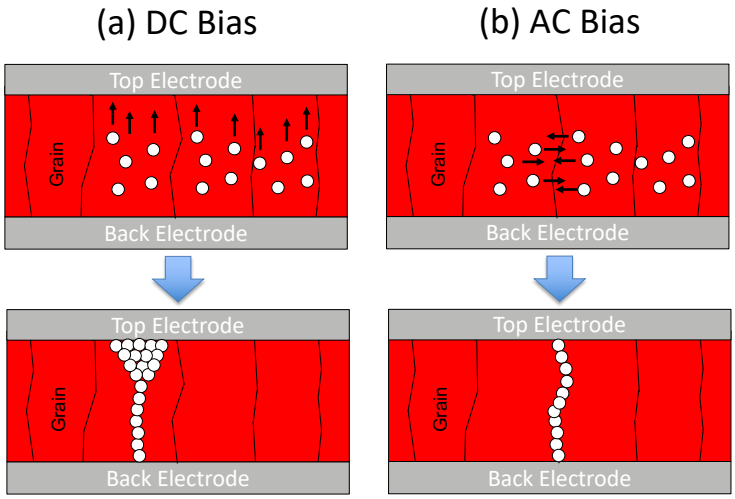


Figure 5.4: (a) Under the application of a DC voltage, oxygen vacancies move in the direction of the applied bias, accumulating at the ferroelectric-electrode interface. (b) Under the application of a AC voltage, the oxygen vacancies do not move toward either electrode. Instead, the applied field lowers the diffusion barrier, resulting in increased lateral movement, following a random walk. This can eventually lead to oxygen vacancies accumulating and becoming pinned at the grain boundaries, forming a conductive filament.

From the fit in **Figure 5.3(c)**, a field-modulated activation energy of $E'_A \approx$ 150-400 meV is obtained, which is much less than the reported thermal self-diffusion activation energy (E_A) of 1.02 $\pm$ 0.24 eV.[337]. It is clear that an electric field will lower the activation barrier for motion in the direction of the field by acting as a force on the charged particle. However, the atomic sites for diffusion hopping rarely lie in a straight line perfectly parallel to the applied field, especially in the case of a polycrystalline material such as this which contains many different crystal orientations. This means there will always be a lateral component to the field-enhanced diffusion, hence we observe a lowering of the activation energy, even when considering lateral diffusion to form a conductive filament. The activation energy and the field-modified activation energy can be related by the energy of a particle with charge z, in an electric potential field of ϕ (**Eq. 5.3**). For this system, this corresponds to an average vacancy charge state equivalent to less than a singly-charged vacancy, possibly due to the clustering of vacancies.

$$E'_A = E_A + z\phi \tag{5.3}$$

While it has been demonstrated the formation of conductive filaments can also occur as a result of heating[338] rather than the motion of oxygen vacancies under an applied electric field, we do not believe this is the case in this system. As the leakage current in our system is very low and given the 9 MHz frequency of the write pulse, dielectric heating is likely to be far larger than Joule heating, which is likely negligible. The dielectric heating is defined below in **Eq. 5.4**[339], where $P_{density}$ is the power per unit volume, ω is the angular frequency of the field, ϵ_0 is the permittivity of free space, ϵ'' is the imaginary part of the relative permittivity, and $|E|$ is the magnitude of the electric field.

$$P_{density} = \omega\epsilon_0\epsilon''|E|^2 \tag{5.4}$$

By multiplying by the volume of the dielectric material across which the field is applied and the length of each pulse, it is possible to estimate the thermal energy generated per cycle. Using a field frequency of 9 MHz, a 1 µm diameter device, with a 3 MV cm^{-1} field across a 10 nm device and $\epsilon'' \approx 5$ [340], we calculate an energy of $\sim 2 \times 10^{-13}$ J each cycle. Using equation **Eq. 5.5**[341] we can estimate the heat dissipation through the W electrode and Si substrate, which act as heat sinks, where κ is the thermal conductivity, A is the area of the heat sink material in contact with the heating source, d is the thickness and ΔT is the drop in temperature.

$$P_{thermal} = \frac{\kappa A \Delta T}{d} \tag{5.5}$$

Using $\kappa \approx 140$ [342], the area of the ferroelectric 1 μm device, and the substrate thickness of 500 μm with a temperature drop of 1 ℃, we estimate the removal of $\sim 1 \times 10^{-13}$ J each cycle, suggesting that the temperature change as a result of dielectric heating will be negligible due to the large Si heat sink available. However, there is still another source of heating that must be considered. This source is intrinsic losses within the ferroelectric material upon switching, due to mechanisms such as piezoelectric lattice deformations[64]. This contribution can be calculated by the area inside the ferroelectric polarization-field hysteresis loop. Integrating the ferroelectric loop in **Figure 5.2**, gives an energy dissipation of $\sim$ 113 J cm^{-3} per cycle. For a 10 nm thick device with a ferroelectric pillar of 1 μm diameter, this corresponds to $\sim 9 \times 10^{-13}$ J each cycle. Factoring in this heat contribution in addition to the dielectric heating, results in a necessary temperature difference of $\sim$ 11 ℃ across the Si substrate to compensate for the heat generation. Considering a rise of 11 ℃, or 11 K, in a temperature range of 300-380 K is less than a 5% discrepancy from our set temperatures, the impact of this additional heat is likely negligible. A temperature rise of this magnitude is clearly insufficient to result in the formation of a conductive filament.

The area dependence of cycling endurance is shown more clearly in **Figure 5.5**. From this, it is clear that failure appears to occur more quickly in the devices with the larger ferroelectric pillars. The slight area dependence indicates that the failure is somewhat dependent on device size, indicating a failure mechanism that is a stochastic mechanism. Generally, it is expected that more defects will be present in a larger ferroelectric device, possibly introduced during ALD deposition, during device fabrication or during cycling. With a larger number of defects present, using a random walk model, there is an increased likelihood of formation of a filament, which should require a fixed number of oxygen vacancies for complete formation, dependent on only the thickness of the ferroelectric layer. However, while there does appear to be an area dependence, it is lower than expected when compared to the literature[343], which expects failure to occur orders of magnitude earlier in large devices.

The E'_A obtained from **Figure 5.3** is plotted as a function of device size in **Figure 5.6(a)**. No area dependence is expected for the field-modified activation energy, as this should be determined only by the mobility of oxygen vacancies under an applied field. Due to the large errors associated with the fitted values of E'_A, it is not clear whether or not we are observing an area dependence. However, we do observe a small negative correlation between area and number of cumulative cycles to failure.

While our analysis of the data in **Figure 5.3** has resulted in a hypothesis of a localized failure mechanism, such as formation of a conductive filament, it is important to obtain more evidence to support this observation. As such, following the failure of these ferroelectric devices, the leakage current of each device was characterized. The measured leakage currents have been reported as a

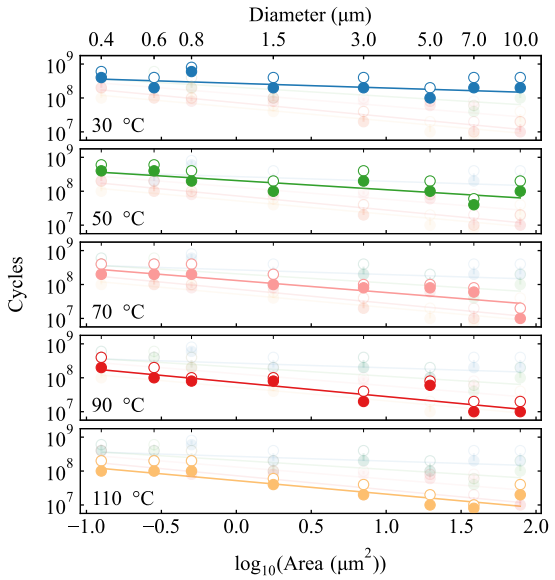


Figure 5.5: Area dependence of the cumulative cycles to failure shown in **Figure 5.3.** Failure occurred at an unknown cycle number between the filled and unfilled data points. It is observed that the number of cumulative cycles to failure depends upon both device size and temperature.

function of device size in **Figure 5.6**(b). The reported currents are large, and invariant of ferroelectric device size, supporting our hypothesis of conductive filament formation from the motion of oxygen vacancies[345]. As soon as the formation of the first conductive filament in a device is completed, it is expected that no further filaments will form, as the potential difference across the ferroelectric film is now close to zero. This results in several partially formed filaments remaining in the film. As each failed device contains one complete conducting filament, it is expected that under this mechanism, the current would not dependent upon ferroelectric device area.

We further investigate our hypothesis of filament formation, using conductive-AFM. In conductive-AFM, a current can be passed through the tip to evaluate localized conductivity. Before conducting conductive-AFM, it was necessary to remove the patterned top electrode (300 nm Au / 10 nm Ti / 20 nm W), exposing the bare ferroelectric layer. While it was not possible to observe any filaments that occurred during the failure of the $Hf_{0.5}Zr_{0.5}O_2$ device under cycling, it was possible to write conductive filaments using an applied voltage, shown in **Figure 5.6(c, d)**. We hypothesize that during this writing process, partially formed filaments are completed under the application of the DC bias from the tip. These filaments are observed to occur primarily during the edge of the electrode. We theorize that our failure to observe any pre-formed filaments is due to their location, likely right at the edge of the electrode. This theory is supported by COMSOL simulations shown in **Figure 5.7**, which shows that there is a significant field amplification ($> 20\%$).

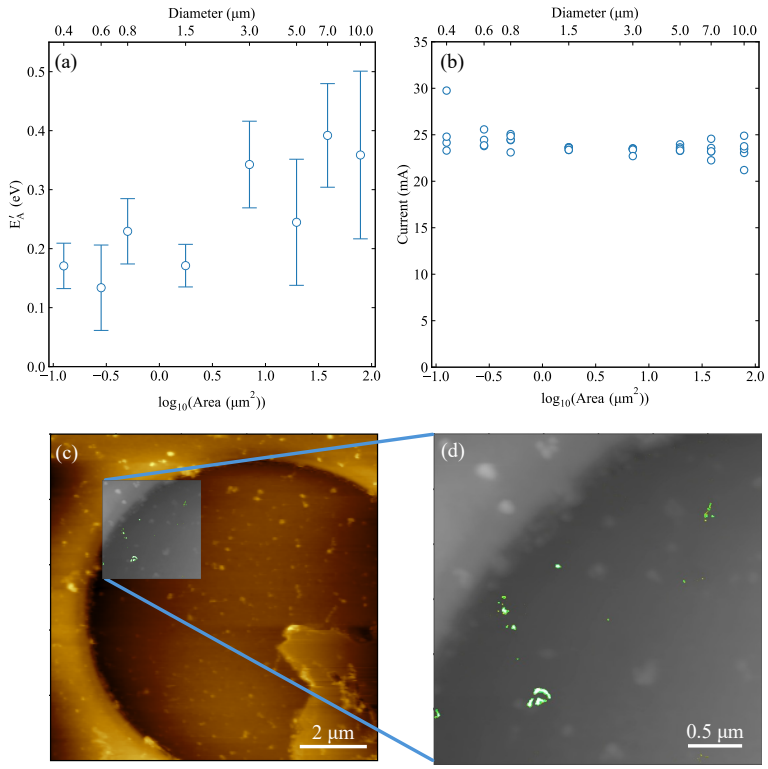


Figure 5.6: (a) Field-modulated diffusion barrier (activation energy) extracted from the fit of **Figure 5.3(c)**, demonstrating a reduction from the reported thermal diffusion value of 1.02 $\pm$ 0.24 eV [337]. (b) Measurement of leakage current in devices measured in **Figure 5.3** following failure is area independent (at a field of 3 MV cm^{-1}), suggesting a localized failure mechanism such as the conductive filaments that are observed in HfO_2-based memristive devices[321, 344]. (c) Topography of a failed $Hf_{0.5}Zr_{0.5}O_2$ device following the removal of the top electrode. (d) It was demonstrated that it is possible to write a conductive filament using a voltage applied by a conductive-AFM tip. High conductivity regions are shown in green, overlaid with the topography from (c). This image was acquired by sourcing a voltage of 1 V through the tip, operated in contact mode. Conductive filaments were written using a voltage of up to 4 V.

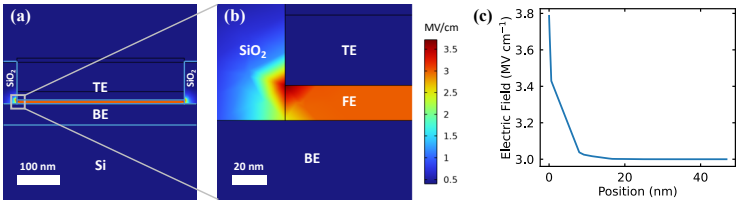


Figure 5.7: (a) Field simulation showing entire device structure, with a field of 3 MV cm^{-1} applied to the top electrode and grounding the bottom electrode. TE is the W top electrode, FE represents a uniform $Hf_{0.5}Zr_{0.5}O_2$ ferroelectric layer, and BE is the W back electrode. (b) Field simulation showing an enlarged view of the edge of the ferroelectric capacitor, exhibiting field amplification at the TE-FE-SiO_2 junction. (c) Horizontal line scan showing electric field as a function of position, starting at the left edge of the FE device (0 nm), an increase of $> 20\%$ is observed at this edge.

5.4 Conclusion: the stability of ferroelectric devices

In this chapter we have demonstrated a simple $Hf_{0.5}Zr_{0.5}O_2$based ferroelectric device, capable of maintaining a switchable polarization for over 10^8 cycles under extreme electric fields at operating temperatures typical of modern electronic devices. This has been observed through the evolution of polarization, as the ferroelectric state is cycled using a field of 3 MV cm^{-1}.

New ferroelectric materials, such as $Hf_{0.5}Zr_{0.5}O_2$, have shown high promise due to their resilience to depolarizing fields at small thicknesses, and their ability to be integrated seamlessly into semiconductor industry processes. However, the operational failure of these films is poorly understood, with several potential failure modes identified in prior studies.

We have shown evidence for the formation of a conductive filament, formed from the motion of oxygen vacancies, as the cause of failure in a W/$Hf_{0.5}Zr_{0.5}O_2$/W structure. The lack of polarization degradation during cycling indicates a failure mechanism that is not based on the pinning or transformation of the ferroelectric phase. This contradicts many prior reports of failure in $Hf_{0.5}Zr_{0.5}O_2$-based devices, suggesting that the failure mechanism may be highly dependent on processing and choice of electrode. Further evidence for a localized failure mechanism was observed, in the form of a high post-failure leakage current, the magnitude of which was independent of ferroelectric device size. Additionally, an Arrhenius dependence of breakdown cycle with temperature was revealed, indicative of a failure mechanism mediated by ionic transport, with a field-modified diffusion barrier reduced by ~ 0.8 eV, compared to the thermal diffusion barrier, under the application of a 3 MV cm^{-1} electric field.

From this work, it is clear that $Hf_{0.5}Zr_{0.5}O_2$ ferroelectric structures are highly stable despite the extremely high switching fields, with failure only occurring after many cycles. It is also clear that the phase stability and defect mobility of these structures is highly dependent on the deposition and treatment processes, and that further improvements to $Hf_{0.5}Zr_{0.5}O_2$ structures will likely be produced by processing that results in a reduction in the defect (oxygen vacancy) density in the ferroelectric layer.

CHAPTER 6

Conclusions and Suggested Future Works

An ever increasing push for higher performance has resulted in many applications subjecting materials to greater and greater extremes. Achieving materials that are stable under such conditions is difficult and requires a deeper understanding of the relationship between failure mechanisms and phase stability and defect mobility in these materials. In this work the behavior of several functional oxide materials with the potential for stability under certain extreme conditions, such as strain, temperature and electric field was investigated. The failure of each material was reported when the conditions become too severe.

In **Chapter 3**, the potential for high entropy oxide systems to exhibit many unique, tunable functional properties, stable under extreme temperatures, was discussed. It was then demonstrated that the bulk prototypical high entropy oxide, $Mg_{0.2}Co_{0.2}Ni_{0.2}Cu_{0.2}Zn_{0.2}O$ ((MgCoNiCuZn)O), was not as stable as may have been expected based on its large configurational entropy. It has been shown that above 1300 ºC, there is a significant decrease in the concentration of copper in the rocksalt phase, and above 1400 ºC, a significant decrease in the concentration of zinc is also observed. It was hypothesized that the loss of copper occurs due to a reduction in copper solubility above 1100 ºC, evident from the solubility of copper in the binary rocksalt oxides. However, solubility alone is not able to explain the loss of zinc from the system. When the copper is lost from the rocksalt phase, there is a reduction in the configurational entropy of the system, reducing the stability of zinc oxide in the unfavorable rocksalt phase, allowing the zinc to sublimate.

In **Chapter 4**, various oxide pair thin film systems with specific optical properties were evaluated at temperatures up to 1100 ºC, with the $BaZr_{0.5}Hf_{0.5}O_3$/MgO system being the most stable of those selected. It was found that films containing (MgCoNiCuZn)O fail at relatively low temperatures either as a result of intermixing, their metastable nature or dewetting. A system containing $BaZr_{0.5}Hf_{0.5}O_3$/MgO, two refractory oxides, was then investigated, achieving a, at the time, record high temperature stability in (dry) air, and a record high improvement in spectral control when paired with the leading TPV emitter. Above 1100 ºC, or in moist air, it was observed that the $BaZr_{0.5}Hf_{0.5}O_3$ phase degraded through the loss of barium and the formation of an (Hf, Zr)O_2

based secondary phase. Despite these exciting properties, it was observed that there was a degradation of optical properties when compared with an ideal model, leading to a further investigation of the film structure. This revealed that structural degradation and failure occurs preferentially at complex defect structures that form during deposition, likely as the result of strain.

In **Chapter 5**, the stability of an exciting ferroelectric material, $Hf_{0.5}Zr_{0.5}O_2$, was investigated under the application of extreme electric field cycling. The $Hf_{0.5}Zr_{0.5}O_2$ ferroelectric device was observed to be stable for over 10^8 cycles at 3 MV cm^{-1} at temperatures typical of the operating conditions of many electronic devices. Failure of this material eventually occurs due to the formation of conductive filaments from the migration of oxygen vacancies.

In the upcoming section we will discuss interesting directions that research on materials stable under extreme conditions could take, particularly in relation to the materials discussed in this thesis.

6.1 Suggested future work

6.1.1 Methods to improve the stability of (MgCoNiCuZn)O

It is undeniable that a large configurational entropy *should* contribute to an increased stability at elevated temperatures, due to Gibbs' free energy, shown in **Eq. 3.3**. Failure in the case of (MgCoNiCuZn)O can be largely attributed to the inclusion of CuO and ZnO, two oxides that do not want to be in the rocksalt structure, and thus contribute an unfavorable enthalpy and present possible solubility issues. That isn't to say that (MgCoNiCuZn)O may not still have, as of yet, unrealized applications at elevated temperatures in the range 1000-1300 ºC, where it is thermodynamically stable, or at room temperature where it is kinetically stable.

It is possible that there are a number of methods that could improve the stability of the (MgCoNiCuZn)O composition at these elevated temperatures. For example, the production of a single crystalline material, may reduce the number of fast diffusion pathways, such as grain boundaries, limiting the loss of Cu and Zn from the interior of the material. As we know that the pure rocksalt oxide (Mg, Co, Ni)O is stable at 1700 ºC, it is likely that a non-equimolar combination of MgO, CoO, NiO, CuO and ZnO, with reduced Cu and Zn concentrations, may be stable at a slightly higher temperature (than the equimolar composition), due to the lower solubility demands, and reduction in unfavorable enthalpy. We can hypothesize that any concentration observed after a two hour anneal in **Figure 3.11**, could potentially be stable at that temperature for two hours. For example, an almost equimolar composition, with 15% Cu could be stable at 1300 ºC. To verify this, it would be necessary to synthesize various compositions, such as $Mg_{0.225}Co_{0.225}Ni_{0.225}Cu_{0.1}Zn_{0.225}O$

or $Mg_{0.267}Co_{0.267}Ni_{0.267}Cu_{0.1}Zn_{0.1}O$, subject them to a similar annealing test and record the composition both before and after annealing. However, while we may expect to observe improved stability, it is important to also consider the functional properties of these oxides, as by reducing the high entropy component of the material, we are probably reducing some of the tunability and excitement of these properties. However, this may be suitable in some applications. A possible relationship between composition, stability and functionality is shown in **Figure 6.1**.

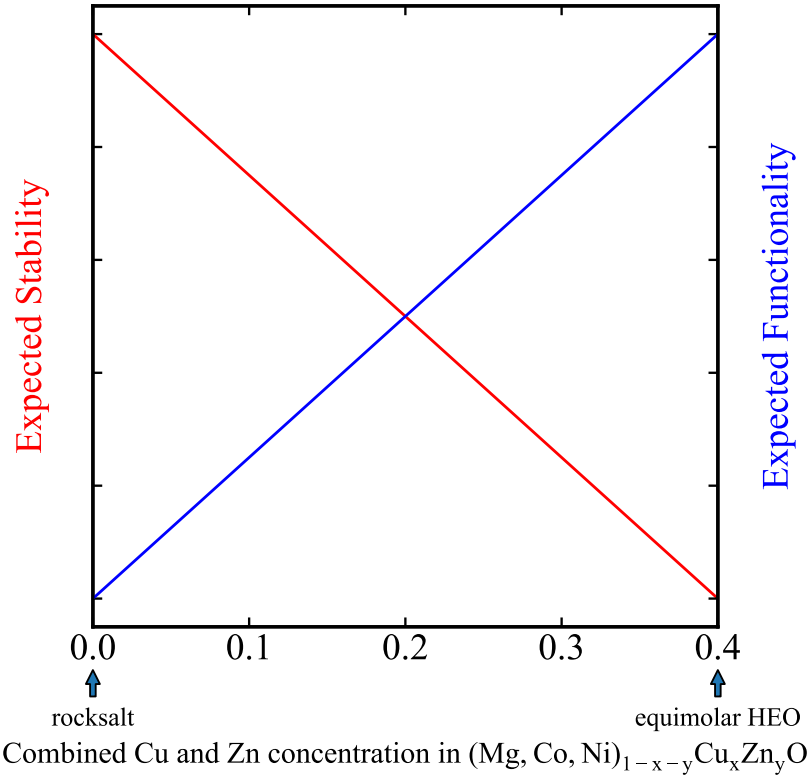


Figure 6.1: Schematic relationship between composition of high entropy oxide (MgCoNiCuZn)O and expected stability and functionality. Linear plots are shown only as a guidance and any real dependence is likely to be far more complex.

Doped compositions of (MgCoNiCuZn)O may also be more stable, due to the interaction of the various ions present. While many alloys based upon (MgCoNiCuZn)O have been reported, few have been investigated at elevated temperatures[167, 178]. Again, it would be necessary to test the effects of various dopants on the high temperature stability and functional properties of the high entropy oxide material.

6.1.2 Monostructural high entropy oxides

While high entropy rocksalt oxides have been the focus of this study, as the first report of a entropy-stabilized oxide was the rocksalt oxide, many other oxide structures have already been investigated such as fluorite, perovskite, bixbyite, pyrochlore, rutile, magnetoplumbite, garnet, and even non-oxide ceramics like carbides, silicides and nitrides[346].

We hypothesize that a monostructural oxide, that is an oxide alloy where each component forms that same stable oxide structure, for example, a perovskite phase, may be a pathway to producing a disordered structure that demonstrates stability at an even higher temperature. In a monostructural system, there are no oxides that are in a metastable structure, such as CuO and ZnO in the rocksalt structure within (MgCoNiCuZn)O. Although the perovskite phase offers less configurational entropy than a rocksalt phase, due to its reduced cation-anion ratio, ABO_3 versus the one-to-one disordered lattice to ordered oxide sub-lattice of the rocksalt structure, there are many more stable perovskite oxides than rocksalt oxides, allowing for a broader selection of oxides to select from[347]. While the lower configurational entropy could result in a reduction in stability when considering the Gibbs' free energy, it may be possible to also reduce issues with solubility and phase separation by utilizing a monostructural system.

Given what is known about the stability of bulk $BaZrO_3$ and $BaHfO_3$, we hypothesize that a high entropy perovskite based on these systems could have an excellent stability and interesting properties. Further suitable oxides to alloy these with could include $BaTiO_3$, $BaSnO_3$ and/or $BaNbO_3$ to give a composition such as $Ba(Ti_{0.2}Zr_{0.2}Nb_{0.2}Sn_{0.2}Hf_{0.2})O_3$. The lowest known melting point of these oxides is 1625 ºC for $BaTiO_3$ and while the melting temperature of $BaSnO_3$ is not known, it has a Debye temperature greater than that of $BaTiO_3$ or $BaZrO_3$, which could indicate a high melting temperature[348–350]. These oxides were selected considering Hume-Rothery considerations such as ionic radii, crystal structure and valence, however due to the enormous compositional space of high entropy oxides, down-selecting components can be difficult. If we consider selecting five component oxides from a pool of only 20 different oxides, we can compute that there are over 15000 different compositions, without even considering non-equimolar combinations. The potential of all these different combinations is to produce oxide materials capable of providing greater flexibility to meet the ever more extreme conditions demanded of today's advanced materials[165]. Despite this, finding high entropy oxides that will form without phase separation is rare, even without considering stability at extreme temperatures[153]. We propose an approach where computational methods are used to down-select high entropy monostructural oxide systems, that would then be experimentally synthesized, tested for stability and functional properties and finally compositionally optimized (**Figure 6.2**).

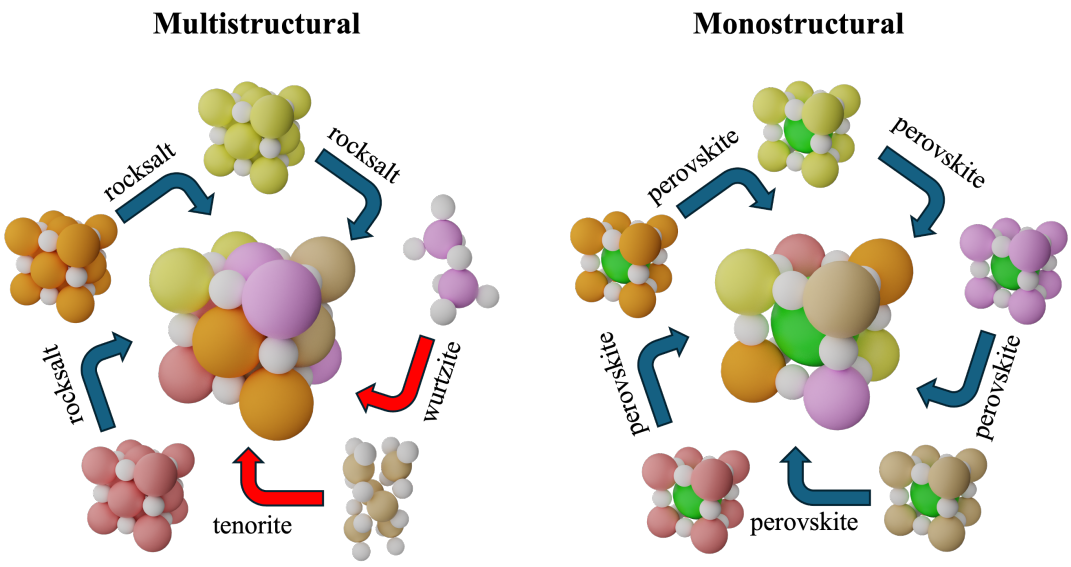


Figure 6.2: Illustration of the differences between a multistructural high entropy oxide, such as (MgCoNiCuZn)O and a monostructural oxide such as $Ba(Ti_{0.2}Zr_{0.2}Nb_{0.2}Sn_{0.2}Hf_{0.2})O_3$, a potential perovskite high entropy oxide. Note that the structures with red arrows are contributing a negative enthalpy of formation (ΔH_f) that could contribute to disrupting the stability of the high entropy material

6.1.3 Methods to improve the stability of the $BaZr_{0.5}Hf_{0.5}O_3$/MgO system

It may also be possible to improve the stability of the $BaZr_{0.5}Hf_{0.5}O_3$/MgO photonic crystal. It is difficult to prevent the loss of Ba due to the reaction with water at elevated temperatures, or the isolated loss of Ba in-vacuo. However, we hypothesize that it is possible to improve the stability of the structure by reducing the formation of the complex strain-related defect structures, as failure occurs preferentially at these sites. Theoretically, by altering the $BaZr_{0.5}Hf_{0.5}O_3$ composition it may be possible to improve the lattice match the MgO substrate. The calculated lattice parameters from Materials Project of a_{BaZrO_3} = 4.256 Å, a_{BaHfO_3} = 4.204 Å, and a_{MgO} = 4.256 Å, reveal that the best composition would be pure $BaZrO_3$[244, 351–353]. However, if we consider instead the experimentally observed lattice parameters for MgO, $BaHfO_3$ and $BaZrO_3$, we find that MgO has a larger lattice parameter than any combinations of the two perovskites[238, 239, 241, 243]. While it could be possible to instead reduce the strain during deposition by tuning the substrate temperature, in this case, both the lattice parameter and the CTE of $BaZrO_3$ are lower than that of MgO, so increasing the growth temperature only increases the strain during deposition. Lowering the temperature would reduce the strain somewhat, however low temperature growths of perovskite materials are uncommon, often requiring a unique approach, such as the use of seed layers or high pressure annealing and as such may not be suitable for this complex system[354, 355].

While pure $BaZrO_3$ offers a better lattice match, it is such a small difference that an improvement in stability may not be observed. We propose instead replacing $BaHfO_3$ with a perovskite possessing a larger unit cell. However, there is a very limited selection of stable perovskite materials with a lattice parameter that is larger than MgO. With a reported experimental lattice parameter of 4.40 Å, $BaUO_3$ is one of the few cubic perovskites that $BaZrO_3$ could be alloyed with to produce a lattice parameter equal to that of MgO, in addition to a melting temperature over 2000 ºC and can be synthesized using UO_2 and $BaCO_3$[356]. An additional advantage is that the CTE of $BaUO_3$ is closer to that of MgO, meaning there would be less thermal strain at extreme temperatures.

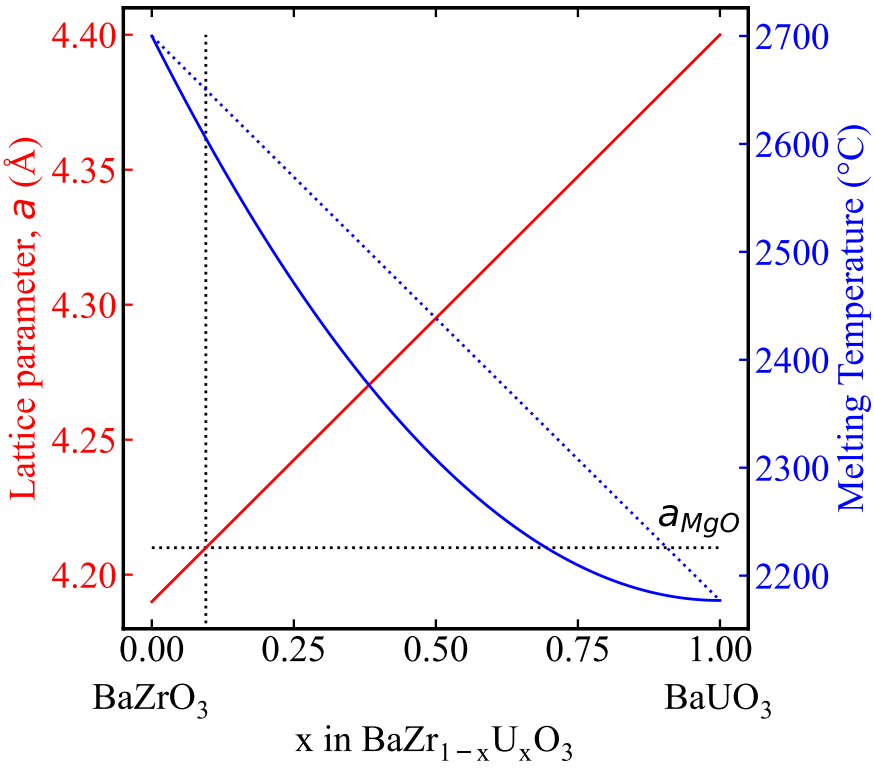


Figure 6.3: Illustration of the effect of doping $BaZrO_3$ with $BaUO_3$ on lattice parameter and melting temperature. Note that while a Vegard's law approach is used for composition, temperature is only illustrated schematically based on typical solidus lines observed for many fully miscible phase diagrams.

While this melting temperature is significantly lower than that of $BaZrO_3$ or $BaHfO_3$, we observe from **Figure 6.3**, that only a small proportion of $BaUO_3$ is needed to match the lattice parameter of MgO, and therefore the melting temperature is not significantly reduced. To test this approach, it would be necessary to reproduce the measurements done on the $BaZr_{0.5}Hf_{0.5}O_3$/MgO systems but with a $BaZr_{0.9}U_{0.1}O_3$/MgO system. Investigating the effect of U doping upon the optical properties would also be an important aspect.

6.1.4 Low lattice mismatch functional oxide pairs

We hypothesize that a different oxide pair with a lower lattice misfit strain or a better match in CTE may be capable of achieving a greater stability, while maintaining the necessary optical properties. A lower coefficient of thermal expansion would result in less thermal strain at extreme temperatures, which are likely a contributor to material failure. Some work towards selecting an oxide pair with better lattice matching was conducted in **Appendix C**. In this process, Materials Project was searched for substrates with a high melting point, and compatible pairs with low lattice misfit[244]. The process and results are summarized in **Figure C.1**, with the steps being:

1. Choose an oxide substrate
2. Query the materials project database
3. Identify low strain compatible oxide pairs
4. Evaluate for high temperature nanophotonics
5. Survey available experimental data

Besides $MgO/BaZrO_3$, other systems such as $KTaO_3/MgAl_2O_4$ were identified as lower mismatch systems with comparable or enhanced refractive index contrast. However, at this time, all of this work has been to computationally select appropriate oxide systems. To truly test our hypothesis that a lower strain system would offer increased stability, it would be essential to fabricate several of these systems to measure experimentally. If these systems could be successfully fabricated then the next step would be to measure the stability of the system in a similar manner as the $BaZr_{0.5}Hf_{0.5}O_3/MgO$ system, in a superlattice structure, annealed in several different atmospheres such as air, dry air and N_2.

APPENDIX A

Calculations of Wurtzite ZnO Solubility in Rocksalt Oxides, MgO, NiO and CoO

The work below was reproduced from the work conducted by my co-authors at Penn State University in the supplementary information of our work 'M. Webb, et al. High temperature stability of entropy-stabilized oxide $(MgCoNiCuZn)_{0.2}O$ in air. *Appl. Phys. Lett.* (2024)'[150].

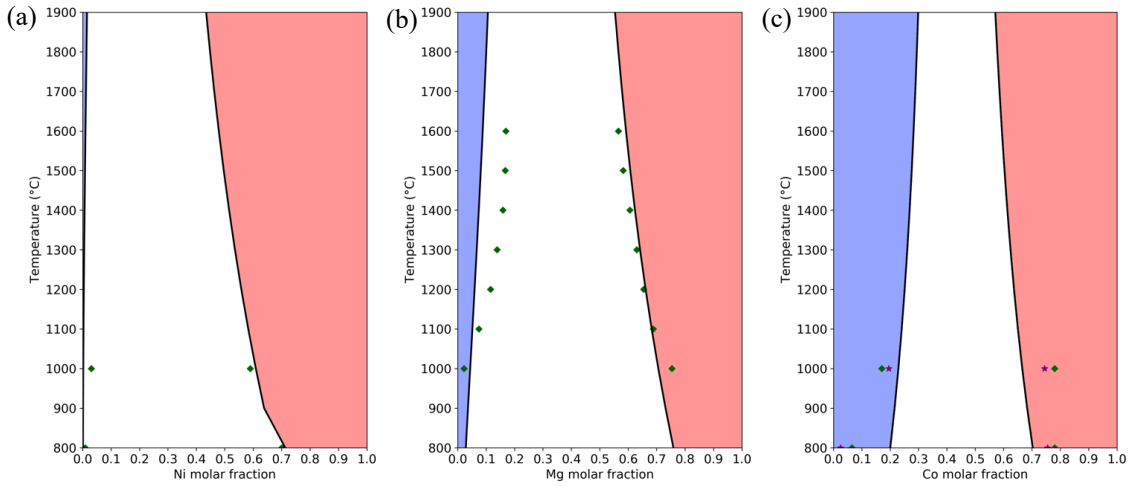


Figure A.1: Computed binary phase diagrams for ZnO-rocksalt oxide. (a) ZnO-NiO, (b) ZnO-MgO, (c) ZnO-CoO. This is shown along with the relevant experimental data plotted in **Figure 3.3**.

The methods for computing the phase diagrams of **Figure A.1** are described below:

Density Functional Theory (DFT) calculations were carried out using version 6.4.2 of the Vienna Ab initio Simulation Package VASP software[357], within the spin-polarized generalized gradient approximation (GGA) and the Perdew-Burke-Ernzerhof (PBE) parametrization[358]. Hubbard U corrections were applied to the $3d$-orbitals of Co (U = 3.32 eV) and Ni (U = 6.2 eV) in oxide compounds, and formation energies were calculated following the methodology employed

by the Materials Project (database release v2021.11.10)[359, 360]. Ionic cores were represented using Projector Augmented Wave (PAW) pseudopotentials[361, 362], and the energy cutoff for the plane-wave basis set was 680 eV. The Brillouin zone was sampled using a Monkhorst-Pack grid with a k-spacing of 0.22 $Å^{-1}$. Atomic configurations were relaxed at zero pressure, using a maximum force threshold of 10 meV/Å. To minimize the Pulay stress, relaxation runs were repeated until the volume change between two consecutive runs was less than 1%.

Symmetrically unique configurations of (Zn, Mg)O, (Zn, Co)O, and (Zn, Ni)O in the wurtzite and rocksalt phases were generated using the structure enumeration module[363, 364] with the Integrated Cluster Expansion Toolkit Python package[365]. Sizes up to eight formula units were initially considered, and larger sizes of ten formula units were considered in cases where few configurations relaxed into the initial phase. A total of 1,030 configurations of (Zn, Mg)O (401 wurtzite and 629 rocksalt), 641 configurations of (Zn, Co)O (401 wurtzite and 240 rocksalt), and 908 configurations of (Zn, Ni)O (333 wurtzite and 575 rocksalt) were considered in this study. Then, the mixing enthalpies, ΔH_{mix}, of these structures were calculated using **Eq. A.1**, where x is the fraction of the dopant A in the ZnO host as a decimal, E_{conf} is the energy of a configuration per formula unit, and E_{ZnO} and E_{AO} are the reference energies of ZnO and AO, respectively. Since the depth of ΔH_{mix} is on the order of -20.0 meV per formula unit, implying the existence of metastable configurations, finite-temperature effects were considered.

$$\Delta H_{mix}(x) = E_{conf} - (1-x)E_{ZnO} - xE_{AO} \tag{A.1}$$

The clustering interactions and mixing enthalpies were fitted using a cluster expansion model[365–367] to model energetics at length scales of thousands of atoms. This method uses an orthogonal basis of cluster functions to describe cluster interactions in a crystal structure as shown in **Eq. A.2**, where $\gamma_{\alpha_i}(\sigma_i)$ is an orthogonal basis function of a cluster, α, within a specific configuration, σ, and the product is calculated over all the lattice sites. The energies of the configurations are then modeled as a linear combination of the cluster functions (**Eq. A.3**), where J_α are the cluster interactions.

$$\Gamma_\alpha(\sigma) = \prod_i \gamma_{\alpha_i}(\sigma_i) \tag{A.2}$$

$$E(\sigma) = \sum_\alpha J_\alpha \Gamma_\alpha(\sigma) \tag{A.3}$$

These effective cluster interactions are extracted using a least-squares regression method. Clus-

ter sizes of doublets and triplets were considered. The cluster expansion model fits of the wurtzite phases resulted in 27, 19, and 89 nonzero effective cluster interactions for (Zn, Mg)O, (Zn, Co)O, and (Zn, Ni)O, respectively, whereas the cluster expansion model fits of the rocksalt phases resulted in 31, 55, and 55 nonzero effective cluster interactions for (Zn, Mg)O, (Zn, Co)O, and (Zn, Ni)O, respectively. The fits are in reasonable agreement with the DFT calculations.

Using the fitted cluster expansion model, the thermodynamic stability of these alloys at finite temperature was modeled using Monte Carlo simulations within the μVT ensemble *via* the Metropolis sampling method[368]. In these simulations, 9 × 9 × 9 supercells of the convex hull structures were simulated at temperatures of 800 to 1900 °C and chemical potentials ($\Delta\mu = \mu_i - \mu_{ZnO}$) of -1000 to 1000 meV per mole. This relative chemical potential as a function of composition and temperature can be modeled as in **Eq. A.4** where A and B are fitted parameters, and the Gibbs free mixing energy, $\Delta G_m ix$, is calculated as an integral of the chemical potential over the composition space (**Eq. A.5**).

$$\Delta\mu(T, x) = Aln(x) - Bln(1 - x) \tag{A.4}$$

$$\Delta G_{mix} = \int_0^1 \mu dx \tag{A.5}$$

The ΔG_{mix} is converted to the formation energy, ΔG_f , to compare these energies on the same reference (**Eq. A.6**. Here, E_{Zn}, E_A, and E_{O_2} are the calculated reference energies of Zn, A, and O_2, respectively.

$$\Delta G_f = \Delta G_{mix} - (1 - x)(E_{Zn} - E_{ZnO}) - x(E_A - E_{AO}) - \frac{1}{2}E_{O_2} \tag{A.6}$$

Using these energies, the phase boundaries are calculated by constructing the common tangent line between the ΔG_f of the two phases. Since the ΔG_f values are similar between the wurtzite and rocksalt phases, an accurate construction is required. A semi-empirical approach is applied where the ΔG_f of the rocksalt phase is shifted downward by a correction, Δ_r , such that the calculated phase boundaries are in reasonable agreement with the experimental data[183, 187, 369, 370]. This method is justified since the accuracy of formation energies from DFT using GGA exchange-correlation functionals is 0.2-0.8 eV per atom[371]. Other discrepancies between first-principles calculations and experimental data can result from the zero-point energy[372], vibrational entropy[373], and deviations from coherent solids[374].

Determining the common tangent line includes solving this system of equations (**Eq. A.7** and **Eq. A.8**) where x^w, x^r are the phase boundaries. In other words, the slopes of the two phases are equal at these boundaries and this slope is equal to the common tangent.

$$\left(\frac{dG_f^W}{dx}\right)_{x=x^w} = \left(\frac{dG_f^r}{dx}\right)_{x=x^r} \tag{A.7}$$

$$\left(\frac{dG_f^W}{dx}\right)_{x=x^w} = \frac{G_f^r(x^r) - G_r^W(x^W)}{x^r - x^w} \tag{A.8}$$

APPENDIX B

Additional Measurements of (MgCoNiCuZn)O

The results presented in this appendix are from the supplementary information of my own work in 'M. Webb, et al. High temperature stability of entropy-stabilized oxide $(MgCoNiCuZn)_{0.2}O$ in air. *Appl. Phys. Lett.* (2024)'[150].

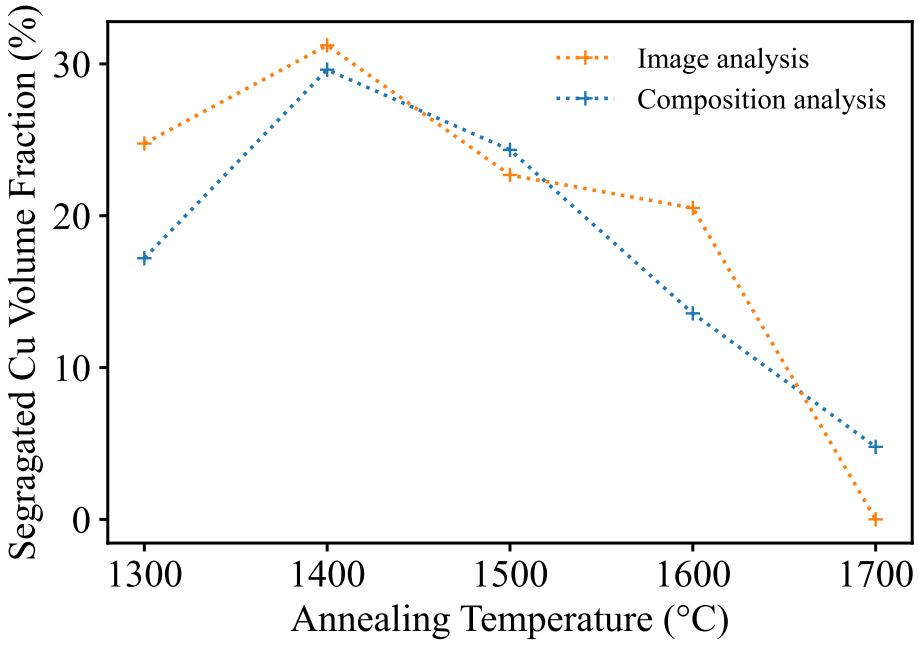


Figure B.1: Cu-rich region analysis. A peak in the volume fraction of Cu-rich regions occurs at around 1400 ºC, close to the melting temperature of tenorite CuO. The volume fraction has been calculated by analyzing the SEM EDS images of Cu concentration, as well as by a lever-rule[375] calculation, using the average Cu concentration of (MgCoNiCuZn)O particles and the overall Cu concentration of the region. Volume fraction analysis was performed using ImageJ Software[376].

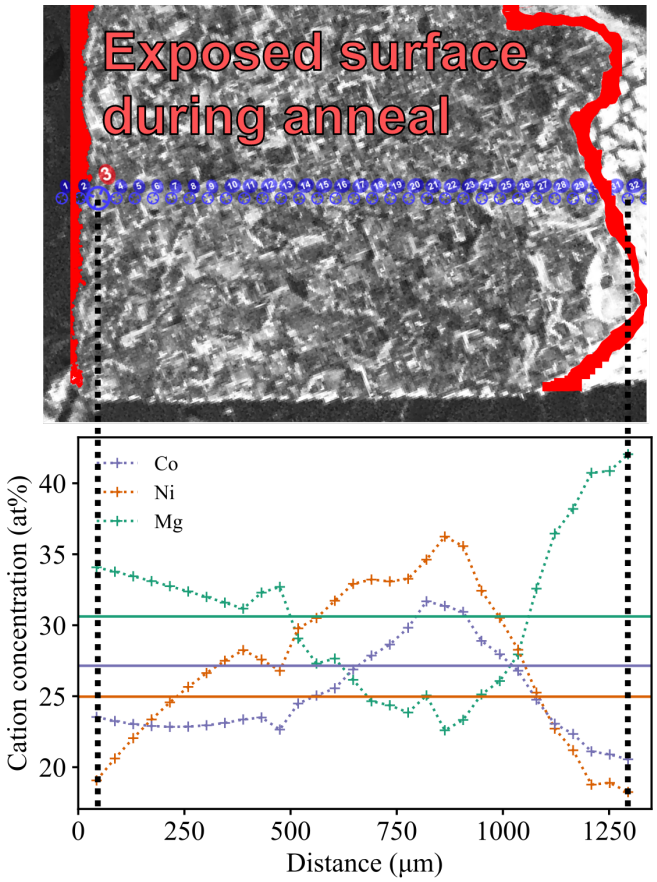


Figure B.2: SEM EDS linescan of (MgCoNiCuZn)O annealed at 1600 ºC. Atomic percent linescan of Mg, Ni, and Co concentration in at% across the center of the annealed pellet. A Savitzky-Golay filter was used to smooth the data. Red-highlighted surfaces were the surfaces exposed during the annealing treatment. There is a clear increase in concentration of Mg at both surfaces of the pellet that were exposed during the heat treatment. Solid lines note the average cation composition over this region..

APPENDIX C

Selecting Nanophotonic Materials

Reproduced from 'S. McSherry[†], M. Webb[†], et al. Nanophotonic control of thermal emission under extreme temperatures in air. *Nat. Nanotechnol.*(2022)'[28].

Stability of $BaZr_{0.5}Hf_{0.5}O_3$/MgO heterostructures under extreme temperatures in air conditions $BaZr_{0.5}Hf_{0.5}O_3$and MgO were down-selected from a large computational dataset[244] based on a set of constraints namely (i) similar lattice constant, (ii) dissimilar crystal structures and very high melting point, and (iii) refractive index mismatch that is relatively insensitive to temperature. The use of different crystal structures such as rocksalt, perovskite, spinel, and pyrochlore, which all have unique unit cells with different atomic arrangements and oxygen sublattices, is expected to create barriers to cation diffusion and mixing. A low lattice and thermal expansion mismatch between layers allows for highly crystalline superlattices. These wide-bandgap oxides also maintain high refractive index contrast and negligible optical absorption over a large temperature range.

$BaZr_{0.5}Hf_{0.5}O_3$/MgO illustrates the concept of using highly crystalline, immiscible refractory materials as building blocks of ultrahigh-temperature photonic designs. Extending the concept to other material systems may overcome some of the specific the limitations of $BaZr_{0.5}Hf_{0.5}O_3$/MgO and could enable breakthroughs in a wide range photonic and energy conversion applications by extending the air-stable operating temperature beyond 1100 ℃ and providing plasmonic/polaritonic functionality.

Our search for new nanophotonic materials is facilitated by a materials screening algorithm (see Figure 5) that predicts high-temperature building blocks based on the down-selection requirements we implemented in our manual screening process to select $BaZr_{0.5}Hf_{0.5}O_3$/MgO. The algorithm matches oxide films to a preferred substrate by using structural and chemical data on over 20,000 oxide entries on the materials project database[244].

First, films of different crystal structures are matched to a chosen substrate in viable configurations based on crystal structure and interface. To narrow the list of compatible films, we set a lattice

[†]These authors contributed equally.

strain cutoff of 5 %, which is intentionally large to account for any noise within the computational data. For high-temperature nanophotonic applications we further narrow the list by only considering wide-bandgap candidates (over 2 eV) with minimal lattice strain and high refractive index contrast. Applying our algorithm to common growth substrates such as MgO, $LaAlO_3$, Y:ZrO_2 and $MgAl_2O_4$ results in several pairs including the following top candidates, A: $BaZr_{0.5}Hf_{0.5}O_3$-MgO, B: CeO_2 - $LaAlO_3$, and C: $KTaO_3$ - $MgAl_2O_4$. Candidate A offers validation against our manual screening process.

For these systems, it is important to evaluate risk based on experimental data to validate the lattice compatibility, index contrast, and bandgap requirements and to fill in lacking computational data, such as melting temperatures and thermal expansion coefficients. For example, in this work, once we identified $BaZr_{0.5}Hf_{0.5}O_3$ and MgO as a candidate pair, we evaluated the melting temperatures of $BaZr_{0.5}Hf_{0.5}O_3$ (2700 ºC) and MgO (2850 ºC) and decided these were acceptable because they were much higher than 2000 ºC, which is generally preferred for this area of nanophotonics[377]. Additionally, we evaluated experimental thermal expansion coefficients of $BaZr_{0.5}Hf_{0.5}O_3$ ($\sim$7×10^{-6} K^{-1})[243, 378] and MgO ($\sim$11 – 14×10^{-6} K^{-1})[379] and decided the mismatch was feasible based on previous experiments. For the materials screening algorithm, we added a simple approximation for the coefficient of thermal expansion[380] based on the Grüneisen equation (**Eq. C.1**) but the accuracy of this method has yet to be tested on a large experimental dataset. N_A is Avogadro's constant, k_B is Boltzmann's constant, μ is Poisson's ratio, B is the bulk modulus, V is the molar volume and n is the number of atoms in the molecular formula, all of these values are available on materials project.

$$CTE = \frac{3nN_A k_B \frac{1+\mu}{2-3\mu}}{2BV} \tag{C.1}$$

By loosening the bandgap and index requirements suggested in **Figure C.1**, the number of potential candidates increases significantly. For MgO, there are 54/480 stable/metastable candidates (see supplemental section S9 for full list). Our algorithm accounts for qualitative charge stability by only considering interfaces with similar oxygen or cation sublattices (see supplementary S9), but more work must be done to include higher-fidelity calculations that predict interface stability. This may include minimal coincident interface area calculations, which are used in the materials project substrate finder[381].

Additionally, for photonic applications, a closer look at the bandgap energy and refractive index must be considered due to the well-known inaccuracy in bandgap prediction with density functional theory. Nonetheless, this computational result reveals that there is substantial room for further improving the stability and performance of nanophotonic materials under extreme

conditions and environments. The discovery of an ultrahigh-temperature thermal emitter could unlock the use of wider-bandgap semiconductors in TPVs, some of which have an established infrastructure for production. In addition to TPVs, the concept of immiscible refractory photonics, demonstrated here, could lead to advances in several areas, including selective solar thermal absorbers[229, 250, 251, 382], broadband directional control using high-quality gradient epsilon near-zero materials[40], and thermal barrier coatings[383].

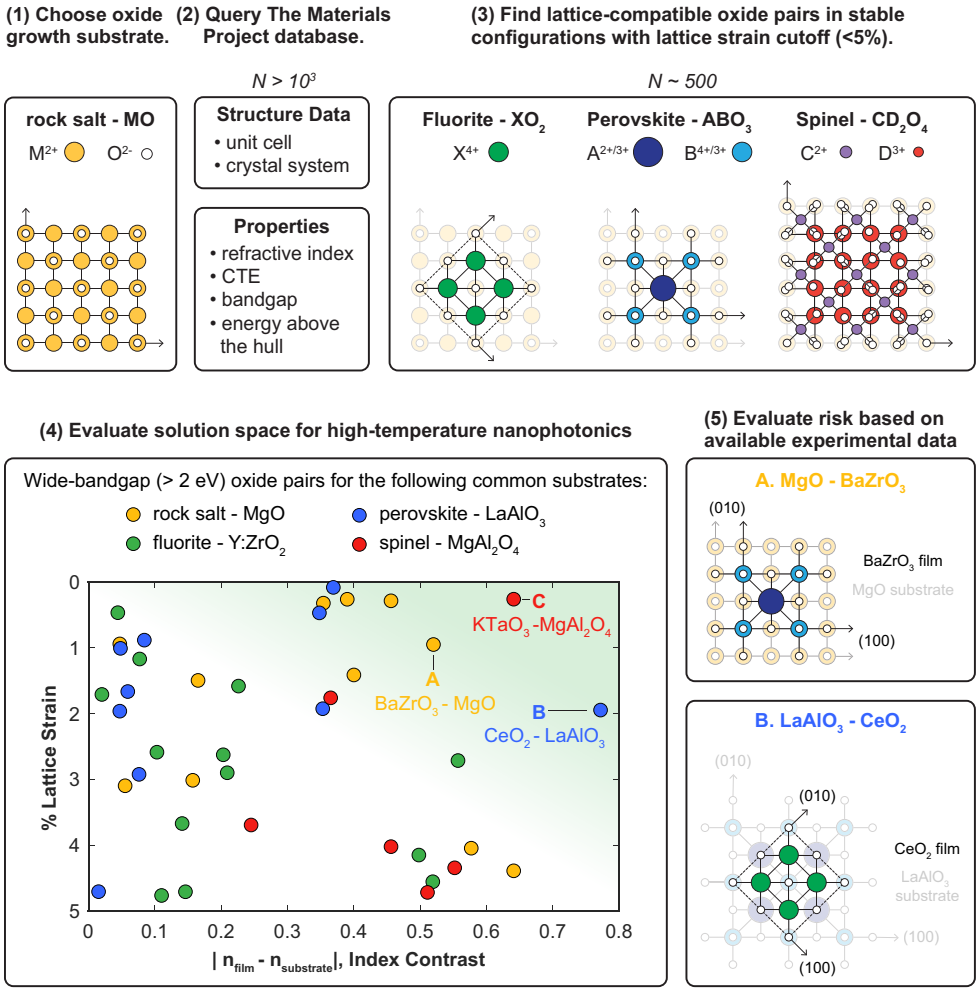


Figure C.1: The screening process consists of five main steps. (1) An oxide substrate with a high melting point (over 2,000 ºC) is selected. (2) The Materials Project database is queried to gather properties of candidate oxide pairs. (3) Lattice-compatible pairs are identified by considering stable configurations between the different oxides and a lattice misfit strain cutoff of 5% is applied. (4) Candidates are filtered by applying a bandgap cutoff of 2 eV and evaluated based on the criteria of minimal lattice strain and maximum refractive-index contrast. (5) Down-selected candidates are assessed using the available experimental data (for example, melting points). $MgO/BaZrO_3$ (top) and $LaAlO_3/CeO_2$ (bottom) are two example systems that have minimal lattice strain, different crystal types, high melting points and contrasting refractive indices.

APPENDIX D

Filament Formation Kinetics

The movement of charged oxygen vacancies can be modeled based on drift and diffusion processes (**Eq. D.1**).

$$J_i = -czy_{ij}\nabla_j\Phi - \frac{cD_{ij}}{k_BT}\nabla_j\mu \tag{D.1}$$

where the first term represents the drift a charged, z, vacancy density, c, in a gradient of an electric potential field, ϕ, gradient with tensor mobility, γ_{ij}, and the second term represents a generalized flux driven by a chemical potential, μ, gradient with D_{ij} representing the Fickian tensor diffusivity that has an Arrhenius temperature dependence. Note that the latter term has been used to describe filament stability from thermodynamic phase coexistence but also reduces to the famous Fick's law when the gradient of the chemical potential is derived from configurational entropy[384].

From the Nernst-Einstein relation, the mean mobility of these oxygen vacancies would have a temperature dependence related to the activation energy (E_A) of the associated Boltzmann probability distribution. This would lead to a temperature dependent fatigue as higher temperature results in a higher mobility, and potentially a faster filament formation (assuming the filament is stable at these temperatures) or a greater rate of charge trapping at the interface. As these are charged vacancies, the application of an electric field can modulate the activation energy, effectively increasing the mobility at low temperatures.

For the formation of conductive filaments, we can start with Ficks' second law of diffusion, **Eq. D.2**, where C is the concentration, t is time and D is the diffusivity of the diffusing species.

$$\frac{\partial C}{\partial t} = D\nabla^2 C \tag{D.2}$$

By assuming a thin source, constant total number of impurities (oxygen vacancies), and no

initial concentration, we get the conditions $C(x > 0, t = 0) = 0$ and $\int C(x,t)\, dx = B$, where B is some constant . This results in the 1D solution shown in **Eq. D.3**.

$$C(x,t) = \frac{B}{\sqrt{\pi Dt}} exp\left(\frac{-x^2}{4Dt}\right) \tag{D.3}$$

Considering the standard deviation of this Gaussian, we get the expected diffusion length in **Eq. D.4**.

$$L = \sqrt{2Dt} \tag{D.4}$$

Rearranging this for t and subbing in the Arrhenius form of $D = D_0 exp(\frac{-E_A}{k_B T})$, we get **Eq. D.5**, where $E_A^{'}$ is the field modified activation energy.

$$t = \frac{L^2}{2D_0 exp(\frac{-E_A^{'}}{k_B T})} \tag{D.5}$$

Finally, by taking the logarithm of this and using that $N = \gamma t$ (where γ is the time under applied field per cycle) we can see the relationship between cycles to failure, N, and temperature T in **Eq. D.6**.

$$ln\left(\frac{N}{\gamma}\right) = 2lnL - ln(2D_0) + \frac{E_A^{'}}{k_B T} \tag{D.6}$$

This can be simplified to **Eq. D.7**, where A and k_B are both constants. γ, L, and D_0 have all been incorporated in to A.

$$ln(N) = A + \frac{E_A^{'}}{k_B T} \tag{D.7}$$

BIBLIOGRAPHY

[1] Yu, P. *Emergent Phenomena at Complex Oxide Interfaces*. PhD thesis, UC Berkeley (2011).

[2] Pollock, T. M. & Tin, S. Nickel-Based Superalloys for Advanced Turbine Engines: Chemistry, Microstructure and Properties. *Journal of Propulsion and Power* **22**, 361–374 (2006).

[3] Prabhakaran, R. The High Pressure Gas Turbine Blades of Jet Engines. *Journal of Aerospace Sciences and Technologies* **69**, 261–285 (2023).

[4] Jain, N. *et al.* A Critical Review of Physical Models in High Temperature Multiphase Fluid Dynamics: Turbulent Transport and Particle-Wall Interactions. *Applied Mechanics Reviews* **73**, 040801 (2021).

[5] Gudivada, G. & Pandey, A. K. Recent developments in nickel-based superalloys for gas turbine applications: Review. *Journal of Alloys and Compounds* **963**, 171128 (2023).

[6] Kyprianidis, K. G. Future Aero Engine Designs: An Evolving Vision. In *Advances in Gas Turbine Technology*. InTech (2011).

[7] Viswanathan, R. & Stringer, J. Failure Mechanisms of High Temperature Components in Power Plants. *Journal of Engineering Materials and Technology* **122**, 246–255 (2000).

[8] Wulpi, D. J. *Understanding How Components Fail*. ASM International, 3rd edition (2013).

[9] Wu, R., Kawagishi, K., Harada, H. & Reed, R. The retention of thermal barrier coating systems on single-crystal superalloys: Effects of substrate composition. *Acta Materialia* **56**, 3622–3629 (2008).

[10] Barwinska, I., Kopec, M., Kukla, D., Senderowski, C. & Kowalewski, Z. Thermal Barrier Coatings for High-Temperature Performance of Nickel-Based Superalloys: A Synthetic Review. *Coatings* **13**, 769 (2023).

[11] Ju, J. *et al.* Understanding the oxidation behaviors of a Ni-Co-based superalloy at elevated temperatures through multiscale characterization. *Corrosion Science* **227**, 111800 (2024).

[12] Hashmi, S., Ferreira Batalha, G., Van Tyne, C. J. & Yilbas, B. S. *Comprehensive Materials Processing*. Elsevier (2014).

[13] Starschich, S., Menzel, S. & Böttger, U. Evidence for oxygen vacancies movement during wake-up in ferroelectric hafnium oxide. *Applied Physics Letters* **108**, 032903 (2016).

[14] Reznicek, A. *et al.* Dynamics of Defects in Strained Silicon, Strained SiGe and Strained Germanium. In *Extended Abstracts of the 2006 International Conference on Solid State Devices and Materials* (2006).

[15] McClure, Z. D. & Strachan, A. Expanding Materials Selection Via Transfer Learning for High-Temperature Oxide Selection. *JOM* **73**, 103–115 (2021).

[16] Abdullah, Md., Ahmed, I., Arafat Islam, M., Ahsan, Z. & Saha, S. Recent developments and diverse applications of high melting point materials. *Results in Engineering* **22**, 102376 (2024).

[17] Sahu, S. K. & Navrotsky, A. High-Temperature Materials Chemistry and Thermodynamics. In *High Temperature Materials and Mechanisms*. CRC Press (2014).

[18] Zhou, W. X. & Ariando, A. Review on ferroelectric/polar metals. *Jpn. J. Appl. Phys.* **59**, SI0802 (2020).

[19] Qi, J. *Metal Oxides and Related Solids for Electrocatalytic Water Splitting*. Elsevier (2022).

[20] Mellah, H. & Sansò, B. Review of Facts, Data and Proposals for a Greener Internet. In *Proceedings of the 6th International ICST Conference on Broadband Communications, Networks, and Systems* (2009).

[21] Kochupurackal Rajan, S., Ramakrishnan, B., Alissa, H., Kim, W., Belady, C. & Bakir, M. S. Integrated Silicon Microfluidic Cooling of a High-Power Overclocked CPU for Efficient Thermal Management. *IEEE Access* **10**, 59259–59269 (2022).

[22] Misra, P. A. *et al.* Overclocking in Immersion-Cooled Datacenters. *IEEE Micro* **42**, 10–17 (2022).

[23] Ramakrishnan, B. *et al.* CPU Overclocking: A Performance Assessment of Air, Cold Plates, and Two-Phase Immersion Cooling. *IEEE Transactions on Components, Packaging and Manufacturing Technology* **11**, 1703–1715 (2021).

[24] Jalili, M. *et al.* Cost-Efficient Overclocking in Immersion-Cooled Datacenters. In *2021 ACM/IEEE 48th Annual International Symposium on Computer Architecture (ISCA)*, pp. 623–636 (2021).

[25] Dias, M. R. S. *et al.* Photonics roadmap for ultra-high-temperature thermophotovoltaics. *Joule* **7**, 2209–2227 (2023).

[26] Tervo, E. J. *et al.* Efficient and scalable GaInAs thermophotovoltaic devices. *Joule* **6**, 2566–2584 (2022).

[27] Omair, Z. *et al.* Ultraefficient thermophotovoltaic power conversion by band-edge spectral filtering. *Proceedings of the National Academy of Sciences* **116**, 15356–15361 (2019).

[28] McSherry, S. *et al.* Nanophotonic control of thermal emission under extreme temperatures in air. *Nature Nanotechnology* **17**, 1104–1110 (2022).

[29] Nakagawa, N., Ohtsubo, H., Waku, Y. & Yugami, H. Thermal emission properties of $Al_2O_3/Er_3Al_5O_{12}$ eutectic ceramics. *Journal of the European Ceramic Society* **25**, 1285–1291 (2005).

[30] Bitnar, S. *et al.* Practical thermophotovoltaic generators. *Semiconductors* **38**, 941–945 (2004).

[31] Yeng, Y. X. *et al.* Enabling high-temperature nanophotonics for energy applications. *Proceedings of the National Academy of Sciences* **109**, 2280–2285 (2012).

[32] Arpin, K. A. *et al.* Three-dimensional self-assembled photonic crystals with high temperature stability for thermal emission modification. *Nature Communications* **4**, 2630 (2013).

[33] Woolf, D. N. *et al.* High-efficiency thermophotovoltaic energy conversion enabled by a metamaterial selective emitter. *Optica* **5**, 213–218 (2018).

[34] Rinnerbauer, V. *et al.* High-temperature stability and selective thermal emission of polycrystalline tantalum photonic crystals. *Opt. Express* **21**, 11482–11491 (2013).

[35] Zhang, S. & Ali, N. *Nanocomposite Thin Films and Coatings*. Imperial College Press (2007).

[36] Ramesh, R. & Spaldin, N. A. Multiferroics: Progress and prospects in thin films. *Nature Materials* **6**, 21–29 (2007).

[37] Wu, R. *et al.* Self-biased magnetoelectric switching at room temperature in three-phase ferroelectric–antiferromagnetic–ferrimagnetic nanocomposites. *Nature Electronics* **4**, 333–341 (2021).

[38] Zubko, P. *et al.* Negative capacitance in multidomain ferroelectric superlattices. *Nature* **534**, 524–528 (2016).

[39] Ying, Y. *et al.* Whole LWIR Directional Thermal Emission Based on ENZ Thin Films. *Laser & Photonics Reviews* **16**, 2200018 (2022).

[40] Xu, J., Mandal, J. & Raman, A. P. Broadband directional control of thermal emission. *Science* **372**, 393–397 (2021).

[41] Balachandran, P. V. & Rondinelli, J. M. Massive band gap variation in layered oxides through cation ordering. *Nature Communications* **6**, 6191 (2015).

[42] Das, S. *et al.* Perspective: Emergent topologies in oxide superlattices. *APL Materials* **6**, 100901 (2018).

[43] Chen, B. *et al.* Spatially Controlled Octahedral Rotations and Metal–Insulator Transitions in Nickelate Superlattices. *Nano Lett.* **21**, 1295–1302 (2021).

[44] Aguado-Puente, P. & Junquera, J. Structural and energetic properties of domains in $PbTiO_3/SrTiO_3$ superlattices from first principles. *Phys. Rev. B* **85**, 184105 (2012).

[45] Hoglund, E. R. *et al.* Emergent interface vibrational structure of oxide superlattices. *Nature* **601**, 556–561 (2022).

[46] Burger, T., Sempere, C., Roy-Layinde, B. & Lenert, A. Present Efficiencies and Future Opportunities in Thermophotovoltaics. *Joule* **4**, 1660–1680 (2020).

[47] Apell, P. & Hunderi, O. Chapter 5 - Optical Properties of Superlattices. In *Handbook of Optical Constants of Solids*, pp. 97–124. Academic Press (1998).

[48] Chirumamilla, M. *et al.* Metamaterial emitter for thermophotovoltaics stable up to 1400 °C. *Scientific Reports* **9**, 7241 (2019).

[49] Stelmakh, V. *et al.* High-temperature tantalum tungsten alloy photonic crystals: Stability, optical properties, and fabrication. *Appl. Phys. Lett.* **103**, 123903 (2013).

[50] Rosendahl, P. L. *Bulk Material Failure*, volume 57, pp. 99–125. Springer (2021).

[51] Evans, A. G. & Rana, A. High temperature failure mechanisms in ceramics. *Acta Metallurgica* **28**, 129–141 (1980).

[52] Kang, C.-W. & Huang, H. Deformation, failure and removal mechanisms of thin film structures in abrasive machining. *Adv. Manuf.* **5**, 1–19 (2017).

[53] Shugurov, A. R. & Panin, A. V. Mechanisms of stress generation and relaxation in thin films and coatings. In *International Conference on Physical Mesomechanics of Multilevel Systems 2014*, pp. 575–578 (2014).

[54] Bull, S. Failure mode maps in the thin film scratch adhesion test. *Tribology International* **30**, 491–498 (1997).

[55] Jin, X., Ma, B., Deng, J., Luo, J. & Yuan, W. High temperature failure modes of In_2O_3 thin films and improved thermal stability using Al_2O_3/ZrO_2 protective layers. *Ceramics International* **47**, 28411–28418 (2021).

[56] Abadias, G. *et al.* Review Article: Stress in thin films and coatings: Current status, challenges, and prospects. *Journal of Vacuum Science & Technology A* **36**, 020801 (2018).

[57] Clarke, D. R. Stresses in Thin Films and Characteristic Failure Modes. In *Optical Interference Coatings*. Optica Publishing Group (1995).

[58] Gabriel, O. E. & Huitink, D. R. Failure Mechanisms Driven Reliability Models for Power Electronics: A Review. *Journal of Electronic Packaging* **145**, 020801 (2023).

[59] Wu, B., Zimmers, A., Aubin, H., Ghosh, R., Liu, Y. & Lopez, R. Electric-field-driven phase transition in vanadium dioxide. *Phys. Rev. B* **84**, 241410 (2011).

[60] Lu, N. *et al.* Electric-field control of tri-state phase transformation with a selective dual-ion switch. *Nature* **546**, 124–128 (2017).

[61] Daniels, J. E., Jo, W., Rödel, J. & Jones, J. L. Electric-field-induced phase transformation at a lead-free morphotropic phase boundary: Case study in a 93%($Bi_{0.5}Na_{0.5}$)TiO_3–7% $BaTiO_3$ piezoelectric ceramic. *Appl. Phys. Lett.* **95**, 032904 (2009).

[62] Zipoli, F., Viterbo, V., Schilter, O., Kahle, L. & Laino, T. Prediction of Phase Diagrams and Associated Phase Structural Properties. *Ind. Eng. Chem. Res.* **61**, 8378–8389 (2022).

[63] Widom, M. Prediction of Structure and Phase Transformations. In Gao, M. C., Yeh, J.-W., Liaw, P. K. & Zhang, Y., editors, *High-Entropy Alloys*, pp. 267–298. Springer International Publishing (2016).

[64] Liu, G., Zhang, S., Jiang, W. & Cao, W. Losses in ferroelectric materials. *Materials Science and Engineering: R: Reports* **89**, 1–48 (2015).

[65] Sicron, N., Ravel, B., Yacoby, Y., Stern, E. A., Dogan, F. & Rehr, J. J. Nature of the ferroelectric phase transition in $PbTiO_3$. *Phys. Rev. B* **50**, 13168–13180 (1994).

[66] Smith, M. B. *et al.* Crystal Structure and the Paraelectric-to-Ferroelectric Phase Transition of Nanoscale $BaTiO_3$. *J. Am. Chem. Soc.* **130**, 6955–6963 (2008).

[67] Kaul, A. R. *et al.* Epitaxial phase stabilization in thin films of complex oxides. *International Journal of Inorganic Materials* **3**, 1177–1180 (2001).

[68] Naghibzadeh, S. K., Xu, Z., Kinderlehrer, D., Suter, R., Dayal, K. & Rohrer, G. S. Impact of grain boundary energy anisotropy on grain growth. *Phys. Rev. Mater.* **8**, 093403 (2024).

[69] Hu, J., Wang, X., Zhang, J., Luo, J., Zhang, Z. & Shen, Z. A general mechanism of grain growth -i. Theory. *Journal of Materiomics* **7**, 1007–1013 (2021).

[70] Mullins, W. W. Two-Dimensional Motion of Idealized Grain Boundaries. *Journal of Applied Physics* **27**, 900–904 (1956).

[71] Turnbull, D. Theory of Grain Boundary Migration Rates. *JOM* **3**, 661–665 (1951).

[72] Van Der Ven, A., Yu, H.-C., Ceder, G. & Thornton, K. Vacancy mediated substitutional diffusion in binary crystalline solids. *Progress in Materials Science* **55**, 61–105 (2010).

[73] Liu, F. & Gencang, Y. Stress-induced recrystallization mechanism for grain refinement in highly undercooled superalloy. *Journal of Crystal Growth* **231**, 295–305 (2001).

[74] Thompson, C. V. & Carel, R. Stress and grain growth in thin films. *Journal of the Mechanics and Physics of Solids* **44**, 657–673 (1996).

[75] Ahmad, Z. Types of Corrosion. In *Principles of Corrosion Engineering and Corrosion Control*, pp. 120–270. Elsevier (2006).

[76] Morshed-Behbahani, K. & Zakerin, N. A review on the role of surface nanocrystallization in corrosion of stainless steel. *Journal of Materials Research and Technology* **19**, 1120–1147 (2022).

[77] Aschauer, E. *et al.* Ultra-high oxidation resistance of nano-structured thin films. *Materials & Design* **201**, 109499 (2021).

[78] Kutz, M., editor *Handbook of Environmental Degradation of Materials*. William Andrew Publishing, 2nd edition (2012).

[79] Bose, S. *High Temperature Coatings*. Butterworth-Heinemann (2007).

[80] Hamdy Makhlouf, A. S. & Aliofkhazra, M. *Handbook of Materials Failure Analysis*. Butterworth-Heinemann (2018).

[81] Tigunta, S., Sando, D., Chanlek, N., Supadee, L. & Pojprapai, S. Effect of gas atmospheres on degradation of MgO thin film magnetic tunneling junctions by deionized water. *Thin Solid Films* **709**, 138185 (2020).

[82] Pineau, A., McDowell, D. L., Busso, E. P. & Antolovich, S. D. Failure of metals II: Fatigue. *Acta Materialia* **107**, 484–507 (2016).

[83] Antaki, G. & Gilada, R. Chapter 2 - Design Basis Loads and Qualification. In *Nuclear Power Plant Safety and Mechanical Integrity*, pp. 27–102. Butterworth-Heinemann (2015).

[84] Campbell, J. Properties of Castings. In *Complete Casting Handbook*, pp. 447–528. Elsevier (2015).

[85] Zhang, G., Volkert, C., Schwaiger, R., Monig, R. & Kraft, O. Fatigue and Thermal Fatigue Damage Analysis of Thin Metal Films. In *EuroSime 2006 - 7th International Conference on Thermal, Mechanical and Multiphysics Simulation and Experiments in Micro-Electronics and Micro-Systems*, pp. 1–6 (2006).

[86] Bradeško, A. *et al.* Electrocaloric fatigue of lead magnesium niobate mediated by an electric-field-induced phase transformation. *Acta Materialia* **169**, 275–283 (2019).

[87] Lupascu, D. C. *Fatigue in Ferroelectric Ceramics and Related Issues*. Heidelberg: Springer (2004).

[88] Lou, X. J. Polarization fatigue in ferroelectric thin films and related materials. *Journal of Applied Physics* **105**, 024101 (2009).

[89] Glaum, J. & Hoffman, M. Electric Fatigue of Lead-Free Piezoelectric Materials. *Journal of the American Ceramic Society* **97**, 665–680 (2014).

[90] Chen, W. *et al.* Essential Characteristics of Memristors for Neuromorphic Computing. *Advanced Electronic Materials* **9**, 2200833 (2023).

[91] Van Orman, J. A. & Crispin, K. L. Diffusion in Oxides. *Reviews in Mineralogy and Geochemistry* **72**, 757–825 (2010).

[92] Gholipour Shahraki, M. & Ghorbanali, S. The temperature and oxygen vacancy effects on the diffusion coefficient and ionic conductivity in ferroelectric $BaTiO_3$ nanowires; A molecular dynamics study. *Microelectronics Reliability* **82**, 153–158 (2018).

[93] Varalda, J., Dartora, C. A., de Camargo, P. C., de Oliveira, A. J. A. & Mosca, D. H. Oxygen diffusion and vacancy migration thermally-activated govern high-temperature magnetism in ceria. *Sci Rep* **9**, 4708 (2019).

[94] Zarnas, P. D., Boyce, B. L., Qu, J. & Dingreville, R. Stress-induced transition from vacancy annihilation to void nucleation near microcracks. *International Journal of Solids and Structures* **213**, 103–110 (2021).

[95] Bampoulis, P., van Bremen, R., Yao, Q., Poelsema, B., Zandvliet, H. J. W. & Sotthewes, K. Defect Dominated Charge Transport and Fermi Level Pinning in MoS_2/Metal Contacts. *ACS Appl. Mater. Interfaces* **9**, 19278–19286 (2017).

[96] Du, H. *et al.* Nanosized Conducting Filaments Formed by Atomic-Scale Defects in Redox-Based Resistive Switching Memories. *Chem. Mater.* **29**, 3164–3173 (2017).

[97] Mallick, A., Lenox, M. K., Beechem, T. E., Ihlefeld, J. F. & Shukla, N. Oxygen vacancy contributions to the electrical stress response and endurance of ferroelectric hafnium zirconium oxide thin films. *Applied Physics Letters* **122**, 132902 (2023).

[98] Callister, W. D. & Rethwisch, D. G. *Materials Science and Engineering*. Wiley, 10$^{\text{th}}$ edition (2018).

[99] Mizutani, U., Sato, H. & Massalski, T. B. The original concepts of the Hume-Rothery rule extended to alloys and compounds whose bonding is metallic, ionic, or covalent, or a changing mixture of these. *Progress in Materials Science* **120**, 100719 (2021).

[100] Hume-Rothery, W., Mabbott, G. W. & Channel Evans, K. M. The freezing points, melting points, and solid solubility limits of the alloys of silver and copper with the elements of the B sub-groups. *Phil. Trans. R. Soc. Lond. A* **233**, 1–97 (1934).

[101] Kim, J.-Y., Jin, M.-J., Hou, B., Kim, M. P., Um, D.-S. & Kim, C.-I. Reducing the oxygen vacancy concentration in $SrTiO_{3-\delta}$ thin films via an optimized O_2 plasma treatment for enhancing device properties. *Applied Surface Science* **639**, 158271 (2023).

[102] Zhang, X., Peng, S., Huang, H., Guo, X., Boukhachem, A. & Deng, L. Effect of annealing temperature on oxygen vacancy and infrared radiation properties of the Co doped α-MoO_3 materials. *Current Applied Physics* **50**, 25–31 (2023).

[103] Alberi, K. & Scarpulla, M. A. Suppression of compensating native defect formation during semiconductor processing via excess carriers. *Sci Rep* **6**, 27954 (2016).

[104] Black, J. Electromigration—A brief survey and some recent results. *IEEE Transactions on Electron Devices* **16**, 338–347 (1969).

[105] Lienig, J. & Thiele, M. *Fundamentals of Electromigration-Aware Integrated Circuit Design*. Springer International Publishing (2018).

[106] d'Heurle, F. Electromigration and failure in electronics: An introduction. *Proceedings of the IEEE* **59**, 1409–1418 (1971).

[107] Zhang, L., He, C.-W., Guo, Y.-H., Han, J.-G., Zhang, Y.-W. & Wang, X.-Y. Development of SnAg-based lead free solders in electronics packaging. *Microelectronics Reliability* **52**, 559–578 (2012).

[108] Vinci, R. P. & Vlassak, J. J. Mechanical Behavior of Thin Films. *Annu. Rev. Mater. Sci.* **26**, 431–462 (1996).

[109] Forschelen, P. J. J., Suiker, A. S. J. & van der Sluis, O. Effect of residual stress on the delamination response of film-substrate systems under bending. *International Journal of Solids and Structures* **97–98**, 284–299 (2016).

[110] Zhang, H., Zhou, Z., Chudnovsky, A. & Pham, H. Time-dependent buckling delamination of thin plastic films and their conformability: Observations and modeling. *International Journal of Engineering Science* **150**, 103258 (2020).

[111] Walther, M., Biehl, M. & Kinzel, W. Formation and consequences of misfit dislocations in heteroepitaxial growth. *Phys. Status Solidi (c)* **4**, 3210–3220 (2007).

[112] Dunstan, D. J. Strain and strain relaxation in semiconductors. *Journal of Materials Science: Materials in Electronics* **8**, 337–375 (1997).

[113] Pisutha-Arnond, N., Yang, B., Lim, D. H., Asta, M. & Thornton, K. Stability of strained thin films with interface misfit dislocations: A multiscale computational study. *Thin Solid Films* **519**, 809–817 (2010).

[114] Navickas, E. *et al.* Dislocations Accelerate Oxygen Ion Diffusion in $La_{0.8}Sr_{0.2}MnO_3$ Epitaxial Thin Films. *ACS Nano* **11**, 11475–11487 (2017).

[115] Verberne, R. *et al.* Dislocations in minerals: Fast-diffusion pathways or trace-element traps? *Earth and Planetary Science Letters* **584**, 117517 (2022).

[116] McPherson, J. W. Time dependent dielectric breakdown physics – Models revisited. *Microelectronics Reliability* **52**, 1753–1760 (2012).

[117] Li, X., Tung, C. H. & Pey, K. L. The nature of dielectric breakdown. *Applied Physics Letters* **93**, 072903 (2008).

[118] Lindon, J. C., Tranter, G. E. & Holmes, J. L. *Encyclopedia of Spectroscopy and Spectrometry*. Elsevier (2010).

[119] Als-Nielsen, J. & McMorrow, D. *Elements of Modern X-ray Physics*. Wiley, 2nd edition (2011).

[120] Cline, J. P., Mendenhall, M. H., Black, D., Windover, D. & Henins, A. The Optics and Alignment of the Divergent Beam Laboratory X-ray Powder Diffractometer and its Calibration Using NIST Standard Reference Materials. *J Res Natl Inst Stand Technol.* **120**, 173 (2015).

[121] Birkholz, M., Fewster, P. F. & Genzel, C. *Thin Film Analysis by X-ray Scattering*. Wiley (2006).

[122] Huang, T., Gilles, R. & Will, G. Thin-film thickness and density determination from x-ray reflectivity data using a conventional power diffractometer. *Thin Solid Films* **230**, 99–101 (1993).

[123] Feidenhans'l, R. Surface structure determination by X-ray diffraction. *Surface Science Reports* **10**, 105–188 (1989).

[124] Penkov, O. V., Kopylets, I. A., Khadem, M. & Qin, T. X-Ray Calc: A software for the simulation of X-ray reflectivity. *SoftwareX* **12**, 100528 (2020).

[125] Ohring, M. *Materials Science of Thin Films: Deposition and Structure*. Academic Press, 2nd edition (2002).

[126] Harrington, G. F. & Santiso, J. Back-to-Basics tutorial: X-ray diffraction of thin films. *J Electroceram* **47**, 141–163 (2021).

[127] Bracco, G. & Holst, B. *Surface Science Techniques*. Springer (2013).

[128] Friedbacher, G. & Bubert, H., editors *Surface and Thin Film Analysis: A Compendium of Principles, Instrumentation, and Applications*. Wiley (2011).

[129] Goldstein, J., Newbury, D. E., Michael, J. R., Ritchie, N. W. M., Scott, J. H. J. & Joy, D. C. *Scanning Electron Microscopy and X-ray Microanalysis*. Springer, 4th edition (2018).

[130] Peters, KR. Conditions required for high quality high magnification images in secondary electron-I scanning electron microscopy. *Scan Electron Microsc* **Pt 4**, 1359–1372 (1982).

[131] Peters, KR. Working at Higher Magnifications in Scanning Electron Microscopy with Secondary and Backscattered Electrons on Metal Coated Biological Specimens and Imaging Macromolecular Cell Membrane Structures. *Scanning Electron Microscopy* **4**, 257–282 (1985).

[132] Williams, D. B. & Carter, C. B. *Transmission Electron Microscopy*. Springer (2009).

[133] Fultz, B. & Howe, J. M. *Transmission Electron Microscopy and Diffractometry of Materials*. Springer, 3rd edition (2008).

[134] Mattox, D. M. *Handbook of Physical Vapor Deposition (PVD) Processing*. William Andrew, 2nd edition (2010).

[135] Venables, J., editor *Introduction to Surface and Thin Film Processes*. Cambridge University Press (2000).

[136] Chrisey, D. B. & Hubler, G. K. *Pulsed Laser Deposition of Thin Films*. J. Wiley (1994).

[137] Oura, K., editor *Surface Science: An Introduction*. Advanced Texts in Physics. Springer (2003).

[138] Schou, J. Physical aspects of the pulsed laser deposition technique: The stoichiometric transfer of material from target to film. *Applied Surface Science* **255**, 5191–5198 (2009).

[139] Sarangan, A. 5 - Nanofabrication. In Haus, J. W., editor, *Fundamentals and Applications of Nanophotonics*, pp. 149–184. Woodhead Publishing (2016).

[140] Kotsonis, G. N., Rost, C. M., Harris, D. T. & Maria, J.-P. Epitaxial entropy-stabilized oxides: Growth of chemically diverse phases via kinetic bombardment. *MRS Communications* **8**, 1371–1377 (2018).

[141] Kääriäinen, T., Cameron, D., Kääriäinen, M.-L. & Sherman, A. *Atomic Layer Deposition: Principles, Characteristics, and Nanotechnology Applications*. Scrivener Publishing, 2nd edition (2013).

[142] Profijt, H. B., Potts, S. E., Van De Sanden, M. C. M. & Kessels, W. M. M. Plasma-Assisted Atomic Layer Deposition: Basics, Opportunities, and Challenges. *Journal of Vacuum Science & Technology A: Vacuum, Surfaces, and Films* **29**, 050801 (2011).

[143] Johnson, R. W., Hultqvist, A. & Bent, S. F. A brief review of atomic layer deposition: From fundamentals to applications. *Materials Today* **17**, 236–246 (2014).

[144] Leskelä, M. & Ritala, M. Atomic Layer Deposition Chemistry: Recent Developments and Future Challenges. *Angew Chem Int Ed* **42**, 5548–5554 (2003).

[145] George, S. M. Atomic Layer Deposition: An Overview. *Chem. Rev.* **110**, 111–131 (2010).

[146] Oke, J. A. & Jen, T.-C. Atomic layer deposition and other thin film deposition techniques: From principles to film properties. *Journal of Materials Research and Technology* **21**, 2481–2514 (2022).

[147] Panjan, P., Drnovšek, A., Gselman, P., Čekada, M. & Panjan, M. Review of Growth Defects in Thin Films Prepared by PVD Techniques. *Coatings* **10**, 447 (2020).

[148] Zhang, L., Jiang, H. C., Liu, C., Dong, J. W. & Chow, P. Annealing of Al_2O_3 thin films prepared by atomic layer deposition. *J. Phys. D: Appl. Phys.* **40**, 3707–3713 (2007).

[149] Kim, H. Characteristics and applications of plasma enhanced-atomic layer deposition. *Thin Solid Films* **519**, 6639–6644 (2011).

[150] Webb, M. *et al.* High temperature stability of entropy-stabilized oxide $(MgCoNiCuZn)_{0.2}O$ in air. *Applied Physics Letters* **124**, 151904 (2024).

[151] Tsai, M.-H. & Yeh, J.-W. High-Entropy Alloys: A Critical Review. *Materials Research Letters* **2**, 107–123 (2014).

[152] Cantor, B. Multicomponent and High Entropy Alloys. *Entropy* **16** (2014).

[153] Toher, C., Oses, C., Hicks, D. & Curtarolo, S. Unavoidable disorder and entropy in multicomponent systems. *npj Computational Materials* **5**, 69 (2019).

[154] Chen, J. *et al.* A review on fundamental of high entropy alloys with promising high–temperature properties. *Journal of Alloys and Compounds* **760**, 15–30 (2018).

[155] MacDonald, B. E. *et al.* Recent Progress in High Entropy Alloy Research. *JOM* **69**, 2024–2031 (2017).

[156] Fazakas, É. *et al.* Experimental and theoretical study of $Ti_{20}Zr_{20}Hf_{20}Nb_{20}X_{20}$ (X=V or Cr) refractory high-entropy alloys. *International Journal of Refractory Metals and Hard Materials* **47**, 131–138 (2014).

[157] Poulia, A., Georgatis, E., Lekatou, A. & Karantzalis, A. Microstructure and wear behavior of a refractory high entropy alloy. *International Journal of Refractory Metals and Hard Materials* **57**, 50–63 (2016).

[158] De Fontaine, D. *Principles of Classical Thermodynamics: Applied to Materials Science*. World Scientific Publishing (2019).

[159] Holcomb, G. R., Tylczak, J. & Carney, C. Oxidation of CoCrFeMnNi High Entropy Alloys. *JOM* **67**, 2326–2339 (2015).

[160] Rost, C. M. *et al.* Entropy-stabilized oxides. *Nature Communications* **6**, 8485 (2015).

[161] Ward, T. Z. *et al.* High entropy ceramics for applications in extreme environments. *J. Phys. Mater.* **7**, 021001 (2024).

[162] Oses, C., Toher, C. & Curtarolo, S. High-entropy ceramics. *Nature Reviews Materials* **5**, 295–309 (2020).

[163] Rost, C. M., Rak, Z., Brenner, D. W. & Maria, J.-P. Local structure of the $Mg_xNi_xCo_xCu_xZn_xO$(x=0.2) entropy-stabilized oxide: An EXAFS study. *Journal of the American Ceramic Society* **100**, 2732–2738 (2017).

[164] Wang, Y., Mi, J. & Wu, Z.-S. Recent status and challenging perspective of high entropy oxides for chemical catalysis. *Chem Catalysis* **2**, 1624–1656 (2022).

[165] Musicó, B. L. *et al.* The emergent field of high entropy oxides: Design, prospects, challenges, and opportunities for tailoring material properties. *APL Materials* **8**, 040912 (2020).

[166] Kotsonis, G. N. *et al.* High-entropy oxides: Harnessing crystalline disorder for emergent functionality. *Journal of the American Ceramic Society* **106**, 5587–5611 (2023).

[167] Chen, H. *et al.* Entropy-stabilized metal oxide solid solutions as CO oxidation catalysts with high-temperature stability. *J. Mater. Chem. A* **6**, 11129–11133 (2018).

[168] Meisenheimer, P. B. *et al.* Magnetic frustration control through tunable stereochemically driven disorder in entropy-stabilized oxides. *Phys. Rev. Materials* **3**, 104420 (2019).

[169] Meisenheimer, P. B., Kratofil, T. J. & Heron, J. T. Giant Enhancement of Exchange Coupling in Entropy-Stabilized Oxide Heterostructures. *Scientific Reports* **7**, 13344 (2017).

[170] Yoo, S. *et al.* Efficient data processing using tunable entropy-stabilized oxide memristors. *Nature Electronics* **7**, 466–474 (2024).

[171] Kotsonis, G. N. *et al.* Property and cation valence engineering in entropy-stabilized oxide thin films. *Phys. Rev. Materials* **4**, 100401 (2020).

[172] Almishal, S. S. *et al.* Untangling individual cation roles in rock salt high-entropy oxides. *Acta Materialia* **279**, 120289 (2024).

[173] Sarkar, A. *et al.* High entropy oxides for reversible energy storage. *Nature Communications* **9**, 3400 (2018).

[174] Lim, M. *et al.* Influence of mass and charge disorder on the phonon thermal conductivity of entropy stabilized oxides determined by molecular dynamics simulations. *Journal of Applied Physics* **125**, 055105 (2019).

[175] Bérardan, D., Franger, S., Dragoe, D., Meena, A. K. & Dragoe, N. Colossal dielectric constant in high entropy oxides. *Phys. Status Solidi (RRL)* **10**, 328–333 (2016).

[176] Bérardan, D., Franger, S., Meena, A. K. & Dragoe, N. Room temperature lithium superionic conductivity in high entropy oxides. *J. Mater. Chem. A* **4**, 9536–9541 (2016).

[177] Braun, J. L. *et al.* Charge-Induced Disorder Controls the Thermal Conductivity of Entropy-Stabilized Oxides. *Advanced Materials* **30**, 1805004 (2018).

[178] Niculescu, G. E. *et al.* Local structure maturation in high entropy oxide $(Mg,Co,Ni,Cu,Zn)_{1-x}(Cr,Mn)_xO$ thin films. *J Am Ceram Soc.* p. e20171 (2024).

[179] Berardan, D., Meena, A., Franger, S., Herrero, C. & Dragoe, N. Controlled Jahn-Teller distortion in (MgCoNiCuZn)O-based high entropy oxides. *Journal of Alloys and Compounds* **704**, 693–700 (2017).

[180] Fracchia, M., Coduri, M., Manzoli, M., Ghigna, P. & Tamburini, U. A. Is configurational entropy the main stabilizing term in rock-salt $Mg_{0.2}Co_{0.2}Ni_{0.2}Cu_{0.2}Zn_{0.2}O$ high entropy oxide? *Nature Communications* **13**, 2977 (2022).

[181] Coduri, M., Magnaghi, L. R., Fracchia, M., Biesuz, R. & Anselmi-Tamburini, U. Assessing Phase Stability in High-Entropy Materials by Design of Experiments: The Case of the (Mg,Ni,Co,Cu,Zn)O System. *Chem. Mater.* **36**, 720–729 (2024).

[182] Anthrop, D. F. & Searcy, A. W. Sublimation and Thermodynamic Properties of Zinc Oxide. *J. Phys. Chem.* **68**, 2335–2342 (1964).

[183] Xia, L., Liu, Z. & Taskinen, P. Solubility study of the halite and wurtzite solid solutions in the MgO-ZnO system within temperature range from 1000 to 1600 °C. *Journal of Alloys and Compounds* **687**, 827–832 (2016).

[184] Eric, H. & Timuçin, M. Equilibrium relations in the system nickel oxide-copper oxide. *Metallurgical Transactions B* **10**, 561–563 (1979).

[185] Zabdyr, L. A. & Fabrichnaya, O. B. Phase equilibria in the cobalt oxide-copper oxide system. *Journal of Phase Equilibria* **23**, 149 (2002).

[186] Gadalla, AMM. & White, J. Equilibrium relationships in the system CuO–Cu_2O–MgO. *Trans. and J. Br. Ceram. Soc* **63**, 119–34 (1964).

[187] Ma, C. & Navrotsky, A. Thermodynamics of the CoO–ZnO System at Bulk and Nanoscale. *Chem. Mater.* **24**, 2311–2315 (2012).

[188] Juan, A. B., Clausell-Terol, C., Fonfría, J. C. J. & Fuster, M. M. The influence of green microstructure and sintering parameters on precipitation process during copper-nickel-zinc ferrites sintering. *Boletin De La Sociedad Espanola De Ceramica Y Vidrio* **53**, 69–75 (2014).

[189] The International Centre for Diffraction Data - ICDD. https://www.icdd.com/ (2024).

[190] Rost, C. M. *et al.* On the thermal and mechanical properties of $Mg_{0.2}Co_{0.2}Ni_{0.2}Cu_{0.2}Zn_{0.2}O$ across the high-entropy to entropy-stabilized transition. *APL Materials* **10**, 121108 (2022).

[191] Yan, J. *et al.* Pressure-induced suppression of Jahn–Teller distortions and enhanced electronic properties in high-entropy oxide $(Mg_{0.2}Ni_{0.2}Co_{0.2}Zn_{0.2}Cu_{0.2})O$. *Applied Physics Letters* **119**, 151901 (2021).

[192] Tarantino, S. C., Giannini, M., Carpenter, M. A. & Zema, M. Cooperative Jahn–Teller effect and the role of strain in the tetragonal-to-cubic phase transition in $Mg_xCu_{1-x}Cr_2O_4$. *IUCrJ* **3**, 354–366 (2016).

[193] Weast, R. C., editor *CRC Handbook of Chemistry and Physics: A Ready-Reference Book of Chemical and Physical Data*. CRC Press, 68. ed., 1987-1988 edition (1987).

[194] Lide, D. R., editor *CRC Handbook of Chemistry and Physics: A Ready-Reference Book of Chemical and Physical Data*. CRC Press, 79. ed., 1998 - 1999 edition (1998).

[195] Budavari, S. *The Merck Index : An Encyclopedia of Chemicals, Drugs, and Biologicals*. Merck, 12th edition (1996).

[196] Smallman, R. & Ngan, A. Chapter 10 - Surfaces, Grain Boundaries and Interfaces. In *Modern Physical Metallurgy*, pp. 415–442. Butterworth-Heinemann, 8th edition (2014).

[197] Chae, S., Williams, L., Lee, J., Heron, J. T. & Kioupakis, E. Effects of local compositional and structural disorder on vacancy formation in entropy-stabilized oxides from first-principles. *npj Computational Materials* **8**, 95 (2022).

[198] Kaufman, J. & Esfarjani, K. Tunable lattice distortion in $MgCoNiCuZnO_5$ entropy-stabilized oxide. *Journal of Materials Research* **36**, 1615–1623 (2021).

[199] Vegard, L. Die Konstitution der Mischkristalle und die Raumfüllung der Atome. *Zeitschrift für Physik* **5**, 17–26 (1921).

[200] Shannon, R. D. Revised effective ionic radii and systematic studies of interatomic distances in halides and chalcogenides. *Acta Crystallographica Section A* **32**, 751–767 (1976).

[201] Hamdi, H., Abedi, H. R. & Zhang, Y. A review study on thermal stability of high entropy alloys: Normal/abnormal resistance of grain growth. *Journal of Alloys and Compounds* **960**, 170826 (2023).

[202] Evans, D., Chen, J., Bokas, G., Chen, W., Hautier, G. & Sun, W. Visualizing temperature-dependent phase stability in high entropy alloys. *npj Computational Materials* **7**, 151 (2021).

[203] Webb, M. *et al.* Geometric defects induced by strain relaxation in thin film oxide superlattices. *Journal of Applied Physics* **132**, 185307 (2022).

[204] Zhou, Z. *et al.* High-temperature, spectrally-selective, scalable, and flexible thin-film Si absorber and emitter. *Opt. Mater. Express* **10**, 208 (2020).

[205] Song, J. *et al.* Design of All-Oxide Multilayers with High-Temperature Stability Toward Future Thermophotovoltaic Applications. *Adv Materials Inter* **11**, 2300733 (2024).

[206] Xu, L. *et al.* High-temperature thin-film strain sensors with low temperature coefficient of resistance and high sensitivity via direct ink writing. *Nanotechnology and Precision Engineering* **8**, 013001 (2025).

[207] Kreider, K. G. & Gillen, G. High temperature materials for thin-film thermocouples on silicon wafers. *Thin Solid Films* **376**, 32–37 (2000).

[208] LaPotin, A. *et al.* Thermophotovoltaic efficiency of 40%. *Nature* **604**, 287–291 (2022).

[209] Fraas, L. M., Avery, J. E. & Huang, H. X. Thermophotovoltaic furnace-generator for the home using low bandgap GaSb cells. *Semiconductor Science Technology* **18**, S247–S253 (2003).

[210] Ferguson, L. G. & Dogan, F. A highly efficient NiO-Doped MgO matched emitter for thermophotovoltaic energy conversion. *Materials Science and Engineering: B* **83**, 35–41 (2001).

[211] Wojtczak, L. The Melting Point of Thin Films. *Phys. Status Solidi (b)* **23** (1967).

[212] Thompson, C. V. Solid-State Dewetting of Thin Films. *Annu. Rev. Mater. Res.* **42**, 399–434 (2012).

[213] Chirumamilla, M. *et al.* Thermal stability of tungsten based metamaterial emitter under medium vacuum and inert gas conditions. *Scientific Reports* **10**, 3605 (2020).

[214] Wang, Y. *et al.* Hybrid Solar Absorber–Emitter by Coherence-Enhanced Absorption for Improved Solar Thermophotovoltaic Conversion. *Advanced Optical Materials* **6**, 1800813 (2018).

[215] Kim, J. H., Jung, S. M. & Shin, M. W. Thermal degradation of refractory layered metamaterial for thermophotovoltaic emitter under high vacuum condition. *Opt. Express* **27**, 3039–3054 (2019).

[216] Shimizu, M., Kohiyama, A. & Yugami, H. Evaluation of thermal stability in spectrally selective few-layer metallo-dielectric structures for solar thermophotovoltaics. *Journal of Quantitative Spectroscopy and Radiative Transfer* **212**, 45–49 (2018).

[217] Cui, K., Lemaire, P., Zhao, H., Savas, T., Parsons, G. & Hart, A. J. Tungsten–Carbon Nanotube Composite Photonic Crystals as Thermally Stable Spectral-Selective Absorbers and Emitters for Thermophotovoltaics. *Advanced Energy Materials* **8**, 1801471 (2018).

[218] Cho, J.-W. *et al.* Optical Tunneling Mediated Sub-Skin-Depth High Emissivity Tungsten Radiators. *Nano Lett.* **19**, 7093–7099 (2019).

[219] Chan, W. R., Stelmakh, V., Ghebrebrhan, M., Soljačić, M., Joannopoulos, J. D. & Čelanović, I. Enabling efficient heat-to-electricity generation at the mesoscale. *Energy Environ. Sci.* **10**, 1367–1371 (2017).

[220] Li, P. *et al.* Large-Scale Nanophotonic Solar Selective Absorbers for High-Efficiency Solar Thermal Energy Conversion. *Advanced Materials* **27**, 4585–4591 (2015).

[221] Arpin, K. A., Losego, M. D. & Braun, P. V. Electrodeposited 3D Tungsten Photonic Crystals with Enhanced Thermal Stability. *Chem. Mater.* **23**, 4783–4788 (2011).

[222] Kim, Y., Kim, M.-J., Kim, Y.-S., Lee, H. & Lee, S.-M. Nanostructured Radiation Emitters: Design Rules for High-Performance Thermophotovoltaic Systems. *ACS Photonics* **6**, 2260–2267 (2019).

[223] Chou, J. B. *et al.* Enabling Ideal Selective Solar Absorption with 2D Metallic Dielectric Photonic Crystals. *Advanced Materials* **26**, 8041–8045 (2014).

[224] Peykov, D., Yeng, Y. X., Celanovic, I., Joannopoulos, J. D. & Schuh, C. A. Effects of surface diffusion on high temperature selective emitters. *Opt. Express* **23**, 9979–9993 (2015).

[225] Dyachenko, P. N. *et al.* Controlling thermal emission with refractory epsilon-near-zero metamaterials via topological transitions. *Nature Communications* **7**, 11809 (2016).

[226] Lee, H.-J. *et al.* Hafnia-plugged microcavities for thermal stability of selective emitters. *Applied Physics Letters* **102**, 241904 (2013).

[227] Han, S., Shin, J.-H., Jung, P.-H., Lee, H. & Lee, B. J. Broadband Solar Thermal Absorber Based on Optical Metamaterials for High-Temperature Applications. *Advanced Optical Materials* **4**, 1265–1273 (2016).

[228] Wells, M. P. *et al.* Temperature stability of thin film refractory plasmonic materials. *Opt. Express* **26**, 15726–15744 (2018).

[229] Berquist, Z. J., Gayle, A. J., Dasgupta, N. P. & Lenert, A. Transparent Refractory Aerogels for Efficient Spectral Control in High-Temperature Solar Power Generation. *Advanced Functional Materials* **32**, 2108774 (2022).

[230] Zhang, R.-Z. & Reece, M. J. Review of high entropy ceramics: Design, synthesis, structure and properties. *J. Mater. Chem. A* **7**, 22148–22162 (2019).

[231] Ronchi, C. & Sheindlin, M. Melting point of MgO. *Journal of Applied Physics* **90**, 3325–3331 (2001).

[232] Lee, H. J. *Thermal Stability of Nano-Structured Selective Emitters for Thermophotovoltaic Systems*. PhD thesis, Massachusetts Institute of Technology (2012).

[233] Wang, Z. *et al.* Selective emitter materials and designs for high-temperature thermophotovoltaic applications. *Solar Energy Materials and Solar Cells* **238**, 111554 (2022).

[234] Wang, J. *et al.* High-Selectivity Planar Thermal Emitter with a Stable Temperature over 1400 K for a Thermophotovoltaic System. *ACS Appl. Mater. Interfaces* **15**, 49123–49131 (2023).

[235] Stephens, R. & Malitson, I. Index of refraction of magnesium oxide. *J. Res. Natl. Bur. Stan.* **49**, 249 (1952).

[236] Mahmoud, S. A., Shereen, A. & Tarawnh, M. A. Structural and Optical Dispersion Characterisation of Sprayed Nickel Oxide Thin Films. *JMP* **02**, 1178–1186 (2011).

[237] Prostakova, V., Chen, J., Jak, E. & Decterov, S. A. Experimental study and thermodynamic optimization of the CaO–NiO, MgO–NiO and NiO–SiO_2 systems. *Calphad* **37**, 1–10 (2012).

[238] Perrichon, A. *et al.* Unraveling the Ground-State Structure of $BaZrO_3$ by Neutron Scattering Experiments and First-Principles Calculations. *Chem. Mater.* **32**, 2824–2835 (2020).

[239] Knight, K. S. Low-temperature thermophysical and crystallographic properties of $BaZrO_3$ perovskite. *J Mater Sci* **55**, 6417–6428 (2020).

[240] Xin, C. *et al.* Single crystal growth of $BaZrO_3$ from the melt at 2700 °C using optical floating zone technique and growth prospects from BaB_2O_4 flux at 1350 °C. *CrystEngComm* **21**, 502–512 (2019).

[241] Cimino, A., Porta, P. & Valigi, M. Dependence of the Lattice Parameter of Magnesium Oxide on Crystallite Size. *J American Ceramic Society* **49**, 152–156 (1966).

[242] Haynes, W. M., editor *CRC Handbook of Chemistry and Physics*. CRC Press, 0 edition (2014).

[243] Maekawa, T., Kurosaki, K. & Yamanaka, S. Thermal and Mechanical Properties of Perovskite-Type Barium Hafnate. *ChemInform* **37** (2006).

[244] Jain, A. *et al.* Commentary: The Materials Project: A materials genome approach to accelerating materials innovation. *APL Materials* **1**, 011002 (2013).

[245] Fan, D., Burger, T., McSherry, S., Lee, B., Lenert, A. & Forrest, S. R. Near-perfect photon utilization in an air-bridge thermophotovoltaic cell. *Nature* **586**, 237–241 (2020).

[246] Sugawara, M., Kondo, M., Yamazaki, S. & Nakajima, K. Exact determination of superlattice structure by small-angle x-ray diffraction. *Journal of Crystal Growth* **93**, 318–322 (1988).

[247] Fewster, P. F. Superlattices. In *X-Ray and Neutron Dynamical Diffraction: Theory and Applications*, pp. 289–299. Springer (1996).

[248] Sasamoto, T., Mizushima, K. & Sata, T. Transpiration Study of the Reaction of Water Vapor with Barium Oxide. *Bulletin of the Chemical Society of Japan* **52**, 2127–2129 (1979).

[249] Meschter, P. J., Opila, E. J. & Jacobson, N. S. Water Vapor–Mediated Volatilization of High-Temperature Materials. *Annu. Rev. Mater. Res.* **43**, 559–588 (2013).

[250] Wang, X., Lee, E., Xu, C. & Liu, J. High-efficiency, air-stable manganese–iron oxide nanoparticle-pigmented solar selective absorber coatings toward concentrating solar power systems operating at 750 °C. *Materials Today Energy* **19**, 100609 (2021).

[251] Zou, C., Xie, W. & Shao, L. Functional multi-layer solar spectral selective absorbing coatings of AlCrSiN/AlCrSiON/AlCrO for high temperature applications. *Solar Energy Materials and Solar Cells* **153**, 9–17 (2016).

[252] Li, W. *et al.* Refractory Plasmonics with Titanium Nitride: Broadband Metamaterial Absorber. *Advanced Materials* **26**, 7959–7965 (2014).

[253] Chirumamilla, M. *et al.* Large-Area Ultrabroadband Absorber for Solar Thermophotovoltaics Based on 3D Titanium Nitride Nanopillars. *Advanced Optical Materials* **5**, 1700552 (2017).

[254] Kaiser, N. Review of the fundamentals of thin-film growth. *Appl. Opt.* **41**, 3053–3060 (2002).

[255] Frank, F. C. & van der Merwe, J. H. One-dimensional dislocations. II. Misfitting monolayers and oriented overgrowth. *Proc. R. Soc. Lond. A* **198**, 216–225 (1949).

[256] Van Der Merwe, J. H. Crystal Interfaces. Part I. Semi-Infinite Crystals. *Journal of Applied Physics* **34**, 117–122 (1963).

[257] Matthews, J. & Blakeslee, A. Defects in epitaxial multilayers. *Journal of Crystal Growth* **27**, 118–125 (1974).

[258] Matthews, J., Jackson, D. & Chambers, A. Effect of coherency strain and misfit dislocations on the mode of growth of thin films. *Thin Solid Films* **26**, 129–134 (1975).

[259] Dai, Y., Schubert, J., Hollmann, E., Mussler, G. & Wördenweber, R. Engineering of the Curie temperature of epitaxial $Sr_{1-x}Ba_xTiO_3$ films via strain. *Journal of Applied Physics* **120**, 114101 (2016).

[260] Hirsch, P. B. Nucleation and Propagation of Misfit Dislocations in Strained Epitaxial Layer Systems. In *Polycrystalline Semiconductors II*, pp. 470–482. Springer (1991).

[261] Goretta, K. *et al.* Thermomechanical response of polycrystalline $BaZrO_3$. *Physica C: Superconductivity* **309**, 245–250 (1998).

[262] Rao, A. S. M. & Narender, K. Studies on Thermophysical Properties of CaO and MgO by γ -Ray Attenuation. *Journal of Thermodynamics* **2014**, 1–8 (2014).

[263] Miyajima, N. & Walte, N. Burgers vector determination in deformed perovskite and post-perovskite of $CaIrO_3$ using thickness fringes in weak-beam dark-field images. *Ultramicroscopy* **109**, 683–692 (2009).

[264] Doukhan, N. & Doukhan, J. C. Dislocations in perovskites $BaTiO_3$ and $CaTiO_3$. *Phys Chem Minerals* **13**, 403–410 (1986).

[265] Baskaran, A. & Smereka, P. Mechanisms of Stranski-Krastanov growth. *Journal of Applied Physics* **111**, 044321 (2012).

[266] Gault, B. *et al.* Atom probe tomography. *Nat Rev Methods Primers* **1**, 51 (2021).

[267] Baek, D. J., Lu, D., Hikita, Y., Hwang, H. Y. & Kourkoutis, L. F. Mapping cation diffusion through lattice defects in epitaxial oxide thin films on the water-soluble buffer layer $Sr_3Al_2O_6$ using atomic resolution electron microscopy. *APL Materials* **5**, 096108 (2017).

[268] Böscke, T., Müller, J., Bräuhaus, D., Schröder, U. & Böttger, U. Ferroelectricity in hafnium oxide thin films. *Applied Physics Letters* **99** (2011).

[269] Boscke, T. S., Muller, J., Brauhaus, D., Schroder, U. & Bottger, U. Ferroelectricity in hafnium oxide: CMOS compatible ferroelectric field effect transistors. In *2011 International Electron Devices Meeting*, pp. 24.5.1–24.5.4 (2011).

[270] Müller, J. *et al.* Ferroelectricity in Simple Binary ZrO_2 and HfO_2. *Nano Lett.* **12**, 4318–4323 (2012).

[271] Kim, T. Y., Kim, S. K. & Kim, S.-W. Application of ferroelectric materials for improving output power of energy harvesters. *Nano Convergence* **5**, 30 (2018).

[272] Valasek, J. Piezo-Electric and Allied Phenomena in Rochelle Salt. *Phys. Rev.* **17**, 475–481 (1921).

[273] Ball, P. Technology takes tiny steps. *Nature Mater* **6**, 182–182 (2007).

[274] Scott, J. F. New developments on FRAMs: [3D] structures and all-perovskite FETs. *Materials Science and Engineering: B* **120**, 6–12 (2005).

[275] Pradhan, D. K. *et al.* A scalable ferroelectric non-volatile memory operating at 600 °C. *Nature Electronics* **7**, 348–355 (2024).

[276] Feng, G. *et al.* A ferroelectric fin diode for robust non-volatile memory. *Nature Communications* **15**, 513 (2024).

[277] Mikolajick, T. *et al.* Next generation ferroelectric materials for semiconductor process integration and their applications. *Journal of Applied Physics* **129**, 100901 (2021).

[278] Kim, I.-J., Choi, J. & Lee, J.-S. Exploring Disturb Characteristics in 2D and 3D Ferroelectric NAND Memory Arrays for Next-Generation Memory Technology. *ACS Appl. Mater. Interfaces* **16**, 33763–33770 (2024).

[279] Ramaswamy, N. *et al.* NVDRAM: A 32Gb Dual Layer 3D Stacked Non-volatile Ferroelectric Memory with Near-DRAM Performance for Demanding AI Workloads. In *2023 International Electron Devices Meeting (IEDM)*, pp. 1–4 (2023).

[280] Shin, Y. J., Jiang, J., Jia, Y., Walker, F. J. & Ahn, C. H. Low temperature growth of epitaxial ferroelectric $BaTiO_3$. *APL Materials* **9**, 041104 (2021).

[281] Li, P. & Lu, T.-M. Direct observation of $BaTiO_3$ microcrystallites in thin amorphous $BaTiO_3$ films. *Applied Physics Letters* **59**, 1064–1065 (1991).

[282] Radaelli, G., Brivio, S., Fina, I. & Bertacco, R. Correlation between growth dynamics and dielectric properties of epitaxial $BaTiO_3$ films. *Appl. Phys. Lett.* **100**, 102904 (2012).

[283] Shaw, T. M., Trolier-McKinstry, S. & McIntyre, P. C. The Properties of Ferroelectric Films at Small Dimensions. *Annu. Rev. Mater. Sci.* **30**, 263–298 (2000).

[284] Gao, P. *et al.* Possible absence of critical thickness and size effect in ultrathin perovskite ferroelectric films. *Nat Commun* **8**, 15549 (2017).

[285] *Certain Data Included Herein Are Derived from Clarivate™ (Web of Science™). © Clarivate 2024. All Rights Reserved.* (2024).

[286] Busch, G. & Scherrer, P. A new seignette-electric substance. *Ferroelectrics* **71**, 15–16 (1935).

[287] Gray, R. B. Transducer and method of making the same. *US Patent No. 2486560A* (1949).

[288] Buck, D. A. Ferroelectrics for Digital Information Storage and Switching. Technical Report, MIT Digital Computer Laboratory (1952).

[289] Sawaguchi, E. Ferroelectricity versus Antiferroelectricity in the Solid Solutions of $PbZrO_3$ and $PbTiO_3$. *J. Phys. Soc. Jpn.* **8**, 615–629 (1953).

[290] Teague, J. R., Gerson, R. & James, W. Dielectric hysteresis in single crystal $BiFeO_3$. *Solid State Communications* **8**, 1073–1074 (1970).

[291] Cross, LE. & Newnham, R. History of Ferroelectrics. *Ceramics and Civilization* **Vol. III**, 289–305 (1987).

[292] Park, M. H., Schenk, T., Hwang, C. S. & Schroeder, U. Chapter 8 - Impact of Electrodes on the Ferroelectric Properties. In Schroeder, U., Hwang, C. S. & Funakubo, H., editors, *Ferroelectricity in Doped Hafnium Oxide: Materials, Properties and Devices*, pp. 341–364. Woodhead Publishing (2019).

[293] Bohr, M., Chau, R., Ghani, T. & Mistry, K. The High-k Solution. *IEEE Spectr.* **44**, 29–35 (2007).

[294] Gundlapudi Ravikumar, P. & Khan, A. Chapter Six - Reliability of ferroelectric devices. In *Semiconductors and Semimetals*, pp. 137–164. Elsevier (2023).

[295] Joh, H. *et al.* Low-Temperature Growth of Ferroelectric $Hf_{0.5}Zr_{0.5}O_2$ Thin Films Assisted by Deep Ultraviolet Light Irradiation. *ACS Appl. Electron. Mater.* **3**, 1244–1251 (2021).

[296] Chang, T.-J. *et al.* Atomic tailoring of low-thermal-budget and nearly wake-up-free ferroelectric $Hf_{0.5}Zr_{0.5}O_2$ nanoscale thin films by atomic layer annealing. *Applied Surface Science* **591**, 153110 (2022).

[297] Onaya, T. *et al.* Ferroelectricity of $Hf_xZr_{1-x}O_2$ thin films fabricated by 300 °C low temperature process with plasma-enhanced atomic layer deposition. *Microelectronic Engineering* **215**, 111013 (2019).

[298] Yu, H. *et al.* Flexible Inorganic Ferroelectric Thin Films for Nonvolatile Memory Devices. *Advanced Functional Materials* **27**, 1700461 (2017).

[299] Cai, Z., Toprasertpong, K., Liu, Z., Takenaka, M. & Takagi, S. Understanding HZO Thickness Scaling in Si FeFETs: Low Operating Voltage, Fast Wake-Up, and Suppressed Charge Trapping. *IEEE Transactions on Electron Devices* **71**, 3633–3639 (2024).

[300] Toprasertpong, K. *et al.* Low Operating Voltage, Improved Breakdown Tolerance, and High Endurance in $Hf_{0.5}Zr_{0.5}O_2$ Ferroelectric Capacitors Achieved by Thickness Scaling Down to 4 nm for Embedded Ferroelectric Memory. *ACS Appl. Mater. Interfaces* **14**, 51137–51148 (2022).

[301] Tahara, K. *et al.* Strategy Toward HZO BEOL-FeRAM with Low-Voltage Operation ($\leq$ 1.2 V), Low Process Temperature, and High Endurance by Thickness Scaling. In *2021 Symposium on VLSI Technology*, pp. 1–2 (2021).

[302] Chen, H. *et al.* HfO_2-based ferroelectrics: From enhancing performance, material design, to applications. *Applied Physics Reviews* **9**, 011307 (2022).

[303] Kondratyuk, E. & Chouprik, A. Polarization Switching Kinetics in Thin Ferroelectric HZO Films. *Nanomaterials* **12** (2022).

[304] Howard, C. J., Kisi, E. H. & Ohtaka, O. Crystal Structures of Two Orthorhombic Zirconias. *Journal of the American Ceramic Society* **74**, 2321–2323 (1991).

[305] Materlik, R., Künneth, C. & Kersch, A. The origin of ferroelectricity in $Hf_{1-x}Zr_xO_2$: A computational investigation and a surface energy model. *Journal of Applied Physics* **117**, 134109 (2015).

[306] Khakimov, R. R., Chernikova, A. G., Koroleva, A. A. & Markeev, A. M. On the Reliability of HZO-Based Ferroelectric Capacitors: The Cases of Ru and TiN Electrodes. *Nanomaterials* **12** (2022).

[307] Yang, W. *et al.* Effect and mechanism of point charge defects on ferroelectric domain switching properties of HfO_2-based ferroelectric thin film. *Computational Materials Science* **213**, 111607 (2022).

[308] Gong, T. *et al.* Observation and Characterization of Recoverable Fatigue Process Under Low-Electric Field (<1.8MV/cm) in HfZrO Ferroelectric Film. *IEEE Electron Device Letters* **42**, 1288–1290 (2021).

[309] Cheng, X. *et al.* Leakage mechanism in ferroelectric $Hf_{0.5}Zr_{0.5}O_2$ epitaxial thin films. *Applied Materials Today* **32**, 101804 (2023).

[310] Fields, S. S. *et al.* Wake-up and fatigue mechanisms in ferroelectric $Hf_{0.5}Zr_{0.5}O_2$ films with symmetric RuO_2 electrodes. *Journal of Applied Physics* **130**, 134101 (2021).

[311] Lenox, M. K., Jaszewski, S. T., Fields, S. S., Shukla, N. & Ihlefeld, J. F. Impact of Electric Field Pulse Duration on Ferroelectric Hafnium Zirconium Oxide Thin Film Capacitor Endurance. *Phys. Status Solidi (a)* **221**, 2300566 (2024).

[312] Mittmann, T., Fengler, F. P., Richter, C., Park, M. H., Mikolajick, T. & Schroeder, U. Optimizing process conditions for improved $Hf_{1-x}Zr_xO_2$ ferroelectric capacitor performance. *Microelectronic Engineering* **178**, 48–51 (2017).

[313] Zhang, Z. *et al.* Phase Transformation Driven by Oxygen Vacancy Redistribution as the Mechanism of Ferroelectric $Hf_{0.5}Zr_{0.5}O_2$ Fatigue. *Advanced Electronic Materials* p. 2300877 (2024).

[314] Fields, S. S. *et al.* Phase-Exchange-Driven Wake-Up and Fatigue in Ferroelectric Hafnium Zirconium Oxide Films. *ACS Appl. Mater. Interfaces* **12**, 26577–26585 (2020).

[315] Fengler, F. P. G., Hoffmann, M., Slesazeck, S., Mikolajick, T. & Schroeder, U. On the relationship between field cycling and imprint in ferroelectric $Hf_{0.5}Zr_{0.5}O_2$. *Journal of Applied Physics* **123**, 204101 (2018).

[316] Pešić, M. *et al.* Physical Mechanisms behind the Field-Cycling Behavior of HfO_2-Based Ferroelectric Capacitors. *Advanced Functional Materials* **26**, 4601–4612 (2016).

[317] Zhao, S. *et al.* Experimental Extraction and Simulation of Charge Trapping During Endurance of FeFET With TiN/HfZrO/SiO_2/Si (MFIS) Gate Structure. *IEEE Transactions on Electron Devices* **69**, 1561–1567 (2022).

[318] Liao, P. J. *et al.* Characterization of Fatigue and Its Recovery Behavior in Ferroelectric HfZrO. In *2021 Symposium on VLSI Technology*, pp. 1–2 (2021).

[319] Wei, W. *et al.* Deep Insights into the Failure Mechanisms in Field-cycled Ferroelectric $Hf_{0.5}Zr_{0.5}O_2$ Thin Film: TDDB Characterizations and First-Principles Calculations. In *2020 IEEE International Electron Devices Meeting (IEDM)*, pp. 39.6.1–39.6.4 (2020).

[320] Zhang, Y. *et al.* Evolution of the conductive filament system in HfO_2-based memristors observed by direct atomic-scale imaging. *Nat Commun* **12**, 7232 (2021).

[321] De Stefano, F., Houssa, M., Afanas'ev, V. V., Kittl, J. A., Jurczak, M. & Stesmans, A. Nature of the filament formed in HfO_2-based resistive random access memory. *Thin Solid Films* **533**, 15–18 (2013).

[322] Brivio, S., Tallarida, G., Cianci, E. & Spiga, S. Formation and disruption of conductive filaments in a HfO_2/TiN structure. *Nanotechnology* **25**, 385705 (2014).

[323] Lin, K.-L., Hou, T.-H., Shieh, J., Lin, J.-H., Chou, C.-T. & Lee, Y.-J. Electrode dependence of filament formation in HfO_2 resistive-switching memory. *Journal of Applied Physics* **109**, 084104 (2011).

[324] Yan, S. *et al.* Influence of metal electrodes on the irradiation resistance of HZO ferroelectric thin film capacitors and mechanism analysis. *Journal of Alloys and Compounds* **976**, 173175 (2024).

[325] Wang, D. *et al.* Enhanced ferroelectric polarization with less wake-up effect and improved endurance of $Hf_{0.5}Zr_{0.5}O_2$ thin films by implementing W electrode. *Journal of Materials Science & Technology* **104**, 1–7 (2022).

[326] Xu, P. *et al.* Effects of different metal electrodes on the ferroelectric properties of HZO thin films. *Journal of Materials Science: Materials in Electronics* **34**, 1915 (2023).

[327] Lee, Y., Goh, Y., Hwang, J., Das, D. & Jeon, S. The Influence of Top and Bottom Metal Electrodes on Ferroelectricity of Hafnia. *IEEE Transactions on Electron Devices* **68**, 523–528 (2021).

[328] Segantini, G. *et al.* Interplay between Strain and Defects at the Interfaces of Ultra-Thin $Hf_{0.5}Zr_{0.5}O_2$-Based Ferroelectric Capacitors. *Advanced Electronic Materials* **9**, 2300171 (2023).

[329] Wei, J., Jiang, L., Huang, M., Wu, Y. & Chen, S. Intrinsic Defect Limit to the Growth of Orthorhombic HfO_2 and $(Hf,Zr)O_2$ with Strong Ferroelectricity: First-Principles Insights. *Advanced Functional Materials* **31**, 2104913 (2021).

[330] Esteves, G., Ramos, K., Fancher, C. & Jones, J. *LIPRAS: Line-Profile Analysis Software* (2017).

[331] Toby, B. H. & Von Dreele, R. B. *GSAS-II* : The genesis of a modern open-source all purpose crystallography software package. *J Appl Crystallogr* **46**, 544–549 (2013).

[332] *ASTM Standard, E112-10* (2013).

[333] Vassighi, A. & Sachdev, M., editors *Thermal and Power Management of Integrated Circuits*. Springer (2006).

[334] Nittayakasetwat, S. & Kita, K. Evidence of ferroelectric HfO_2 phase transformation induced by electric field cycling observed at a macroscopic scale. *Solid-State Electronics* **184**, 108086 (2021).

[335] Jaszewski, S. T. *et al.* Phase Transformations Driving Biaxial Stress Reduction During Wake-Up of Ferroelectric Hafnium Zirconium Oxide Thin Films. *Advanced Electronic Materials* p. 2400151 (2024).

[336] Bouaziz, J., Romeo, P. R., Baboux, N. & Vilquin, B. Huge Reduction of the Wake-Up Effect in Ferroelectric HZO Thin Films. *ACS Appl. Electron. Mater.* **1**, 1740–1745 (2019).

[337] Shvilberg, L. *et al.* Oxygen diffusion coefficients in ferroelectric hafnium zirconium oxide thin films. *Applied Physics Letters* **124**, 252905 (2024).

[338] Wu, X. *et al.* Evolution of Filament Formation in Ni/HfO_2/SiO/Si-Based RRAM Devices. *Advanced Electronic Materials* **1**, 1500130 (2015).

[339] Brodie, G., Jacob, M. V. & Farrell, P. *Microwave and Radio-Frequency Technologies in Agriculture: An Introduction for Agriculturalists and Engineers*. De Gruyter Open (2015).

[340] Abdulazhanov, S. *et al.* RF-Characterization of HZO Thin Film Varactors. *Crystals* **11**, 980 (2021).

[341] Holman, J. P. *Heat Transfer*. McGraw-Hill Series in Mechanical Engineering. McGraw-Hill Higher Education, 10th edition (2010).

[342] Yamasue, E., Susa, M., Fukuyama, H. & Nagata, K. Thermal conductivities of silicon and germanium in solid and liquid states measured by non-stationary hot wire method with silica coated probe. *Journal of Crystal Growth* **234**, 121–131 (2002).

[343] Francois, T. *et al.* Impact of area scaling on the ferroelectric properties of back-end of line compatible $Hf_{0.5}Zr_{0.5}O_2$ and Si:HfO_2-based MFM capacitors. *Applied Physics Letters* **118**, 062904 (2021).

[344] Lee, J. *et al.* Role of oxygen vacancies in ferroelectric or resistive switching hafnium oxide. *Nano Convergence* **10**, 55 (2023).

[345] Privitera, S., Bersuker, G., Lombardo, S., Bongiorno, C. & Gilmer, D. Conductive filament structure in HfO_2 resistive switching memory devices. *Solid-State Electronics* **111**, 161–165 (2015).

[346] McCormack, S. J. & Navrotsky, A. Thermodynamics of high entropy oxides. *Acta Materialia* **202**, 1–21 (2021).

[347] Brahlek, M. *et al.* What is in a name: Defining "high entropy" oxides. *APL Materials* **10**, 110902 (2022).

[348] Wypych, G. Fillers – Origin, Chemical Composition, Properties, and Morphology. In *Handbook of Fillers*, pp. 13–266. Elsevier (2016).

[349] Kılıçarslan, A., Bal, E., Dinç, M., Salmankurt, B. & Duman, S. First-principles studies of the atomic, elastic and vibrational properties of $BaNbO_3$. In *9th International Physics Conference of the Balkan Physical Union*, p. 220012 (2016).

[350] Galazka, Z. *et al.* Melt growth and properties of bulk $BaSnO_3$ single crystals. *J. Phys.: Condens. Matter* **29**, 075701 (2017).

[351] Persson, K. Materials Data on $BaZrO_3$ by Materials Project (2014).

[352] Persson, K. Materials Data on MgO by Materials Project (2014).

[353] Persson, K. Materials Data on $BaHfO_3$ by Materials Project (2016).

[354] Husain, S. *et al.* Low-temperature grapho-epitaxial La-substituted $BiFeO_3$ on metallic perovskite. *Nat Commun* **15**, 479 (2024).

[355] Song, L., Glinsek, S. & Defay, E. Toward low-temperature processing of lead zirconate titanate thin films: Advances, strategies, and applications. *Applied Physics Reviews* **8**, 041315 (2021).

[356] Yamanaka, S., Kurosaki, K., Matsuda, T. & Uno, M. Thermophysical properties of $BaUO_3$. *Journal of Nuclear Materials* **294**, 99–103 (2001).

[357] Kresse, G. & Furthmüller, J. Efficient iterative schemes for ab initio total-energy calculations using a plane-wave basis set. *Phys. Rev. B* **54**, 11169–11186 (1996).

[358] Perdew, J. P., Burke, K. & Ernzerhof, M. Generalized Gradient Approximation Made Simple. *Phys. Rev. Lett.* **77**, 3865–3868 (1996).

[359] Jain, A. *et al.* A high-throughput infrastructure for density functional theory calculations. *Computational Materials Science* **50**, 2295–2310 (2011).

[360] Jain, A. *et al.* Formation enthalpies by mixing GGA and GGA + U calculations. *Phys. Rev. B* **84**, 045115 (2011).

[361] Blöchl, P. E. Projector augmented-wave method. *Phys. Rev. B* **50**, 17953–17979 (1994).

[362] Kresse, G. & Joubert, D. From ultrasoft pseudopotentials to the projector augmented-wave method. *Phys. Rev. B* **59**, 1758–1775 (1999).

[363] Hart, G. L. W. & Forcade, R. W. Generating derivative structures from multilattices: Algorithm and application to hcp alloys. *Phys. Rev. B* **80**, 014120 (2009).

[364] Hart, G. L. W. & Forcade, R. W. Algorithm for generating derivative structures. *Phys. Rev. B* **77**, 224115 (2008).

[365] Ångqvist, M. *et al.* ICET – A Python Library for Constructing and Sampling Alloy Cluster Expansions. *Advanced Theory and Simulations* **2**, 1900015 (2019).

[366] Sanchez, J., Ducastelle, F. & Gratias, D. Generalized cluster description of multicomponent systems. *Physica A: Statistical Mechanics and its Applications* **128**, 334–350 (1984).

[367] van de Walle, A. Multicomponent multisublattice alloys, nonconfigurational entropy and other additions to the Alloy Theoretic Automated Toolkit. *Calphad* **33**, 266–278 (2009).

[368] Metropolis, N., Rosenbluth, A. W., Rosenbluth, M. N., Teller, A. H. & Teller, E. Equation of State Calculations by Fast Computing Machines. *The Journal of Chemical Physics* **21**, 1087–1092 (1953).

[369] Bates, C., White, W. & Roy, R. The solubility of transition metal oxides in zinc oxide and the reflectance spectra of Mn^{2+} and Fe^{2+} in tetrahedral fields. *Journal of Inorganic and Nuclear Chemistry* **28**, 397–405 (1966).

[370] Navrotsky, A. & Muan, A. Activity-composition relations in the systems CoO-ZnO and NiO-ZnO at 1050°C. *Journal of Inorganic and Nuclear Chemistry* **33**, 35–47 (1971).

[371] Stevanović, V., Lany, S., Zhang, X. & Zunger, A. Correcting density functional theory for accurate predictions of compound enthalpies of formation: Fitted elemental-phase reference energies. *Phys. Rev. B* **85**, 115104 (2012).

[372] Mei, Z.-G., Shang, S.-L., Wang, Y. & Liu, Z.-K. Density-functional study of the thermodynamic properties and the pressure–temperature phase diagram of Ti. *Phys. Rev. B* **80**, 104116 (2009).

[373] Liu, B., Seko, A. & Tanaka, I. Cluster expansion with controlled accuracy for the MgO/ZnO pseudobinary system via first-principles calculations. *Phys. Rev. B* **86**, 245202 (2012).

[374] Liu, J. Z. & Zunger, A. Thermodynamic states and phase diagrams for bulk-incoherent, bulk-coherent, and epitaxially-coherent semiconductor alloys: Application to cubic (Ga,In)N. *Phys. Rev. B* **77**, 205201 (2008).

[375] Singh, V. K. 8 - Phase equilibria and formation of clinker phases. In Singh, V. K., editor, *The Science and Technology of Cement and Other Hydraulic Binders*, pp. 253–323. Woodhead Publishing (2023).

[376] Schneider, C. A., Rasband, W. S. & Eliceiri, K. W. NIH Image to ImageJ: 25 years of image analysis. *Nature Methods* **9**, 671–675 (2012).

[377] Guler, U., Boltasseva, A. & Shalaev, V. M. Refractory Plasmonics. *Science* **344**, 263–264 (2014).

[378] Yamanaka, S. *et al.* Thermophysical properties of $BaZrO_3$ and $BaCeO_3$. *Journal of Alloys and Compounds* **359**, 109–113 (2003).

[379] Durand, M. A. The Coefficient of Thermal Expansion of Magnesium Oxide. *Physics* **7**, 297–298 (1936).

[380] Wang, X. *et al.* Calculation of Thermal Expansion Coefficient of Rare Earth Zirconate System at High Temperature by First Principles. *Materials* **15** (2022).

[381] Ding, H., Dwaraknath, S. S., Garten, L., Ndione, P., Ginley, D. & Persson, K. A. Computational Approach for Epitaxial Polymorph Stabilization through Substrate Selection. *ACS Appl. Mater. Interfaces* **8**, 13086–13093 (2016).

[382] Wang, H., Prasad Sivan, V., Mitchell, A., Rosengarten, G., Phelan, P. & Wang, L. Highly efficient selective metamaterial absorber for high-temperature solar thermal energy harvesting. *Solar Energy Materials and Solar Cells* **137**, 235–242 (2015).

[383] Mehboob, G., Liu, M.-J., Xu, T., Hussain, S., Mehboob, G. & Tahir, A. A review on failure mechanism of thermal barrier coatings and strategies to extend their lifetime. *Ceramics International* **46**, 8497–8521 (2020).

[384] Li, J. *et al.* Thermodynamic origin of nonvolatility in resistive memory. *Matter* (2024).